METAL FLOW ANALYSIS AND MICROSTRUCTURE MODELLING OF HOT UPSET Al–B_4C COMPOSITE

A Dissertation
Submitted in partial fulfillment of the requirements for
the award of Degree of

DOCTOR OF PHILOSOPHY

in

MECHANICAL ENGINEERING

by

R SEETHARAM
(Roll No.: 714017)

Supervisors:

Dr. S. Kanmani Subbu
&
Dr. M. J. Davidson

DEPARTEMENT OF MECHANICAL ENGINEERING
NATIONAL INSTITUTE OF TECHNOLOGY,
WARANGAL (TS), INDIA,
2018

DEPARTEMENT OF MECHANICAL ENGINEERING

NATIONAL INSTITUTE OF TECHNOLOGY,

WARANGAL, TS, INDIA – 506004

CERTIFICATE

This is to certify that the dissertation work entitled **— METAL FLOW ANALYSIS AND MICROSTRUCTURE MODELLING OF HOT UPSET Al–B_4C COMPOSITE**, which is being submitted by **Mr. R SEETHARAM** (Roll No. 714017), is a bonafide work submitted to the Department of Mechanical Engineering, National Institute of Technology, Warangal in partial fulfillment of the requirement for the award of the degree of **Doctor of Philosophy in Mechanical Engineering.**

To the best of our knowledge, the work incorporated in this thesis has not been submitted elsewhere for the award of any degree.

Dr. S. Kanmani Subbu
Supervisor
Department of Mechanical Engineering
National Institute of Technology
Warangal- 506004

Dr. M. J. Davidson
Supervisor
Department of Mechanical Engineering
National Institute of Technology
Warangal- 506004

Prof. P. Bangarubabu
Head, Department of Mechanical Engineering
National Institute of Technology
Warangal-506004

This thesis dedicated to my late father,

Who always supported me, whatever path I took.

APPROVAL SHEET

This Thesis entitled "**METAL FLOW ANALYSIS AND MICROSTRUCTURE MODELLING OF HOT UPSET Al–B_4C COMPOSITE"** by **R SEETHARAM** is approved for the Degree of Doctor Philosophy

Examiners

Supervisors

Dr. S. Kanmani Subbu (Asst. Prof., MED)

&

Dr. M. J. Davidson (Assoc. Prof., MED)

Chairman

Prof. P. Bangarubabu,
MED, NIT WARANGAL

DECLARATION

This is to certify that the work presented in the thesis entitled. **"METAL FLOW ANALYSIS AND MICROSTRUCTURE MODELLING OF HOT UPSET Al–B_4C COMPOSITE"** is a bonafide work done by me under the supervision of **Dr. S. Kanmani Subbu** and **Dr. M. J. Davidson**, and was not submitted elsewhere for the award of any degree. I declare that this written submission represents my ideas in my own words and where others' ideas or words have been included, I have adequately cited and referenced the original sources. I also declare that I have adhered to all principles of academic honesty and integrity and have not misrepresented or fabricated or falsified any idea / data / fact / source in my submission. I understand that any violation of the above will be a cause for disciplinary action by the Institute and can also evoke penal action from the sources which have thus not been properly cited or from whom proper permission has not been taken when needed.

(R Seetharam)

(Roll No.: 714017)

Date:

ACKNOWLEDGMENT

Foremost, Praise to God.

Afterwards, I would like to express my sincere thanks and gratitude to my supervisors, **Dr. S. Kanmani Subbu,** Asst. Professor and **Dr. M. J. Davidson**, Assoc. Professors, Mechanical Engineering Department, National Institute of Technology, Warangal, for their continuous guidance, constructive suggestions, support, enthusiasm and motivation in my PhD research work. It has been a benediction for me to spend many opportune moments under the guidance of the perfectionist at the acme of professionalism.

I am grateful to Prof. **N.V. Ramana Rao,** Director, National Institute of Technology, Warangal and other top officials who gave me an opportunity to carry out research work. I thank Prof**. P. Bangarubabu**, Head of the Department of Mechanical Engineering for his help and continuous encouragement to complete this work.

I would like to express my sincere thanks to **Prof. N. Selvaraj, Prof. V. Suresh Babu** (Mechanical Engineering Department), and **Dr. R. Arockia Kumar** (Metallurgical and Materials Engineering Department), learned members of my Doctoral Scrutiny Committee for being helpful and generous during the entire course of this work.

I would like to express my sincere thanks to **Dr. Asit Kumar Khanra,** Metallurgy and Material Science Engineering Department, National Institute of Technology, Warangal for their cooperation and the help extended during this work

I wish to thank the Lab technicians and my fellow lab mates in the Department of Mechanical Engineering and Metallurgical and Materials Engineering for their support in my research work.

I also like to express my sincere thanks to all my friends and colleagues specially, to **Mr. P. Madhukar** and **Mr. B. Muarali Krishna**, and well-wishers whose list cannot be quoted, for extending their co-operation in the successful completion of this work.

Last but not the least; I would like to thank my family: my mother **Manga**, father Late **Laxman**, brother **Raju** and sister **Nellaveni** for their love, trust and patience during my journey from childhood. I am grateful to them for always supporting in my decisions and caring with the warmth of love. My heartfelt gratitude to my beloved wife **Santhoshi**, my sweet daughter **Rohikanand** and my son **Akhiranand** for bearing my demands throughout the research, which made the journey more remarkable and easy in completing the thesis.

R Seetharam (Roll No.: 714017)
Research Scholar

ABSTRACT

The present work pertains to investigate the deformation behaviour of powder metallurgical (P/M) processed Aluminium-Boron Carbide preforms during hot upsetting. A series of hot upsetting studies are carried out on P/M Al-B_4C preforms under various processing conditions to evaluate the plastic flow properties and densification behavior. This study is mainly focused on the formability behavior and developed a model to predict the flow stress and grain size of a porous Al–B_4C preforms at elevated temperatures.

The experimental work was performed to study the workability and the densification behavior of a porous Al–B_4C preforms in the present investigation. Hot upsetting tests have been carried out on Al–B_4C powder metallurgy preforms having an initial relative density of 0.9 and having different B_4C compositions of 2wt.%, 4wt.% and 6wt.%. The samples were compressed between two flat dies in a hydraulic press of 50 ton capacity under varying deformation temperatures such as 200 ^oC, 300 ^oC, 400 ^oC and 500 ^oC under the tri–axial stress state condition. The workability and densification behavior of Al–B_4C preforms were analyzed till the initiation of cracks on the outer surface of the preform. The experimental results were analyzed for the various deformation parameters such as axial strain, relative density, formability stress index and different stress ratio parameter under the tri–axial stress state condition. Formability and densification behavior were discussed with the axial strain (ε_z) during the hot upsetting process. Highest relative density and formability are attained in the Al–2wt.%B_4C composite for 500 ^oC deformation temperatures for any given axial strains. The relationships between the various stress ratio parameters ($\sigma_\theta/\sigma_{eff,}$ σ_m/σ_{eff}) and formability stress index (β_σ) as a function of the relative density under the tri–axial stress state condition were studied.

A constitutive base analysis has been conducted to develop mathematical equations to predict the hot deformation and densification behavior of P/M Al-B_4C preforms. The main aim of this work is to estimate the effect of initial relative density (IRD), deformation temperature, and strain rate on the hot deformation behavior and development of constitutive equations for predicting the hot deformation behavior. For this purpose, upsetting tests have been performed in a hydraulic press for obtaining true stress–true strain curve data of sintered Al–4wt.%B_4C composites. The upsetting tests were carried out at different IRDes of 80%,

85% and 90% for various temperatures of 300 ^{o}C, 400 ^{o}C and 500 ^{o}C and strain rates of 0.1 s^{-1}, 0.2 s^{-1} and 0.3 s^{-1}. It clearly shows that the effect of IRD, deformation temperature, and strain rate on flow stress curves is significant. The predicted flow stress results are well satisfied with the experimental flow stress result, which verifies the accuracy of the developed constitutive model for sintered Al–4wt.%B_4C composite during the hot upsetting test. In addition, the required activation energies (Q) of sintered Al–4wt.%B_4C composites during the hot upsetting, calculated for various IRDes of 80%, 85% and 90% were 161.06, 172.28 and 181.05 KJ/mol, respectively and compared with published literatures.

It is essential to understand the microstructure evolution of sintered Al–B_4C preforms during the hot deformation for controlling the grain size. Hence, the aim of this work is to evaluate the microstructure of sintered Al–4wt.%B_4C composite for different deformation conditions such as temperature, strain rate, initial relative density and deformation degree during the hot compression test by metallurgical analysis. The compression tests were performed on a 50 ton capacity hydraulic press for different temperatures (300 ^{o}C, 400 ^{o}C and 500 ^{o}C), strain rates (0.1 s^{-1}, 0.2 s^{-1} and 0.3 s^{-1}), initial relative densities (80%, 85% and 90%) and deformation degree (reduction in preforms height of 10%, 20%, 30%, 40% and 50%). The microstructures of compressed sintered Al–4wt.%B_4C preforms were evaluated by an optical microscope (OM) for different deformation conditions. Intercept line method was used to measure the grain size of the compressed preforms. The dynamic recrystallization grain of sintered Al–4wt.%B_4C preforms are significantly sensitive to the deformation condition such as temperature, strain, strain rate and initial relative density. The average DRX grain size increases with increase in deformation temperature and IRD and with decreasing strain rate and deformation degree. The finer DRX grain size was found in hot forming process at lower deformation temperature and IRD, and at a higher strain rate and deformation degree.

In the final phase of this work, a mathematical model was developed between dynamic recrystallization grain size and Zener–Hollomon parameter, which helps in calculating the DRXed grain size for various IRDes, temperatures and strain rates. For this, experimental work was performed on sintered Al–4wt.%B_4C preforms at various initial relative densities (IRD) of 80%, 85% and 90%, and over the temperature range of 300 ^{o}C – 500 ^{o}C and strain rates range of 0.1 s^{-1} – 0.3 s^{-1}. The activation energy and Zener–Hollomon parameter of sintered Al–4wt.%B_4C preforms were calculated for different temperatures, strain rates and

IRDes. The correlation between Zener–Hollomon parameters and average DRX grain size of sintered Al–4wt.%B_4C composite were established by fitting power law for different initial relative densities. The calculated DRXed grains (d_c) are compared with measured DRXed grains (d_m) to evaluate the accuracy of the developed mathematical model of sintered Al–4wt%B_4C composite for different IRDes. It is observed that the calculated DRXed grains well agreed with the measured DRXed grains for tested deformation conditions. And the average percentage error for various IRDes and deformation conditions were not exceeding 9.92% and mean absolute error does not exceed 8.58%. This proves the precision and reliability of the developed mathematical model for sintered Al–4wt.%B_4C composite for various IRDes. The results of this work can be used to develop hot deformation regimes of Al–4wt.%B_4C preforms, providing a required DRXed grain size.

CONTENTS

List of Tables

List of Figures

List of Symbols and Abbreviations

Symbols

A_{dyn}	Material constants
A_i	Instantaneous cross section area
A_o	Initial cross section area
D_b	Bulged diameter of preform
D_{cb}	Bottom contact diameter of preform
D_c	Average surface contact diameter of preform
d_c	Calculated DRXed grains
d_{dyn}	Dynamically recrystallized grain size
D_o	Initial diameter of preform
d_m	Measured DRXed grains
D_{ct}	Top contact diameter
F	Deformation load
H_f	Final height of preform after deformation
h_i	Instantaneous height
H_o	Initial height of preform
K_i	Instantaneous strength coefficient
n	Strain hardening Exponent
n_{dyn}	Material constants
n_i	Instantaneous strain hardening Exponent
P	Normal stress
Q	Activation energy
R	Relative density
R	Universal gas constant

R^2	Correlation coefficient
T	Absolute temperature
W_a	Weight of preform in air
W_w	Weight of preform in water
Z	Zenner Hollomon parameter
α	Poisson's ratio
$\acute{\varepsilon}$	Strain rate
ε_{eff}	Effective strain
ε_r	Radial strain
ε_z	True axial strain
ε_θ	True hoop strain
σ_{eff}	Effective stress
σ_m	Mean stress or hydrostatic stress
σ_o	Yield stess
σ_z	Axial stress
σ_θ	Hoop stress
a	Material constant
A	Material constant
β	Material constant
β_σ	Formability stress index
δ	Absolute error
δ_m	Mean absolute error
ρ_f	Final density
ρ_o	Initial density
σ	Flow stress

σ_E	Experimental flow stress
σ_P	Predicted flow stress

Abbreviations

P/M	Powder metallurgy
WH	Work hardening
DRV	Dynamic recovery
DRX	Dynamic recrystallization (DRX)
SEM	Scanning electron microscope (SEM)
EDAX	Energy-Dispersive X-ray Analysis
IRD	Initial relative density
OM	Optical microscope
PFS	Peak flow stress
FEM	Finite element method
FGM	Functionally graded materials

List of Appendices

CHAPTER 1

Introduction

1.1 Foreword of the present work

Metal forming is one of the competitive manufacturing processes to make engineering parts catering to the needs of the various industries such as automotive, aerospace, transportation, marine, nuclear industries, defense, etc. industries at higher production rate with minimum cost. The major advantage of forming process compared to other manufacturing processes is that it produces parts with superior mechanical properties with minimum waste of material. In forming operation, it is essential to know the forming limit of the material to fabricate parts or components without formation of a crack. Generally, formability is considered as the extent to which the material undergoes deformation without formation of a crack. The formability mainly depends on the properties of material, types of process and its process parameters. The formability of Powder Metallurgy (P/M) components depends on aspect ratio, initial relative density, preform geometry, interface friction, particle size and percentage content of reinforcement in the material under various stress state conditions. Therefore, understanding the flow of material during plastic deformation is important for metal forming industries to extend the failure limit of the material.

Powder Metallurgy (P/M) process is more advantages compared to conventional manufacturing processes such as casting, forging, machining and joining to make engineering part to satisfy the need of the above mentioned industries at higher production with minimum cost. Generally, the powder metallurgy process is a rapid, economical and high volume production method of making parts with required properties. It manufactures parts with greater surface finish, high accuracy, high wear resistance, and strength. When the requirement for intricate and near net parts, high material utilization with less wastage and low energy requirement process, are in demand, P/M is the absolute choice over other conventional manufacturing processes [1]. Powder metallurgical processed materials are extensively used as porous materials (self lubricating bearing and filters), refractory metals (lamp filaments and heating elements), friction materials (clutch liners and brake band), cemented carbides (cutting tools, wire drawing dies and deep drawing dies), bio-materials and structural materials in automotive, aerospace and defense industries.

There is a rapid growth on P/M industries over the last decades due to continuous increase in the demand for high-performance parts. However, P/M parts have poor mechanical properties because of the presence of inherent porosity left after sintering. Thus, industries mainly go for bulk-forming processes namely, forging, extrusion, rolling and hot deformation to reduce or eliminate the porosity. Therefore, investigation on bulk forming of P/M component is one of the most exciting new fields in metal forming industries due to its uniqueness in giving superior mechanical and metallurgical properties, and process flexibility over other conventional manufacturing processes.

1.2 Upset forging of powder metallurgy preforms

Various secondary processes are available for processing of P/M parts to improve the mechanical properties by reducing or eliminating the porosity. Among those, upset forging is accepted as an economical and effective method of improving the density as well as the mechanical properties through the promotion of uniform structures [2]. It is usually carried out by upsetting cylindrical billets between two parallel flat dies. Upset forging provides benefits such as fewer die requirement, less material waste, lower tooling costs and isotropic properties over other secondary processes [3].

Upset forging involves subjecting the material to compression either in cold or hot working conditions. During the forging process, the material flows into the pores, and hence the density of material increases, which results in enhanced mechanical properties and reduction in non-uniformities of metallurgical properties. Thus, the final components obtained after the upset forging of sintered parts are superior over wrought materials with the equivalent composition. Several investigations [4–6] have been reported on the upset forging of P/M preforms, and its relative merits during working. In addition, the works of several authors [7–9] revealed that upset forging of porous materials is a feasible and economical method for the production of automotive, aircraft and machine tool components.

1.3 Constraint in upset forging of P/M preforms

There is a subsequent lateral flow of metals due to induced longitudinal strain during upset forging of sintered preforms which makes the metal prone to fracture at free outside surface. Hence, the successful transformation of P/M materials depends not only on the material properties and also on the associated forming parameters such as aspect ratio (height/diameter), strain rate, initial relative density, friction, temperature, etc. [10,11]. The effect of most prominent forming parameters such as aspect ratio, initial relative density, percent content and size of particulate on the deformation behavior of sintered preforms was investigated by Narayanasamy et al. [12].

The aspect ratio limits the deformation of the material with the possibility of buckling ($h/d > 5$) shearing ($h/d > 205$), and double barring ($h/d > 2.0$) or barreling ($h/d < 2.0$). For the latter case, $h/d < 2.0$, the workpiece undergoes barreling due to interface friction constraint which paves the material for the formation of the dead or stagnant zone. At the tool-workpiece interface and dead zone of the workpiece, plastic deformation is less which proves the existence of non-uniformity or in-homogeneity in deformation and densification behavior of the material with friction.

1.4 Development of porous compacts

For the present study, it is required to have compacts of different initial densities to get various levels of properties. The powder density and the porosity depend largely on the compacting pressure during the compacting stage. If higher compacting pressures are applied, due to the compacting load, the density of the powder mass increases. Thus, by properly controlling the mass of the powder and the compacting pressure, the density and hence the porosity of the preforms can be controlled. However, it will be difficult to control the distribution of pores in the matrix. Though few attempts have been made to mathematically correlate the porosity and the applied pressure, accurate predictions could not be made and hence only average pressure only was considered.

1.5 Densification behavior of P/M preforms

During forging of porous materials, the metal flows into pores, and hence the volume of the material decrease and the density persistently increases. Densification of P/M compacts during upset forging has been reported by Kim et al. [13] and Narayan et al. [14]. The density after the deformation determines the performance and service life of the components. Thus, secondary processes which are carried out in the present investigation is hot upsetting, aimed at minimizing the uncertainties in mechanical properties and non-uniformities in the metallurgical properties by reducing or eliminating the pores and make the P/M parts available for advanced applications.

1.6 Hot deformation and modeling

In real industrial practice, understanding the hot deformation behavior of porous materials is useful for designers of metal forming processes because the metal deformation mechanism can be significantly affected by the hot working process parameters such as temperature, strain rate, strain, and porosity. As a result, the mechanical and microstructure properties of the final desired product vary accordingly. The flow behavior of the material is described by constitutive equations which are expressed in terms of linear and nonlinear relationship between process parameters mainly stress, strain, strain rate, temperature and initial relative density of the material. Several authors [15–17] developed constitutive

equations to describe the plastic flow of metals during deformation at elevated temperature. However, constitutive equations proposed for porous materials which take into account the influence of porosity are very limited. Therefore, it is also fascinating to investigate the hot deformation behavior and developed a constitutive equation to predict the flow stress by considering the influence of porosity and other process parameters such as temperature and strain rate on deformation and densification behavior.

1.7 Modeling aspect of microstructure evolution and modeling

Sintered P/M parts have poor mechanical properties due to the presence of porosity. P/M parts usually undergo bulk forming processes such as forging, extrusion, rolling and hot deformation to reduce or eliminate the porosity [18]. As a result, the microstructures or grain size of the preforms vary persistently with the influence of deformation conditions such as strain, strain rate, temperature and initial relative density. The good mechanical properties can be obtained by controlling the evolution of microstructure or grain size of the product structure. The microstructure or grain size evolution will occur during the hot forming process, and it has great influence on strength and hardness of the final product. Understanding the final microstructure or grain size of the P/M preforms after bulk forming process is essential to know service performance of components.

Nowadays, increased numbers of manufacturers of P/M components are interested in predicting the microstructure of the components and optimizing the process parameters. The microstructures information of P/M components is considerably different from their corresponding wrought metals of the same composition due to the influence of porosity [19–21]. Therefore, information of fully dense material may not be suitable for P/M materials with same composition. Dynamic recrystallization (DRX) is one of the fundamental mechanisms for the grain size or microstructure control and reduces the material resistance force during the hot forming process [22–23]. The average DRX grain sizes of the materials are described by a mathematical equation as a function of Zener-Hollomon parameters for different deformation conditions such as strain, strain rate, temperature and initial relative density. It is essential for the designer to understand the correlation between deformation process parameters and microstructures of any engineering materials during the hot forming process, to get a good quality product. Several authors [23, 24] developed a mathematical model to

describe the average DRX grain size of the material in terms of Zener-Hollomon parameters during deformation at elevated temperature. However, microstructure evolution and mathematical models proposed for porous materials which take into account the influence of porosity is limited. Therefore, it is also interesting to investigate the microstructure evolution and mathematical models to predict the grain size by considering the influence of porosity and other deformation conditions.

1.8 Applications of aluminum and P/M Al-alloys

Nowadays, aluminum and its alloys are the leading non-ferrous materials in engineering applications. In most of the engineering applications, P/M aluminium and its alloys are preferred due to its low density, high strength to weight ratio, better wear resistance, high surface finish and dimensional control. The vast applications of P/M aluminum and its alloys are in automobile and aerospace industries to reduce the weight of the product and, thereby increase the fuel efficiency and reduce exhaust emission. Some of the common applications of aluminium alloys are listed as follows:

- Aerospace: light structures, extrudates, forgings, sheets, plates, fuel tanks, brackets, fixtures, chassis, covers, and casings for many tools & devices
- Automotive: chassis, bodies, engine blocks, radiators, hubcaps, etc.
- Marine: hulls, masts, and superstructures on pleasure boats and the bridges and superstructures of passenger ships and merchant ships
- Rail: aluminium alloys sheets and extrudates
- Buildings: commonly used in extruded, sheet-rolled or molded form for window frames and other glass supports, for siding, partitions, roofing, doors, canopies,
- Packaging: foils, beverage containers, aerosols, bottle caps, lids, etc.
- Mechanical industry and engineering: robots, heat exchange parts in electronics, seawater desalination, HVAC exchangers and the plastic industry
- Energy distribution: high tension wires, telephone cable shields, and protectors against electrical and magnetic fields.

Powder metallurgical aluminium and its alloys are mainly used for their better material characteristics or ease of making complex shapes at low production cost. They have

high Young‘s modulus, low density, better high-temperature strength and better wear resistance. Their improved material characteristics make them potentially suitable for several applications in automobile and aerospace industries as follows:

- Automobile industries: camshaft bearing caps or cam caps pulleys, rod guides, shock absorber piston, oil transmission gears, brake calipers, valves, brackets, suspension components, push rods, ABS housings, etc.
- Aerospace industries: light structures, airframe structures, engine components, wings, fuselage, skin and other structural applications
- Lightweight machine components: drive belt pulleys, hubs, caps and connection collars.

Al–B_4C is one of the high-performance metal matrix composites used in industries. Al–B_4C composite is used as nuclear fuel storage tank material for storing nuclear waste in the nuclear industry due to high neutron absorption property and used as neutron shielding material. It also finds its application in hard disc substrates and brakes due to the high wear resistance property. In addition, it is used as armor plates for high ballistics performance. Al–B_4C composite can be prepared by P/M route with required porosity for high toughness and better lubrication purposes. Thus, to find the applicability of this composite in industrial applications as stated above and other similar applications, formability studies need to be conducted on Al–B_4C for better understanding the process.

1.9 Organization of the thesis

The entire thesis is presented in eight chapters including the present part as chapter 1 which presents the introduction part of deformation and densification behavior, and microstructure evolution of P/M preforms. The relevance of P/M aluminum and Al-B_4C preforms in industrial applications has been discussed.

Chapter 2 This chapter provides a detailed survey of literature relevant to the current investigation. The gaps existing in the current knowledge of deformation and densification behavior, and microstructure evolution of P/M preforms has been identified. The objectives of this work are stated and explained.

Chapter 3 In this chapter the experimental details, which includes the selection of material, specimen preparation, hot compression test, microstructure analysis by optical microscope and characterization of the investigated material have been discussed.

Chapter 4 This chapter provides detailed discussions on hot workability and densification behavior of sintered powder metallurgy Al-B_4C preforms during upsetting. The formability and densification behavior were discussed with the axial strain (ε_z) during the hot upsetting process. The relationships between the various stress ratio parameters ($\sigma_\theta/\sigma_{eff}$, σ_m/σ_{eff}) and formability stress index (β_σ) as a function of the relative density under the tri–axial stress state condition was established.

Chapter 5 In this chapter the modeling aspects of the flow behavior of sintered Al-4%B_4C composite at high-temperature upsetting has been discussed. The constitutive model was developed in terms of IRD of sintered Al–4wt.%B_4C composite to predict flow stress. The activation energy of sintered Al–4wt.%B_4C composite was calculated for different IRDes and compared with existing literatures.

Chapter 6 This chapter gives a brief introduction to microstructure evolution of sintered Al-4wt.%B_4C preforms during the hot compression test. The effect of deformation conditions such as temperature, strain rate, initial relative density and deformation degree (reduction in preforms height) on the dynamic recrystallized grain size under steady-state conditions were examined during compression tests.

Chapter 7 This chapter gives detailed discussions on microstructure modeling of sintered Al-4wt.%B_4C composite during hot upsetting. The activation energy and Zener–Hollomon parameter of sintered Al–4wt.%B_4C preforms were calculated for different temperatures, strain rates, and IRDes. Mathematical models were developed between dynamic recrystallization grain size and Zener–Hollomon parameter, which helps in calculating the DRXed grain size for various IRDes, temperatures, and strain rates.

Chapter 8 This chapter contains the conclusion drawn from the current research work and scope for future work.

1.10 Summary

This chapter initially discusses about the foreword of the present work. Later, detailed introduction about upset forging, the constraint of upset forging, development of porous compacts, and densification behavior of P/M preforms, hot deformation and modeling aspect of microstructure evolution are given. The applications of aluminium and its alloys (fully dense/porous) and Al–B_4C composite are explained. Finally, a detailed note on the organization of the thesis of each chapter is given.

CHAPTER 2

Literature Review

2.1 Introduction

Powder metallurgy is a unique process by which finished or semi-finished products are made from pure and mixed or alloyed metallic powders. The art of making parts by pressing and heating of powdered materials is an old age prehistoric process. Carpenter et al. [25] reported that many of metallic products of the older civilization could be made by using P/M technique. As notable witnesses, the famous Delhi iron pillar, certain Egyptian implements, and articles of precious metal made of Incas [26] are believed to be made by an old-time P/M technology. The modern P/M technology has emerged in the 1920s, and then it was rapidly taken to an advanced level. Since the Second World War, the P/M technique has been established as one of the competitors and most flexible methods over the other convention manufacturing processes such as casting, machining, stamping and forging for making engineering parts in automobile, aerospace, electronics, defense and nuclear industries. Powder metallurgy is the absolute choice when the need for a rapid, high volume production and better utilization material. Also, products with higher strength, high wear resistance, and intricate and near net shape is the priority.

The key steps in P/M route include powder mixing, compaction, and sintering. Powder compaction contributes to the densification of loose powder particles due to mechanical interaction between neighboring powder particles. Uniaxial die compaction is the most typical method of densification of powder particles because it is rapid and suitable for mass production. During compaction, friction at the die-powder interface has an influence on the behavior of particle interactions and densification of powder particles. Hence, several researchers [27–29] have worked and reported on how to control die wall friction and the effects of lubrication on density distribution during compaction under various conditions. Apart from the conventional die compaction method, nowadays advanced compaction techniques such as high-speed compaction [30], rotary die pressing [31], frictionless isostatic pressing [32], and warm equal channel angular pressing [33] are available for achieving effective powder consolidation.

Powder metallurgy processed parts which are made by cold die compaction essentially require sintering process to increase strength, densification and to control the dimension of parts. An effective sintering process creates strong bonding between particles with minimum oxides and having good dimensional control [34]. Generally, sintering temperature, sintering time and sintering atmosphere are major process parameters in sintering. The mechanical properties of the parts produced depend largely on sintering process, and hence sintering process parameters should be controlled. Among all sintering process parameters, sintering temperature and time are very important [35].

2.2 Deformation behavior of P/M materials

The pores are responsible for the difference in density and the mechanical properties of porous parts than their fully dense parts. Plastic deformations of P/M processed parts are essential to minimize the uncertainties in the mechanical properties and non-uniformities in metallurgical properties through reduction or elimination of porosity and thereby the strength and dimensional control of the part increases. The plastic deformation of porous parts is considerably different from the conventional fully dense parts due to the presence of pores. During deformation of P/M preforms, metal flows into the pores and close the pores thereby increasing the density.

Mohan Raj and Selvakumar [36] conducted experimental work on Fe-C-Mn composite to study the densification and deformation behavior during hot upsetting. They revealed that higher manganese content exhibits better compaction and load bearing capacity compared to lower manganese preforms. Rajeshkannan and Utkal Mehta [37] analyzed deformation studies on sintered cylindrical Iron-Carbon-Silicon-Copper Steel compacts during cold forging. The authors added 0.4% and 1.2% of copper in the developed composites and analyzed their addition in the deformation behavior. They reported the various stresses, strains and Poisson's ratio under triaxial conditions. They also observed the variation in deformations under dry condition compared to lubrication condition. Increase of copper content and frictional conditions proportionally increased axial and hoop stress, however there was no effect on mean stress.

Several authors [38–40] performed experimental investigations on work hardening behavior of P/M preforms during cold upsetting. Narayanasamy et al. [38] conducted an experimental investigation on the strain hardening behavior of Al-3.5%Al_2O_3 P/M composite under uniaxial, plane and triaxial stress state conditions during cold upsetting. They found that the instantaneous strain hardening exponent (n_i) and instantaneous strength coefficient (k_i) values are greater for triaxial state of stress conditions irrespective of the initial relative density and aspect ratio when compared to other state of stress. The work hardening behavior of elliptical shaped billets of aluminium during cold upsetting under different stress state conditions was reported by Baskara et al. [39]. They revealed that n_i and k_i vary to a large extent depending upon the aspect ratio (height/diameter) and the ratio of minor diameter to the major diameter of elliptical billet. They concluded that for any given ratio of minor diameter to major diameter, the rate of increase in n_i and k_i values with axial strain is high for lower aspect ratio preforms due to the complexity of billet geometry. Selvakumar et al. [40] performed research work on the effect of carbon content on the workability and strain hardening behavior of P/M Fe-C- 0.5Mn, and they reported that 0.1%C composition as an optimum condition which provides more strength, high initial relative density, and workability. In general, the above mentioned research works conclude that the deformation behavior of P/M performs depends largely on the processing variables such as initial relative density, aspect ratio (height/diameters), preform geometry, interface friction and content, particle size, and nature of reinforcement in the composite material.

2.3 Densification behavior of P/M materials

The presence of the inherent porosity after sintering in the P/M processed parts degrades the mechanical properties of the parts. Therefore, these parts are commonly subjected to secondary processes such as forging, rolling, extrusion and hot deformation to improve the density. Generally pores acts as sites for initiations cracks and leads to failure of the materials during the service. The final density of part determines the performance of service and life of parts.

The densification behavior depends on several factors, namely, the magnitude of deformation load, initial relative density, aspect ratio, friction, temperature, etc. The rate of densification can be controlled to a good extent by proper control of the associated parameters. Narayan and Rajeshkannan [19] performed experimental work on sintered iron-0.35%carbon to study densification behavior during cold upsetting for various processing conditions. They evaluated the densification mechanism by examining the densification behavior against induced strain and Poisson's ratio. During the stage of deformation, the densification rate is higher due to collapse and closure of more number of pores with little advance in height strain. The second stage follows a steady state increase in densification, and very little densification was achieved in the final stage of densification due to the formation of cylindrical pores perpendicular to the load axis which do not flatten further. Preforms with lower aspect ratio undergo enhanced densification and increased friction conditions. This condition produces higher circumferential stress at the free surface and leads to increased barreling of the preform, and the hence the formability reduces.

Kandavel et al. [41] conducted experimental work on sintered low alloy P/M steels to study plastic deformation and densification behavior for various material compositions under cold upsetting, hot forging, and repressing. The addition of particulates says, Ti and Mo reduced the level of deformation and densification due to the formation of fine particulate intermetallics irrespective of mode of forming. Further studies on densification of P/M preforms were reported by Parteder et al. [42] and Shanmugasundaram et al. [43]. They established a model to describe the densification behavior of porous materials with various processing conditions and, the developed model successfully predicted the pore closure phenomena. In addition, Lu and Ma [44] carried out experimental investigations on

densification of the porous Al_2O_3 system and developed mathematical relations to predict the density over a range of deformation by considering the effect of macropores on densification. They indicated that accurate modeling of the densification behavior of porous materials, where both macro and micropores exist, will require independent consideration of both categories of pores.

2.4 Formability of P/M Preforms

To achieve a successful transformation of P/M preforms into finished products of the desired shape which is characterized by good properties for a particular application without cracks, it is essential to understand the forming limit of the particular material during deformation. The formability of materials is very important technological features in the forming process that mostly depends on the ductility of the material and associated process parameters.

Narayanasamy et al. [12] defined the term workability for powder metallurgy material as a measure of the deformation that a material can withstand prior to failure in forming process. The authors investigated the workability behavior of Al-Fe composite under triaxial stress condition and observed that there is a change in formability behavior in the composite due to different amount and size of the iron particle and different aspect ratio. Abdel-Rahman and El-Sheikh [45] investigated the effect of mean stress and effective stress to describe the workability factor on powder metallurgy compacts in upsetting process. The authors investigated the effect of relative density on the formability limit of powder compacts. Vujovic and Shabaik [46] proposed forming limit criterion by stress formability index, which relates hydrostatic stress and effective stress in metalworking processes. Tensile, compression, and torsion tests were performed to determine the forming limit curves.

Over the decades, several investigations on the upsetting of aluminium powder embedded with metallic and non-metallic inclusion are being done to analyze barreling, density variations, and formability. The barreling behavior in the cylindrical upsetting process was investigated by Selvakumar et al [47]. Narayanasamy et al. [48] conducted the experimental work on Al-Al_2O_3 composite to study the workability behavior during the cold upsetting process. They reported that the workability of a material purely depends on the

amount of ductile fracture present in the material and details of process parameters, namely initial relative density, aspect ratio, etc. Raj et al. [49] performed experimental work on Fe-C-Mn sintered composites during cold upsetting to study the effect of percentage content of carbon and manganese on the workability and strain hardening behavior. They noticed that enhanced workability for a composition at Fe-0.1C-0.5Mn due to higher initial relative density and better pore closure phenomena.

2.5 Hot deformation behavior and constitutive modelling

In the past few years, researchers have been concentrating more on the flow behavior of aluminium and its alloys for understanding to design and develop mechanical working processes. The knowledge about the hot deformation performance of the material is essential for optimizing the process parameters to get the desired products with excellent properties in forming. The flow stress of the material is influenced by deformation conditions such as temperature, strain, strain rate, the microstructure of initial materials, and composition of the materials. Generally, the flow stress of the material can affect the required energy for forming and microstructure through the work hardening (WH), dynamic recovery (DRV) and dynamic recrystallization (DRX) in the hot deformation process. Hence, it is essential to conduct an investigation of deformation process, flow stress behavior and development of the constitutive model with various process parameters for better performance of the metals.

Jin et al. [50] studied the hot deformation performance of F40MnV steel and developed flow stress model at dynamic recovery and recrystallization region. They reported that the predicted flow stress agreed with experimental data and it is applicable for forging simulation. Li et al. [51] reported the microstructural evolution of 7050 aluminium alloy during hot upsetting and revealed that the existence of dynamic recrystallization and dynamic recovery contributed to flow softening of metal. Taleghani et al. [52] performed hot compression tests on 7075 aluminium alloy to study the effect of relative green density on the flow stress. They found the peak stress to decrease with increase in deformation temperature, decreasing strain rate and relative green density. Also they developed the relationship between material constants and relative green density for predicting the peak flow stress. Guo et al. [53] conducted experimental work on Al alloy 3003 to study the hot deformation behavior during the compression test. They adopted a modified voce type model to explain the flow

stress behavior and developed constitutive equation to predict flow stress. Gangolu et al. [54] studied the flow characteristic of Al-5wt% B_4C composite during hot compression tests. They developed constitutive equations to estimate the hot deformation behavior and optimized the process parameters such as temperature and strain rates in the form of process mapping. Zhang et al. [55] conducted hot compression tests on $TiC–Al_2O_3$/Al composites to study the development of microstructure evolution and flow stress performance for various process parameters. They reported that deformation condition such as temperatures and strain rates strongly influence the flow stress behavior and observed that the softening mechanism of the composite material is different from pure aluminium. Wolla et al. [56] performed hot compression tests on Al-4%Cu to study the effect of initial relative density on flow stress. They reported that the effect of IRD, temperature and strain rate on flow stress is significant and the developed constitutive equation predicted the flow stress with minimum error and also verified with experimental results. Sun et al. [57] performed isothermal compression tests on Al–0.62Mg–0.7Si aluminium alloy to predict the flow stress by developing a constitutive model. They suggested that the modified Johnson-Cook model is best to predict flow stress behavior instead of Arrhenius- type model for easier calculation of material constants.

Narayan and Rajeshkannan [19] performed a cold upsetting test on sintered iron-0.35% carbon to study densification behavior. They mentioned that the deformation behavior of the material fabricated by powder metallurgy route is different from the cast/wrought materials (fully dense) because more numbers of pores are present in the powder preforms, thereby limiting the deformation of the materials. Further, the volume of the pores is minimized during deformation of sintered powder compacts. This will result in an increase in the density thereby its densification. In addition, Narayanasamy et al. [58] conducted cold upsetting tests on aluminium-3.5% alumina to study the effect of hardening on workability and densification. They discussed that the work hardening and flow stress of the material is increased during the plastic deformation process, thus the sintered powder compacts undergo geometric hardening and densification hardening. Venugopal et al. [20] conducted ring-compression tests on sintered iron preforms for various relative densities. They found that the friction between works and tool is more in the powder preform, which leads to increase in the nonuniformity density distribution of the P/M compacts at lower IRD. Therefore, Taleghani et al. [52] revealed that material properties of fully dense material are not acceptable for the

material which is fabricated by powder metallurgy route with the same chemical compositions.

Therefore, the modeling of the constitutive equation of hot deformation is necessary for estimating the failure, understanding the phenomenon, the cost of design, and lifetime of the product. Thus, many studies have been performed on wrought metals and its alloys as well as powder metals, to report the flow behavior of metals while hot upsetting. The results obtained from constitutive analysis of sintered preforms benefits industries/ researchers by providing information for further modeling of processing techniques such as powder extrusion and powder forging [59, 60].

2.6 Microstructure evolution and modelling of powder preforms

Better mechanical properties such as strength and hardness are necessary to increase the lifetime of the final product. These mechanical properties can be controlled by the grain size of the material. By controlling the evolution of microstructure of a material the grain size can be controlled. Microstructure evolution which controls the grain size occurs during the hot forming process and it has great influence on strength and hardness of the final product. It is essential for the designer to understand the correlation between deformation process parameters and microstructures of any engineering materials during the hot forming process, to get a good quality product. Over the last few years, researchers have been concentrating more on the grain size evolution of the metals and alloys, due to its influence on the mechanical properties of the final product. The size of the grains in the material is affected by deformation conditions such as temperature, strain and strain rate, initial microstructure, composition and initial relative density of the materials during hot upsetting. Therefore, few researchers have analyzed the effect of deformation condition on the DRX grains of the materials during the forming process. In order to get good quality product, it becomes necessary to know the relationship between deformation conditions and the DRX grains of the metals and alloys during the hot upsetting process.

A number of researchers [22–24, 61] have revealed the effect of deformation conditions on the microstructures and DRX grains of cast/wrought material (fully dense) and established the mathematical model between DRX grain size and Zener–Hollomon parameter.

Shaban and Eghbali [23] performed experimental work on Nb-Ti microalloyed steel during hot torsion tests. They reported that the DRX grains are very sensitive to deformation conditions and the authors developed relationships between DRX grain size, critical strain, and steady state strain and Zener–Hollomon parameter. Kodzhaspirov and Terentyev [24] studied the microstructure evolution of superalloy during a torsion test and a mathematical model was developed between DRX grain size and Zener–Hollomon parameter, which gives the predicted DRX grain size. Further studies on microstructure evolution and DRX grain size of Inconel 625 superalloy were reported by Li et al. [22] and Geo et al. [61]. They reported that the effect of deformation temperatures on nucleation mechanisms of DRX is significant and size and volume fraction of DRXed grains increases with temperature.

There is little information found relating to microstructures and the DRX grains evolution of powder metals during hot upsetting. Therefore, it is essential to study the microstructure evolution and DRX grains behavior of powder preforms with deformation conditions such as temperature and strain rate for estimating the failure, understanding the phenomenon, the cost of design, and lifetime of the product. The deformation, microstructure and the DRX grains behavior of the material are different for products fabricated by powder metallurgy route compared to cast/wrought material (fully dense) because more numbers of pores are present in the powder preforms [19]. During the plastic deformation process work hardening and flow stress of the material is increased, thereby powder preforms undergo geometric hardening and densification hardening [58]. The nonuniformity density distribution in the P/M compacts at lower IRD is observed due to higher friction between the tool and works due to the substantial amount of pores present in the P/M preforms [20]. Therefore, the deformation, microstructure and DRX grains behavior of the cast/wrought material (fully dense) information are not suitable for porous materials with the same chemical compositions [52]. Therefore, it is fascinating to investigate the microstructure evolution and modeling to predict the DRX grain size by considering the influence of porosity and other process parameters such as temperature and strain rate on microstructure evolution.

2.7 Gaps in the literature survey

After thoroughly going through the literature, some of the major limitations in the existing literature on P/M parts processing are given as below;

i. There is a necessity to develop process map for Al-B_4C composite preforms involving a different percentage of B_4C and process condition like forming temperature and strain rate. There is limited literature available on the study of formability of sintered Al-B_4C preforms related to its process parameters such as temperature, strain rate, and porosity.

ii. The effect of boron carbide content on densification behavior of sintered Al-B_4C preforms has not been explained.

iii. The deformation behavior of sintered Al-B_4C preforms with various initial relative densities at different temperature and strain rate conditions has not been explained.

iv. The densification behavior of sintered Al-B_4C performs during upsetting at high-temperature has not been reported.

v. No or limited studies have been reported on developing constitutive relations considering the effect of porosity to predict the flow stress of sintered Al-B_4C preforms during upsetting at high-temperature.

vi. There is limited research related to the microstructure evolution of sintered Al-B_4C composite considering the effect of temperature, strain rate, initial relative density and deformation degree.

vii. Mathematical relations to predict the DRX grain size of sintered Al-B_4C composite after plastic deformation considering the effect of temperature, strain rate, and initial relative density are limited.

2.8 Objectives

Based on the identified gaps on the available information in the literature related plastic deformation of P/M components during hot working, the current investigations were formulated to study the formability characteristics, densification and deformation behavior, and microstructure evolution of sintered Al-B_4C composite under hot upsetting. The main objectives of the thesis are

I) To study the hot workability and densification behavior of sintered powder metallurgy Al-B_4C preforms during upsetting.

II) To Model the flow behavior of sintered Al-4%B_4C composite during high-temperature upsetting.

III) To analyze the grain size evolution of sintered Al-4%B_4C composite subjected to plastic deformation at elevated temperature.

IV) To model the microstructure of dynamically recrystallized grain size of sintered Al-4%B_4C composite during hot upsetting.

A series of hot upsetting studies were carried out on sintered Al-B4C preforms under various deformation conditions to evaluate the formability behavior, microstructure evolution and developed a model to predict the flow stress and grain size of sintered Al-B_4C preforms. The detailed procedure of the present investigation is shown in Fig. 2.1.

2.9 Summary

This chapter provides a detailed survey of literature relevant to the current investigation such as densification behavior, formability behavior, microstructure analysis and modeling. The gaps existing in the current knowledge of deformation and densification behavior, and microstructure evolution of P/M preforms has been identified. Based on the literature review and literature gaps four objectives were defined. Finally, the detailed procedure of the present investigation was explained through the flowchart diagram.

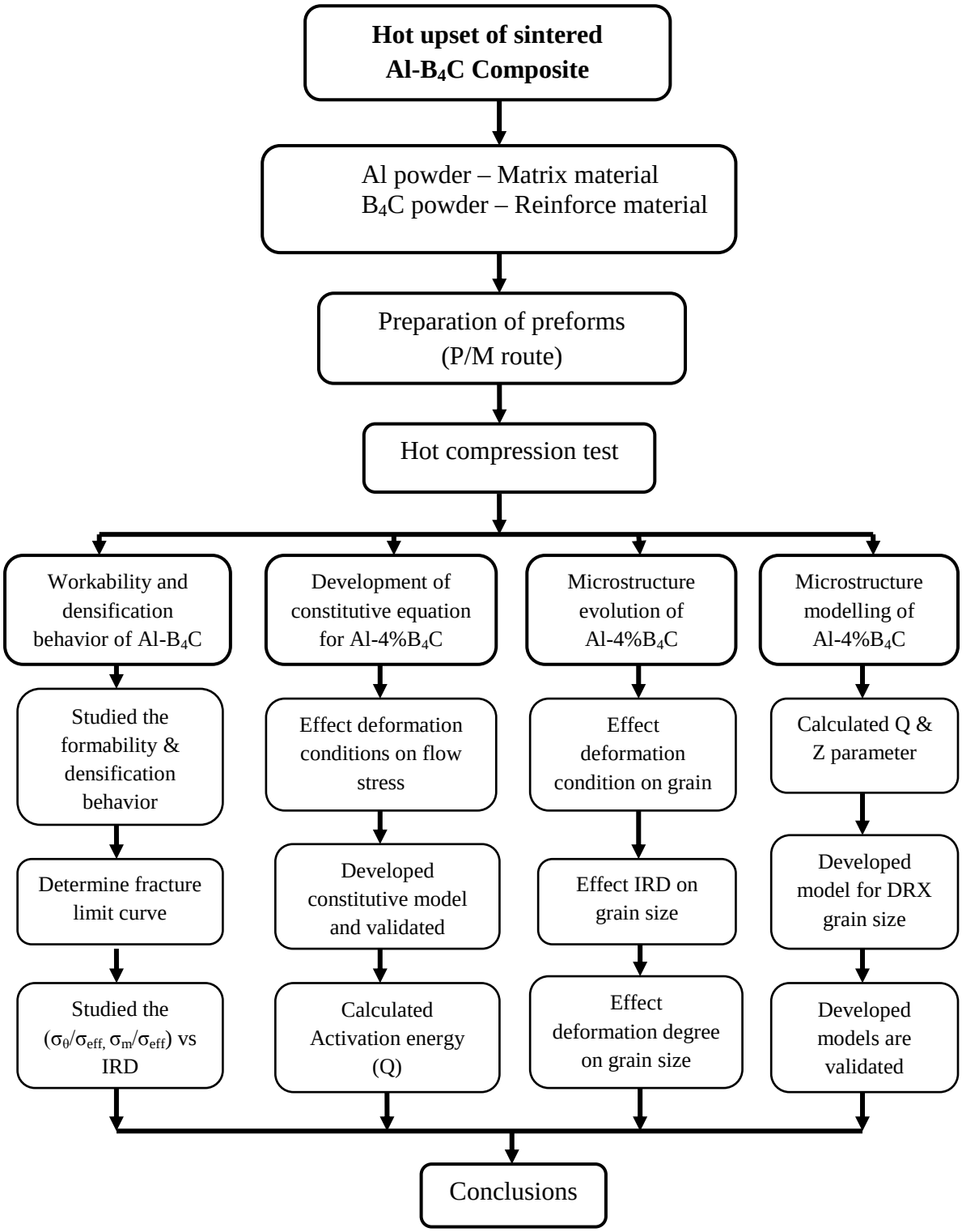

Fig: 2.1 Flowchart diagram showing the detail procedure of the present investigation

CHAPTER 3

Experimental Details

This chapter describes the details of experiments conducted for the present investigation which include material selection, sample preparation, hot upsetting test and metallurgical analysis by an optical microscope.

3.1 Selection of materials for the study

Generally, Al metal is used as a matrix material due to its lightweight, high elastic modulus, high strength, and good wear resistance and ceramics are used as reinforcement material because it provides sufficient strength, and stiffness to the metal matrix [62]. B_4C is one the hardest and lightest (density = 2.51 g/cc) material than other commercial reinforcement [63]. It has other attractive properties such as good thermal stability, high wear and impact resistance and good chemical stability hence B_4C widely used as cermets and armor materials. B_4C is known to be neutron absorber and due to this Al-B_4C composite is used as fuel storage tank material in nuclear industries [64, 65]. The reason for selecting these materials is the vast applications of their alloys/composites in nuclear industries, defense, and electronic industries.

The B_4C has high hardness and low density (2.51 g/cc) than the Al due to this reason Al-B_4C composite finds the application as armor plates [66]. Moreover, literature studies

related to the deformation, densification, and microstructure evolution studies of the candidate materials are scarce. P/M processed components have superior practical and industrial importance than the corresponding wrought material with the same composition. The material chosen for the present investigations are pure aluminium (Al) powder and boron carbide (B_4C) powder. Atomized Al powder of particle size 325 mesh size and purity of 99% with a maximum of 0.53% insoluble impurities was procured from SR Laboratories, Mumbai, India. B_4C powder of particle size 325 mesh size has been used as reinforcement and procured from supertek dies, Delhi, India. Boron carbide was analyzed for its purity, and it was found to be 99.61% and the rests are insoluble impurities.The Al and B_4C material properties are tabulated in Table 3.1.

Table 3.1 Properties of Aluminum and Boron carbide

Parameters	**Al**	**B_4C**
Molecular Weight (g/mol.)	26.98	55.25
Theoretical Density (g/cm3)	2.7	2.51
Color	Dark gray	Black or Dark gray
Crystal Structure	FCC	Rhombohedral
Tensile strength (MPa)	90	569
Compressive Strength (MPa)	330	5687
Yield Strength (MPa)	50	360
Ultimate Strength (MPa)	68.9	430
Hardness (MPa)	42	44100
Young's Modulus (GPa)	70	472
Shear Modulus (GPa)	26	195

3.1.1 SEM and EDAX

The particle size and shape of the Al and B_4C were characterized by using scanning electron microscope (SEM). The morphology of the Al and B_4C powder as shown in Figs. 3.1

and 3.2 respectively, are found to be flaky and irregular in shape. The morphology and Energy-Dispersive X-ray Analysis plot of as-received B_4C particles are shown in Fig. 3.3. EDX peaks corresponding to the B_4C were found in good agreement. Figure 3.4 shows the photograph of the scanning electron microscope.

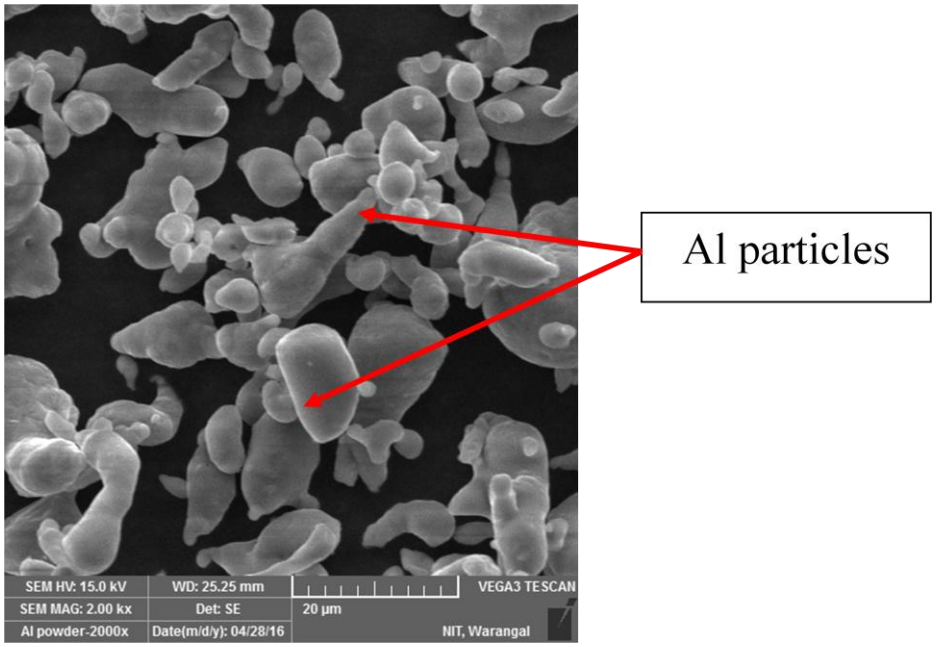

Fig. 3.1 SEM image of aluminium particles

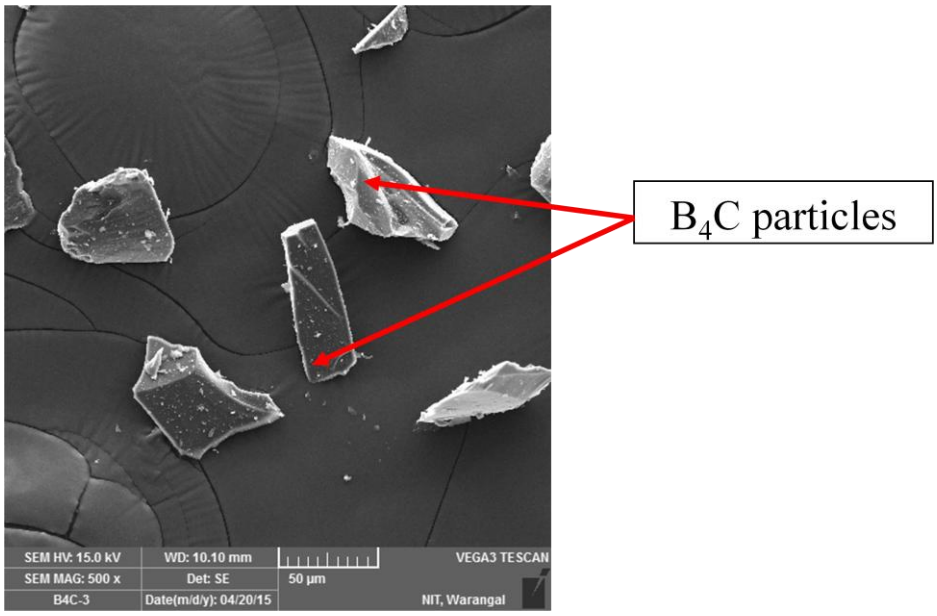

Fig. 3.2 SEM image of boron carbide particles.

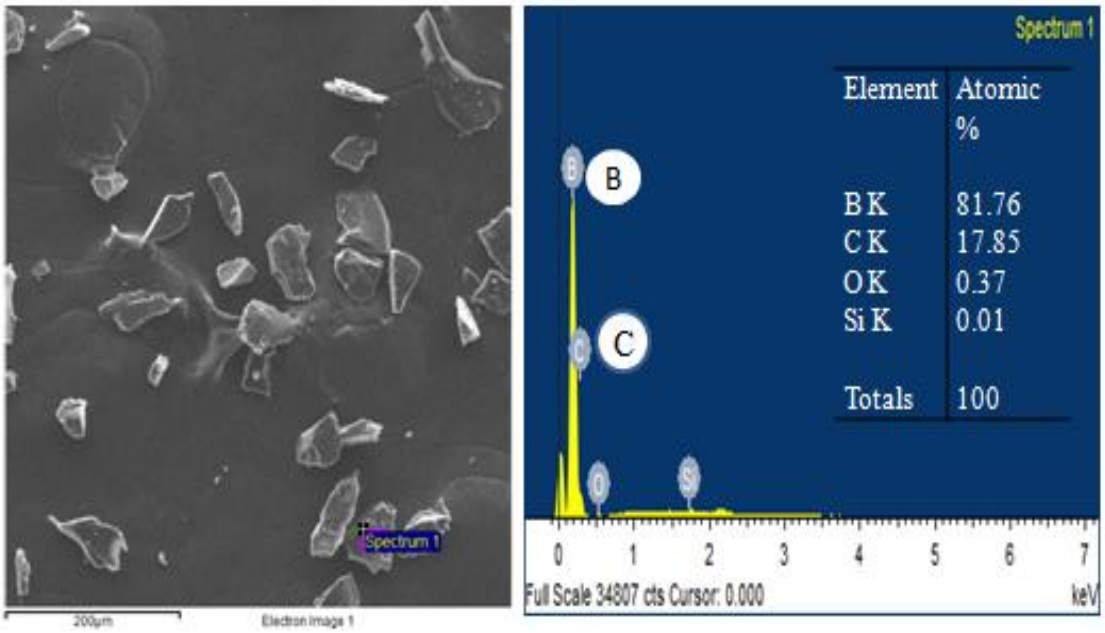

Fig. 3.3 EDX analysis of B_4C

Fig. 3.4 Shows the photograph of the Scanning Electron Microscope (SEM).

3.2 Specimen preparation

3.2.1 Mixing of powders

The required mass of Al and B_4C powder (2wt%, 4wt% and 6wt%) was accurately weighed using electronic mass balance (± 0.01 mg repeatability) and mixed in a pot mill for 1 hr to get a homogeneous mixture. The homogeneous powder mix has an advantage of improving sinter-ability of the powder and making the ejection of compaction easy. Figure 3.5 shows the morphology of the blended Al-B_4C was analyzed with the help of SEM and it was found to be homogeneous.

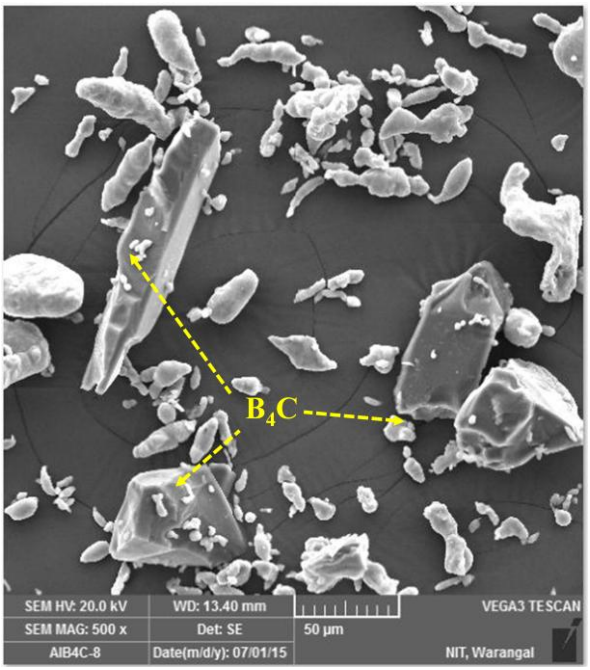

Fig. 3.5 SEM image of Al-B_4C composition

3.2.2 Compaction

Among several compaction methods, uniaxial die compaction was used for preparing powder compacts as it is by far most economical and important method. Uniaxial die compaction involves pressing of powder mix within a die cavity by the action of an upper punch at a constant velocity while the lower punch remains fixed. Figure 3.6 shows the schematic diagram of uniaxial die compaction technique adopted in the current work for

sample preparations. A hydraulic press of 50 ton capacity was used for preparing Al-B_4C compacts. In this process, the required amount of the Al-B_4C powder mix was properly poured into the die with its bottom punch inserted from the lower part of the die and top punch was introduced from the upper side. The recommended compaction pressures of 170 MPa, 226 MPa and 282 MPa were applied to the die assembly to achieve compacts with initial relative densities of 80%, 85% and 90%, respectively. The geometry of the compacts was 15 mm in diameter and height for the hot compression test. After completion of compaction step, the green compacts were carefully ejected from the die by making the die upside down and applied ejection load ranging from 50 MPa to 80 MPa. Zinc stearate was applied as a lubricant to reduce interface friction between the metal powders and die. It is expected to be decomposed during the sintering cycle due to its low operating temperature, and its small residues left after sintering does not impart a considerable effect on the final parts. Figure 3.7 shows the photograph of the compaction die, punch and butt which is used for preparing powder compacts for the compression test.

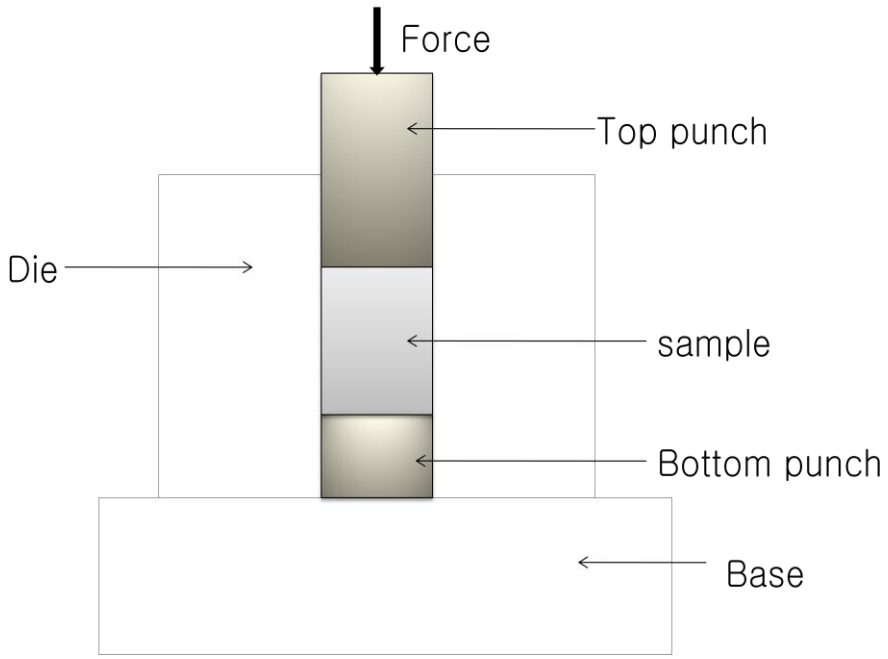

Fig. 3.6 The schematic diagram of uniaxial die compaction technique

The green compact density was measured by using the Archimedes principle with an accuracy of ± 1% and the equation is described as follows:

$$Preform\ density = \frac{w_a}{w_a - w_w} \quad (3.1)$$

During preform density measurement, Teflon sheet was used for making the surface of the preforms to prevent the infiltration of water into the pores and its density was considering during calculation procedure.

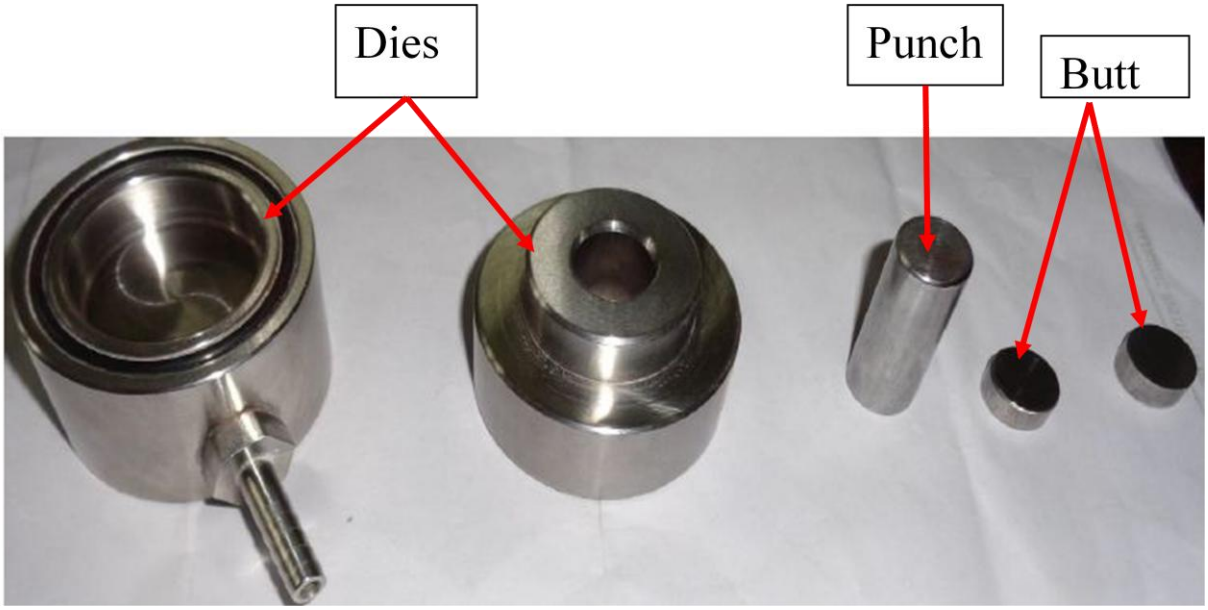

Fig. 3.7 Photographs of 15 mm die, top and bottom punches for preparing powder compacts for compression tests.

3.2.3 Sintering

The photographs of electric muffle furnace, which were used for sintering, as shown Fig. 3.8. Sintering of green compacts is done with the purpose of achieving all possible final strength, hardness and dimensions, therefore the green compacts were sintered in an electric muffle furnace at a temperature of 550±10 ^{o}C about 60 min. then the compacts were allowed to cool to room temperature within the furnace. During the sintering process, there is some shrinkage in dimensions that leads to increasing in the density of the consolidated body. The sintered density of the preforms was measured using Archimedes principles with an accuracy of ± 1%, and the photographs of few sintered preforms are shown in Fig. 3.9.

Fig. 3.8 Photograph of electric muffle furnace

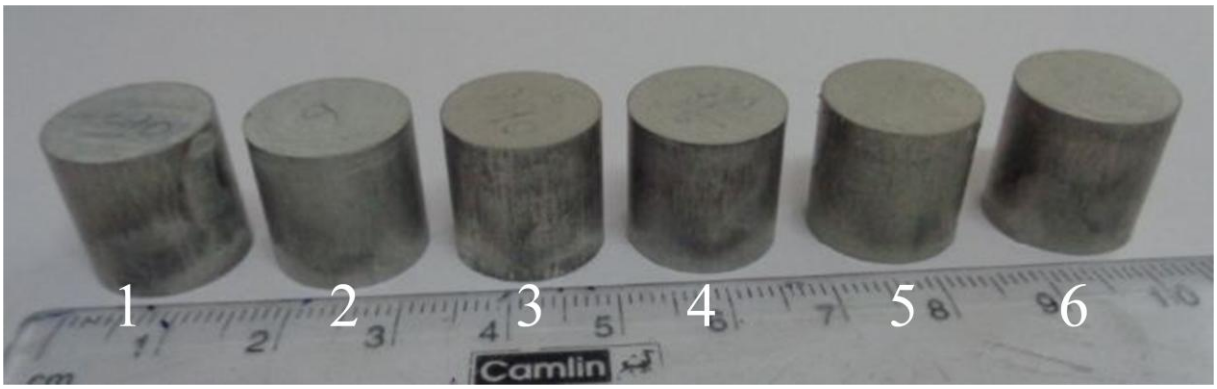

Fig. 3.9 Photographs of sintered preforms before deformation

3.3 Hot compression test

3.3.1 Formability and densification behavior

The hot compression tests were conducted with the purpose of determining the formability and the densification behavior at various deformation temperatures and percentage of B_4C in preforms for 90% of initial relative density. For this, the initial dimensions, such as diameter (D_o), height (H_o) and density (ρ_o) of the preforms were measured and recorded after completion of a sintering process. Figure 3.10 shows the pictorial representation of the geometry of specimen before and after deformation. The hot deformation tests were conducted on different Al-B_4C compositions preforms such as 2%B_4C, 4%B_4C and 6%B_4C between two flat dies in a hydraulic press (50 T) for various deformation temperatures such as 200 ^oC, 300 ^oC, 400 ^oC and 500 ^oC.

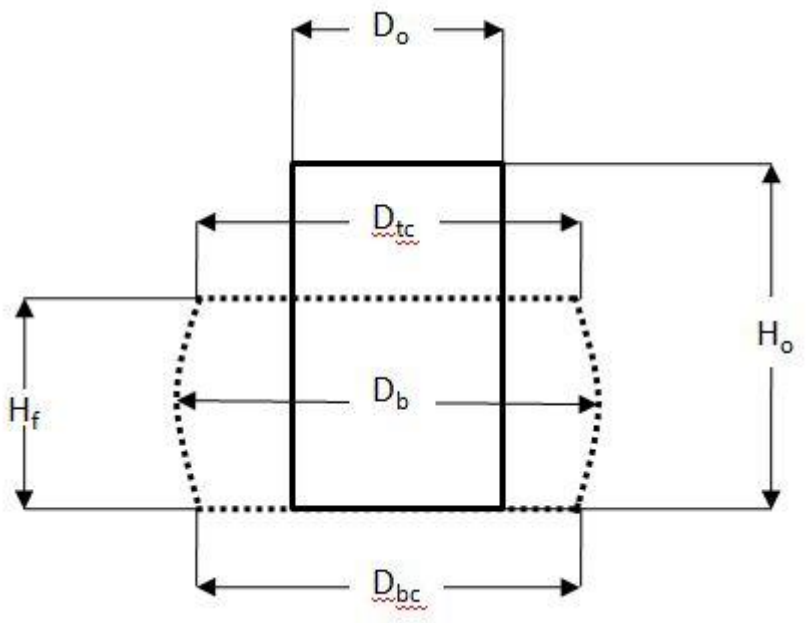

Fig. 3.10 Geometry of the specimen before and after deformation

Figure 3.11 shows the photograph of hydraulic press used for the compression test. The hot deformation process was carried out inside a split type electrical resistance muffle furnace provided on the bed of the hydraulic press. The furnace temperature and the sample temperature were measured by two thermocouples, one is placed inside the furnace and

another is placed near to preform, respectively. Soaking time of 30 min was provided to the preforms after getting the required test temperature before the deformation. The incremental compressive load was applied till the initiation of crack on the free surface of the preforms. For each compression test condition, six specimens of the same dimension were prepared and made to deform to different strain levels. The deformation load and displacement continuously monitored by the data acquisition system connected to the hydraulic press and data were recorded after deformation. After each step of deformation, the final dimensions, such as height (H_f), top contact diameter (D_{tc}), bottom contact diameter (D_{bc}), and bulge diameter (D_b) were measured by digital vernier caliper, and density was measured by Archimedes principle. Figure 3.12 presents the photographs of preforms before and after deformation test to different strain levels.

Fig. 3.11 Photograph of hydraulic press (50 ton capacity)

Fig. 3.12 Photograph of preforms before and after deformation test

3.3.2 Development of constitutive equation

Hot compression tests were conducted to evaluate the deformation behavior and to develop constitutive equation to predict the flow stress for preforms of various initial relative densities deformed at different deformation temperatures and strain rates. The blended Al-4wt.%B_4C powder was uniaxially cold pressed into a cylindrical compact with diameter and height of 15 mm. The various IRDes of 80%, 85% and 90% are obtained by applying different compaction load. The initial dimensions such as diameter and height were measured by using vernier calipers and relative density was measured by Archimedes's principle with an accuracy of ± 1%. The compression test was performed on the hydraulic press (capacity of 50 tons) between two flat dies at various temperatures of 300 ^oC, 400 ^oC and 500 ^oC and strain rates of 0.1 s^{-1}, 0.2 s^{-1} and 0.3 s^{-1} and for IRDes of 80%, 85% and 90%. During the compression test, cylindrical compacts were heated (soaking time) for 30 min at test temperature to have homogenous heat. The incremental compressive load was applied to the cylindrical compacts until the appearance of first visible cracks on the circumference of the compacts. From the data – log unit of hydraulic press the load–displacement data were recorded.

3.3.3 Microstructure evolution and modelling

Hot upsetting tests were performed to evaluate the microstructure behavior and to develope0 mathematical models to predict the DRX grain size for preforms of various initial relative densities deformed at different deformation temperatures and strain rates. For this the blended Al-4wt.%B_4C powder was compacted into 15 mm diameter and height disks in a hydraulic press and suggested compaction pressures were applied to get different IRDes of 80%, 85% and 90%. The sintered Al-4%B_4C preforms were compressed between two flat dies in a hydraulic press. The upsetting tests were performed at different deformation temperatures of 300 ^oC, 400 ^oC and 500 ^oC and strain rate of 0.1 s^{-1}, 0.2 s^{-1}, and 0.3 $s^{-1}$and for various IRDes. The procedure of hot upsetting tests is shown in Fig. 3.13. During upsetting test the preforms were soaked for 30 min. at a test temperature to get uniform temperature distribution in the preforms and the incremental compressive load was applied until cracks appear on the free surface of the preforms. The samples were then immediately quenched in water to obtain uniform microstructure. And also, to know the effect of deformation degree on the DRX grain

size the sintered Al-4wt.%B_4C preforms were compressed with a deformation degree of 0 (undeformed preform), 10%, 20%, 30%, 40%, and 50% (fracture preform) at different deformation temperatures of 300 ^oC, 400 ^oC and 500 ^oC and strain rate of 0.1 s^{-1}, 0.2 s^{-1}, and 0.3 $s^{-1}$and for various IRDes. The load–displacement data were recorded in a computer equipped with a data logger unit of the hydraulic press.

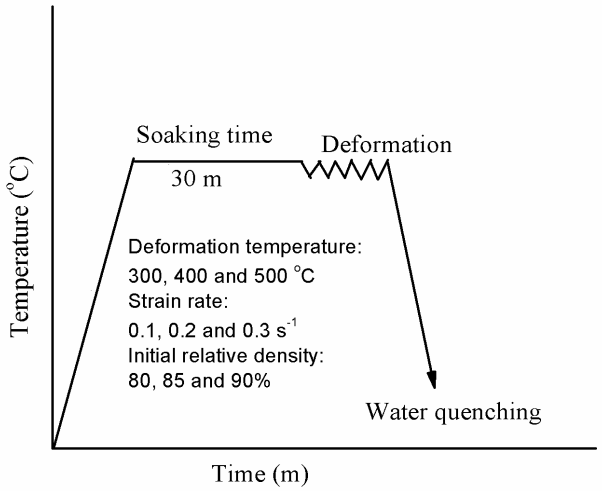

Fig. 3.13 Experimental procedure for hot upsetting tests

3.4 Metallurgical analysis

The microstructures of sintered Al-4wt.%B_4C preforms were characterized by the optical microscope (OM) after the upsetting process. Figure 3.14 shows the photograph of an optical microscope. The compressed preforms were mechanically polished with different grade of emery paper followed by final polish on disk polishing machine to get a mirror-like finish. The polished preforms were etched in a Keller's reagent for 60 sec. The compressed sintered Al-4wt.%B_4C preforms microstructures were evaluated by the optical microscope (OM) for different deformation conditions such as temperature, strain rate, initial relative density and deformation degree. The grain size of preforms was measured by an intercept line method for different IRDes, temperatures and strain rates. The average DRXed grain size of sintered Al–4wt.%B_4C preforms for different deformation conditions were tabulated in Table 3.2. Figure 3.15 shows the microstructure of sintered Al–4wt.%B_4C preforms before the upsetting test and it is observed that the reinforcement is uniformly distributed in the matrix.

The initial microstructures of the sintered Al-4wt.%B_4C preforms for different IRDes are shown Fig. 3.16 (a-c). It is noticed that the grain size is equiaxed and it is measured approximately 16.85 µm, 22.55 µm and 25.02 µm for different IRDes of 80%, 85% and 90%, respectively.

Table 3.2 Effect of temperature and strain rates on grain size (µm) of P/M Al-4wt.%B_4C composite for various IRDes.

Def. Tem. (K)	έ (s^{-1})	IRD = 80%	IRD = 85%	IRD = 90%
		d_m (µm)	d_m (µm)	d_m (µm)
573	0.1	7.74	9.09	15.16
673	0.1	8.42	9.69	16.19
773	0.1	8.84	10.31	16.87
573	0.2	7.50	8.76	14.76
673	0.2	8.17	9.41	15.71
773	0.2	8.72	10.01	16.61
573	0.3	7.40	8.57	14.57
673	0.3	7.89	9.34	15.47
773	0.3	8.48	9.84	16.56

Fig. 3.14 Photograph of optical microscope.

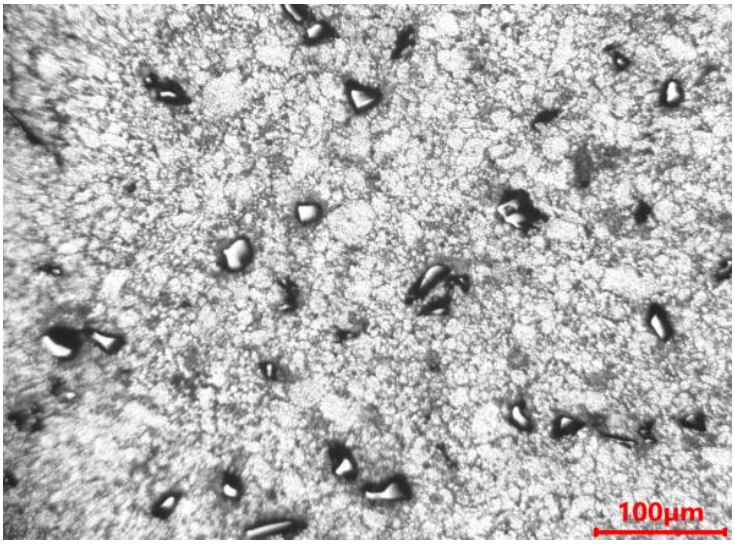

Fig. 3.15 Microstructure of sintered Al-4wt.%B_4C preforms

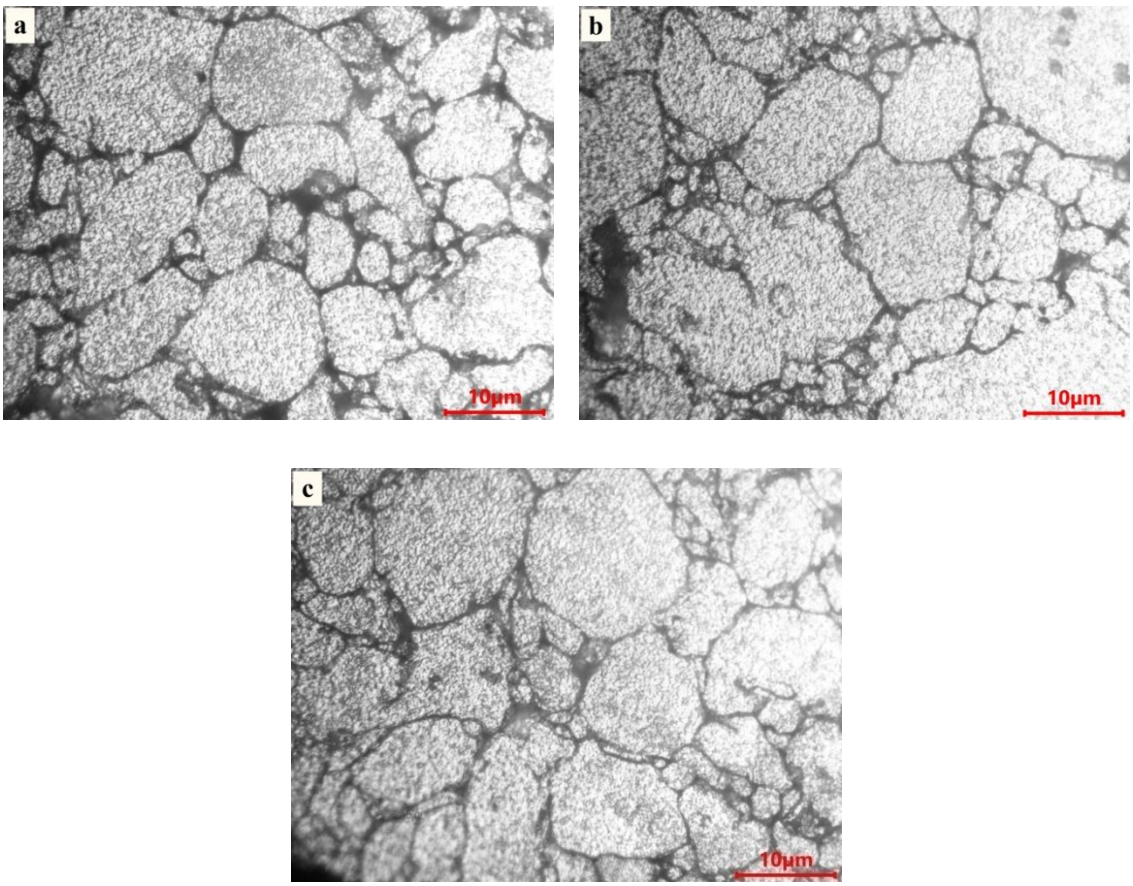

Fig. 3.16 (a-c) Microstructure of sintered Al-4wt.%B_4C preforms prior to deformation for different IRDes (a) 80% (b) 85% (c) 90%.

3.5 Theoretical analysis

The upsetting parameters were determined by the following mathematical expressions under the tri–axial stress state condition. The expressions for the normal stress (σ_z), normal strain (ε_z), hoop stress (σ_θ), hoop strain (ε_θ), hydrostatic stress (σ_m), effective stress (σ_{eff}) and formability stress index (β_σ) used in the present work can be stated as below.

According to Abdel-Rahman and El-Shiekh [45], axial strain (ε_z), axial stress (σ_z) component of P/M composite preforms can be calculated from the following equations.

$$\varepsilon_z = \ln\left(\frac{H_f}{H_o}\right) \tag{3.2}$$

$$\sigma_z = \frac{load}{contact\ \ surface\ \ area} \tag{3.3}$$

And the hoop strain is

$$\varepsilon_\theta = \varepsilon_r = \ln\left(\frac{D_f}{D_o}\right) \tag{3.4}$$

Raj et al. [36] presented the hoop strain (ε_θ) as stated below which includes the forged bulged diameters (D_b) and forged contact diameters of the preforms.

$$\varepsilon_\theta = \ln\left[\frac{2D_b^2 + D_c^2}{3D_o^2}\right] \tag{3.5}$$

Where D_c is the average surface contact diameter of the preform after the deformation

Kumar et al. [67] expressed the state of stress as

$$\alpha = \frac{d\varepsilon_\theta}{d\varepsilon_z} = \frac{(2+R^2)\sigma_\theta - R^2(\sigma_Z + 2\sigma_\theta)}{(2+R^2)\sigma_Z - R^2(\sigma_Z + 2\sigma_\theta)} \tag{3.6}$$

When α, the Poisson's ratio, R, the relative density and σ_z, the axial strain are known, the hoop stress (σ_θ) can be calculated from the Eq. (3.6) as

$$\sigma_\theta/\sigma_z = \left[\frac{2\alpha + R^2}{2 - R^2 + 2R^2\alpha}\right] \quad (\text{Where } \alpha = \frac{d\varepsilon_\theta}{d\varepsilon_z}) \tag{3.7}$$

The hydrostatic stress is calculated by using cylindrical coordinates ($\sigma_\theta = \sigma_r$) as

$$\sigma_m = \frac{\sigma_r + \sigma_\theta + \sigma_z}{3} = \frac{2\,\sigma_\theta + \sigma_z}{3} \tag{3.8}$$

$$\frac{\sigma_m}{\sigma_z} = \frac{1}{3}\left(1 + \frac{2\sigma_\theta}{\sigma_z}\right) \tag{3.9}$$

Narayanasamy et al. [68] presented the effective stress as stated below.

$$\sigma_{eff}^2 = \frac{\sigma_z^2+\sigma_\theta^2+\sigma_r^2-R^2(\sigma_z\sigma_\theta+\sigma_\theta\sigma_r+\sigma_r\sigma_z)}{2R^2-1} \quad (3.10)$$

Since $\sigma_\theta = \sigma_r$ for cylindrical axisymmetric upsetting operation, the Eq. (3.11) becomes

$$\sigma_{eff}^2 = \frac{\sigma_z^2 + 2\sigma_\theta^2 - R^2(\sigma_z\sigma_\theta + \sigma_\theta^2 + \sigma_z\sigma_\theta)}{2R^2 - 1}$$

$$\sigma_{eff} = \left[\frac{\sigma_z^2+2\sigma_\theta^2-R^2(\sigma_\theta^2+2\sigma_z\sigma_\theta)}{2R^2-1}\right]^{0.5} \quad (3.11)$$

Vujovic and Shabaik [46] experimentally proved the role of spherical (hydrostatic) component of the stress state on fracture called formability stress index 'β_σ' and is defined as follows:

$$\beta_\sigma = \left(\frac{3\sigma_m}{\sigma_{eff}}\right) \quad (3.12)$$

This formability stress index (β_σ) determines the fracture limit as explained in [46].

3.6 Summary

In this chapter the experimental details, which includes the selection of material, specimen preparation, hot compression test, macrostructure analysis by optical microscope and characterization of the investigated material have been discussed. The as-received aluminium and boron carbide properties such as shape, size, and compositions were studied. Detailed explanations have been given about the fabrication of Al-B_4C composite material. The initial microstructure of Al-B_4C composite was studied for different deformation conditions. The hot deformation test was carried out at various deformation conditions such as the percentage of B_4C content, initial relative density, temperature, strain rate and strain. The upsetting parameters such as normal stress (σ_z), normal strain (ε_z), hoop stress (σ_θ), hoop strain (ε_θ), hydrostatic stress (σ_m), effective stress (σ_{eff}) and formability stress index (β_σ) were explained which is used in this work.

CHAPTER 4

Hot Workability and Densification Behavior of Sintered Powder Metallurgy Al-B_4C Preforms During Upsetting

4.1 Introduction

Formability is a criterion that gives the extent of deformation that a material can withstand the induced internal stress prior to fracture in forming. Abdel-Rahman and El-Sheikh [45] reported that the densification plays a greater role in the formability of P/M material. It is very significant to note that the extents to which materials are formed without fracture and achievable maximum relative density are the major desirable characteristics for forming applications. During plastic deformation of porous materials, there is a substantial flow of metals into pores that lead to pore shrinkage and, hence the density changes. For the case of wrought material, the volume of the material before and after deformation is the same. However, the same is not true for porous materials, and it is essential to know the final density of the material which decides the performance and service life. Hence, the formability stress index and relative density as a function of strain induced are a worthwhile study. Generally, the products which are manufactured by forming process subjected to near to maximum limit of formability. Therefore, due to the industrial significance attached to Al–B_4C composite, a

detailed investigation on the workability and densification of sintered Al–B_4C composite preforms have been done at the elevated temperatures.

Experimental work was performed to study the workability and the densification behavior of a porous Al–B_4C preforms in this chapter. Hot upsetting tests have been carried out on Al–B_4C powder metallurgy preforms having an initial preform density of 0.9 and having different B_4C compositions of 2%, 4% and 6%. The samples were compressed in a hydraulic press under varying deformation temperatures such as 200 ^oC, 300 ^oC, 400 ^oC and 500 ^oC under the tri–axial stress state condition. The instantaneous deformation load corresponding to instantaneous height was recorded from the data acquisition system of the hydraulic press. Therefore, based on these data, true height strain (ε_z) and true axial stress (σ_z) were computed using Eqns. (3.2) and (3.3) for preforms with various deformation temperature and B_4C content. The hoop stress, hydrostatic stress, effective stress and formability stress index (β_σ) were calculated using Eqns. (3.7), (3.8), (3.11) and (3.12). Thereafter instantaneous densities of the preforms were measured using Archimedes principle for each specimen from the instantaneous area and instantaneous height.

4.2 Densification behavior

4.2.1 Effect of axial strain on relative density

Figs. 4.1– 4.3 shows the effect of axial strain (ε_z) on relative density (R) for different deformation temperatures, such as 200 ^oC, 300 ^oC, 400 ^oC and 500 ^oC of the various Al–B_4C preforms under the tri-axial stress state conditions with 0.9 initial relative density. The density of preforms increases with increasing deformation temperature irrespective of percentage of B_4C in preforms. It can be seen from the plot that the densification achieved by the preforms with 2%B_4C is found to be more than the 4%B_4C preform for any deformation temperature. The improved densification is achieved by the closure of pores. However, the densification is showing an inverse relationship with the addition of B_4C. The material flow starts from the center and ends in the outer periphery. It is inferred that the closure of pore is obstructed by dispersion of the B_4C present in the matrix. Thus, with the addition of more and more amounts of B_4C the densification of the preforms reduces. Further, the curves have been divided into three different stages of densification mechanism relating to the axial strain. In

the first stage, the densification rate is faster with little enhancement of axial strain. The proportion of pores in the initial stage of deformation is larger than the later stage as the pores are found to close continuously during the deformation process. As the deformation load is spent on closing the pores on the initial stages of deformation, the stage-1 of the deformation curve has a steep increase in densification with a little amount of axial strain. Densification rate gradually decreases during the stage-2 of the deformation path with increase in axial strain, meaning that the pore size decreases with the increase in axial deformation and finally collapses in stage-3. It is also noticed that very little amount of density was achieved during the final stage of the deformation curve, as by this time, the pores would have got elongated perpendicular to the applied load. This elongated shaped pore increases the material's resistance to the deformation. Hence, higher relative density was attained before the preforms fractured at the outer surface.

From the densification curves, it is found that the amount of deformation and densification behavior is different for the different percentage of B_4C content in the composite for various deformation temperatures. The highest deformation and densification were obtained for preforms with a lower percentage of B_4C content for any given axial strain compared to other preforms with the higher percentage of B_4C content. The flow behavior of preforms decreases with the addition of B_4C in the Al metal matrix as B_4C particles blocked the free movement of Al particles from the center towards the edge. As a result, hoop stress is more in the case of Al with lower percentage of B_4C. It is also observed from the plots that the attained relative density is higher for the 500 ^oC deformation temperature irrespective of the percentage of B_4C content in Al matrix. A maximum relative density of 0.95 was obtained at 500 ^oC deformation temperatures for 2%B_4C composite.

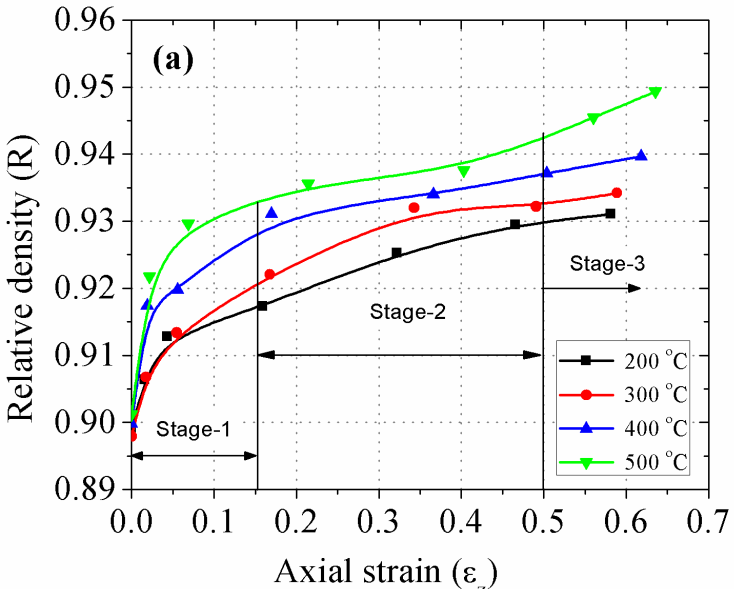

Fig. 4.1 Effect of axial strain (ε_z) on relative density (R) of 2%B_4C composite for various temperatures under the tri–axial stress state condition.

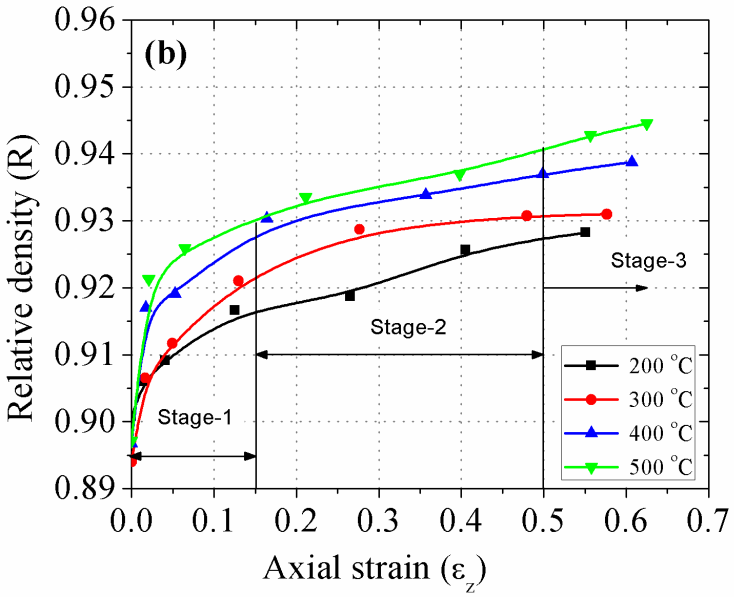

Fig. 4.2 Effect of axial strain (ε_z) on relative density (R) 4%B_4C composite for various temperatures under the tri–axial stress state condition.

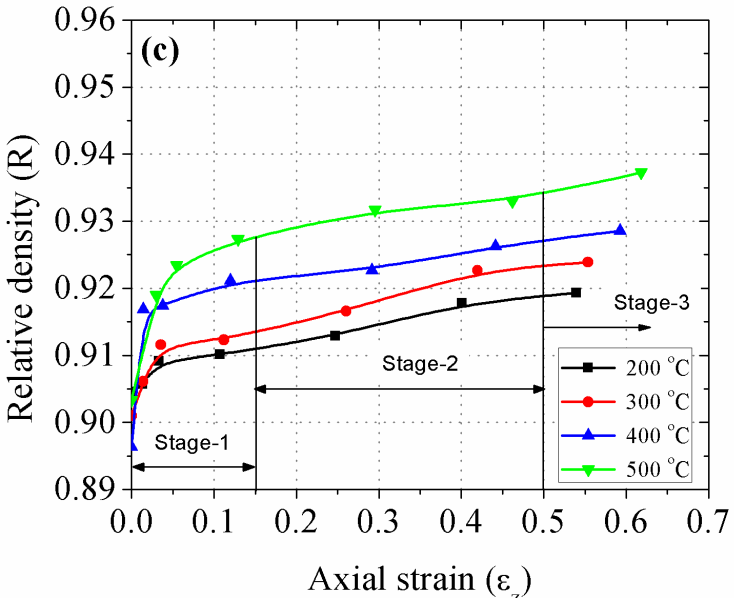

Fig. 4.3 Effect of axial strain (ε_z) on relative density (R) 6%B_4C composite for various temperatures under the tri–axial stress state condition.

4.2.2 Effect of relative density (R) on stress ratio parameter

Figs. 4.4 – 4.6 show the stress ratio parameter ($\sigma_\theta/\sigma_{eff}$), against relative density (R) for the Al–B_4C preforms with initial relative density of 0.9 and for different deformation temperatures, such as 200 ^oC, 300 ^oC, 400 ^oC and 500 ^oC under the tri–axial stress state conditions. It is noticed that the stress ratio parameter increased with increasing relative density irrespective of the deformation temperature and B_4C content in the Al composite. The stress ratio parameter was found to increase along with the hoop stress. The material displaced from the core to the outer periphery of the preforms by the successive axial loads leads to closure of pores. As a result, the increase of stress in the material will be stressed more along the periphery of the preform rather than the axial direction. The stress ratio parameter increased with increasing relative density and deformation temperature irrespective of the percentage of B_4C in the Al composite. As the deformation temperature increases, the flowability of the material from the center to the free surface also increases thus more densification. Furthermore, it is observed from the graphs that the stress ratio parameter decreases with the addition of an amount of B_4C percentage in the Al composite. The highest relative density and stress ratio parameter were attained for the Al–2%B_4C composite at

500 ^{o}C deformation temperature. The same kind of trend is followed in the case of stress ratio parameters (σ_m/σ_{eff}) as shown in Fig. 4.7 – 4.9.

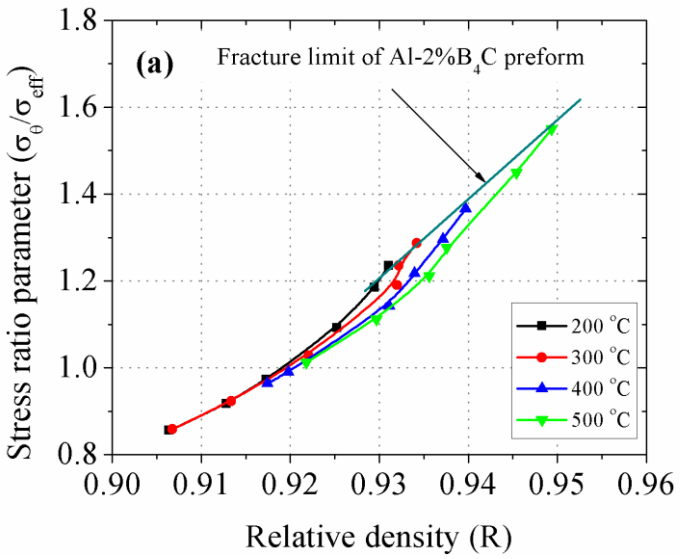

Fig. 4.4 Effect of relative density (R) on stress ratio parameter ($\sigma_\theta/\sigma_{eff}$) of 2%$B_4C$ composite for various temperatures under the tri–axial stress state condition.

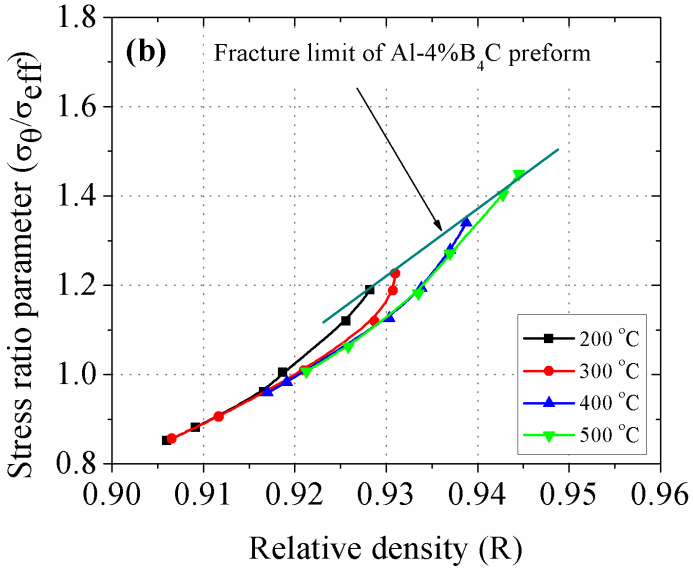

Fig. 4.5 Effect of relative density (R) on stress ratio parameter ($\sigma_\theta/\sigma_{eff}$) of 4%$B_4C$ composite for various temperatures under the tri–axial stress state condition.

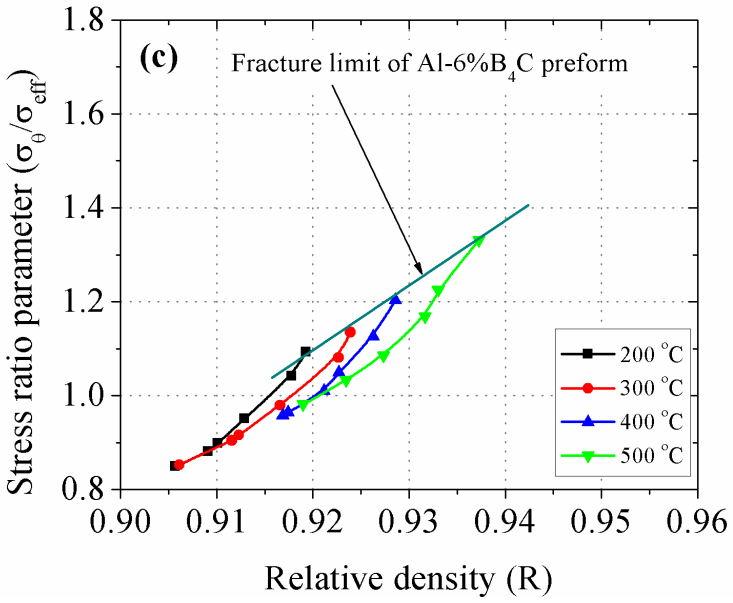

Fig. 4.6 Effect of relative density (R) on stress ratio parameter ($\sigma_\theta/\sigma_{eff}$) of 6%$B_4C$ composite for various temperatures under the tri–axial stress state condition.

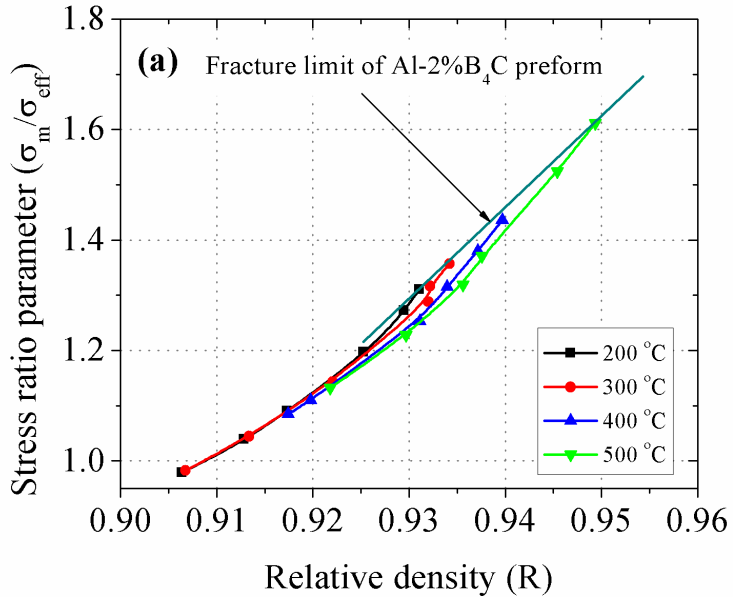

Fig. 4.7 Effect of relative density (R) on stress ratio parameter (σ_m/σ_{eff}) of 2%B_4C composite for various temperatures under the tri–axial stress state condition.

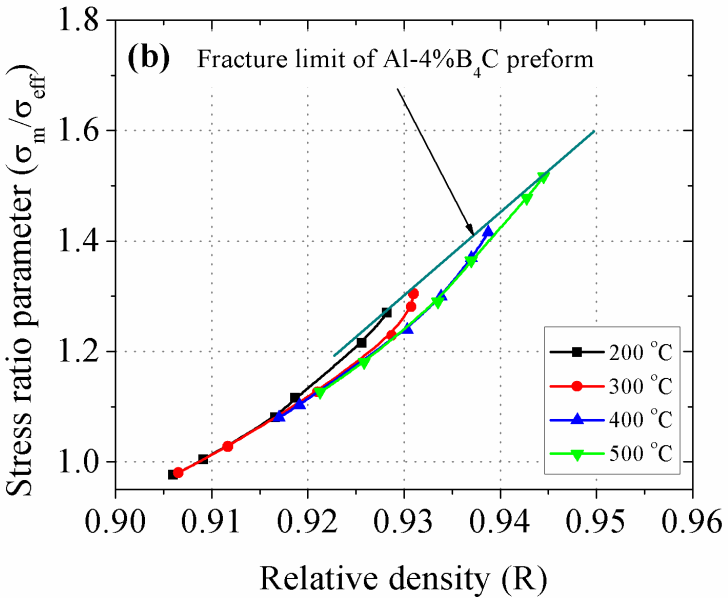

Fig. 4.8 Effect of relative density (R) on stress ratio parameter (σ_m/σ_{eff}) of 4%B_4C composite for various temperatures under the tri–axial stress state condition.

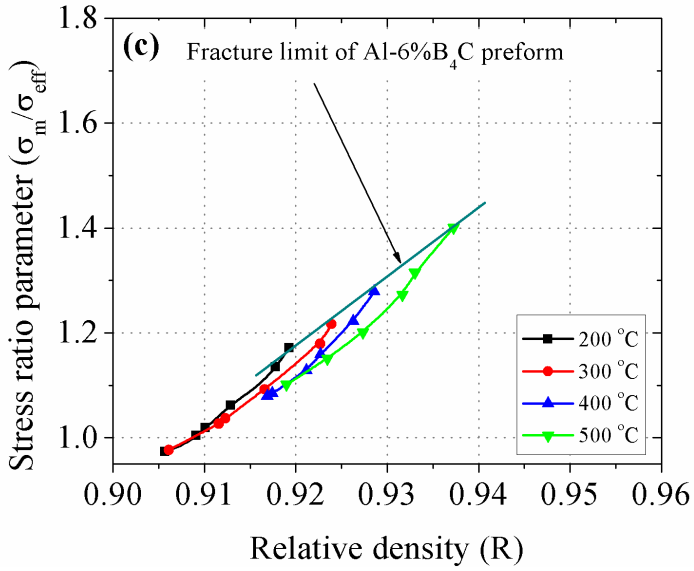

Fig. 4.9 Effect of relative density (R) on stress ratio parameter (σ_m/σ_{eff}) of 6%B_4C composite for various temperatures under the tri–axial stress state condition.

4.3 Formability behavior

4.3.1 Effect of axial strain on formability stress index (β_σ)

Figs. 4.10 – 4.12 give the effect of axial strains on the formability stress index (β_σ) for different deformation temperatures, such as 200 ^oC, 300 ^oC, 400 ^oC and 500 ^oC of various Al–B_4C preforms with initial relative density of 0.9 under the tri-axial stress state conditions. The formability stress index increases with increasing axial strains irrespective of the deformation temperature and percentage of B_4C content. It is noticed that the formability stress index varies with all investigated deformation temperatures and with the addition of B_4C content in the aluminium metal matrix. From Fig. 4.10, it is observed that the intersection point increases with increasing deformation temperature with respect to axial strain. The flow behavior of the preforms increased from the center to the outer periphery with increasing deformation temperature. At the higher deformation temperatures preforms densified more than the lower deformation temperatures due to the reduction of pore size at the higher deformation temperatures. Therefore, higher formability of the material is obtained at higher deformation temperatures irrespective of the B_4C content.

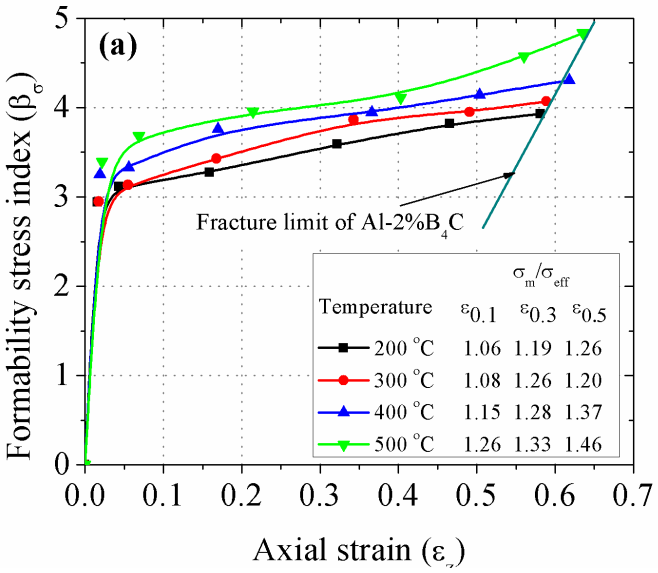

Fig. 4.10 Effect of axial strains (ε_z) on formability stress index (β_σ) of 2%B_4C composite for various temperatures under the tri–axial stress state condition.

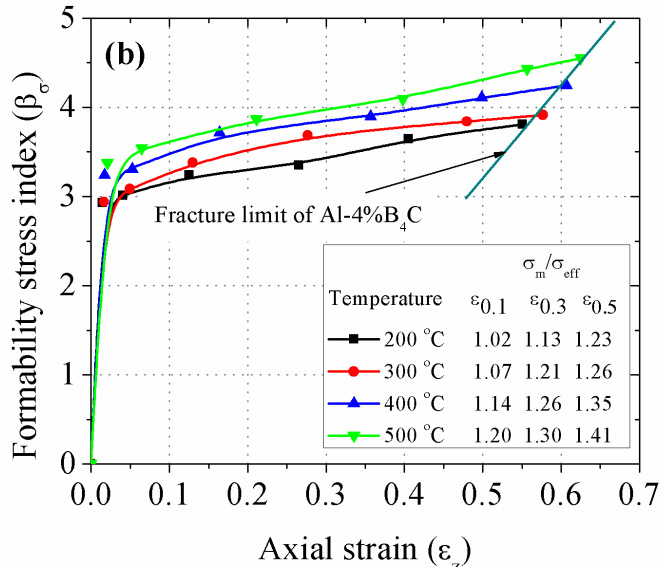

Fig. 4.11 Effect of axial strains (ε_z) on formability stress index (β_σ) of 4%B_4C composite for various temperatures under the tri–axial stress state condition.

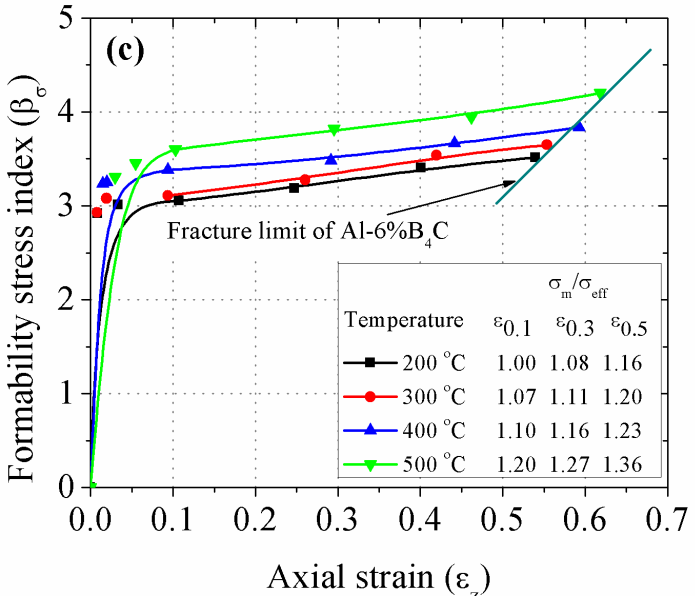

Fig. 4.12 Effect of axial strains (ε_z) on formability stress index (β_σ) of 6%B_4C composite for various temperatures under the tri–axial stress state condition.

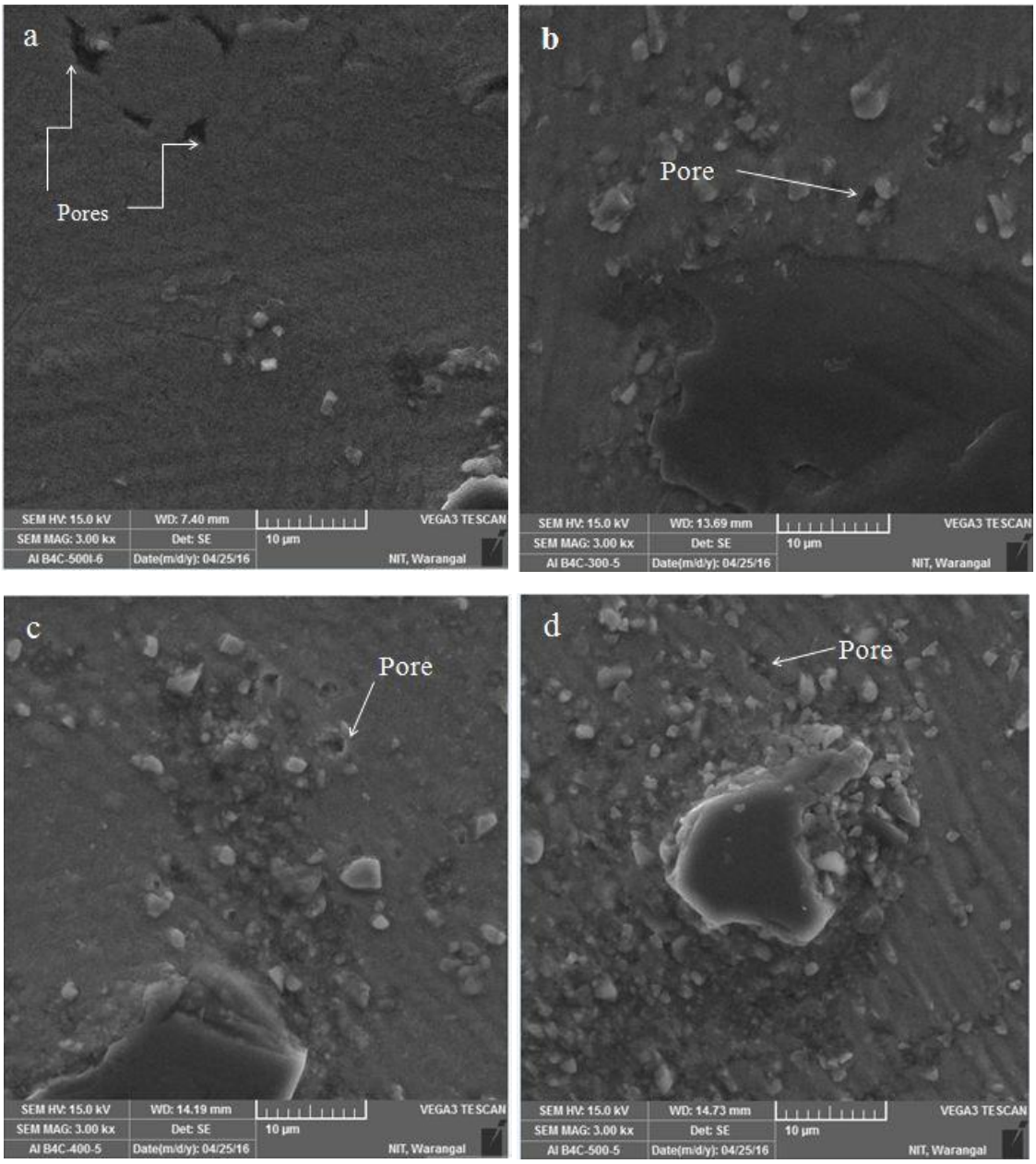

Fig. 4.13 The SEM morphology of (a) sintered Al–6%B_4C before deformation, (b) sintered Al–6%B_4C after deformation at 300 ^oC, (c) sintered Al–6%B_4C after deformation at 400 ^oC, (d) sintered Al–6%B_4C after deformation at 500 ^oC preforms.

It can be observed from Figs. 4.10 – 4.12 that with increasing B_4C content in the aluminium matrix, the fracture limit curves moves towards the left side. It is also observed that the preforms with high percentage of B_4C content in the aluminium matrix undergo an early fracture. The flow behavior of Al is obstructed in composite due to the presence of B_4C particles; hence the material is prone to early initiation of fracture with the addition of high

percentage of B_4C content in Al metal matrix, resulting in lower formability. Moreover, it is observed that the lowest formability stress index for any given axial strain is the prefroms with 6% of B_4C contents irrespective of the temperature. The formability stress index is found to be higher in the case of 2%B_4C preforms and 500 ^oC deformation temperature and it fractures at higher axial strain. For 2%B_4C preforms the relative density is higher for any given axial strain due to the small pore size compared to other composites (4%, and 6% B_4C preforms), thus leading to high formability stress index for 2%B_4C. The relative density increases with respect to a large amount of deformations and the same is observed by other authors [14, 69]. The stress ratio (σ_m/σ_{eff}) values obtained for different strains (0.1, 1.3, and 0.5) provided in the graphs indicates that the formability stress index increases with increase in axial strains. Apart from the strain, preforms having the aspect ratio of 0.5 densified more due to the presence of fine pores (see Fig. 4.13), and such preforms were found to crack along the free surface of the preforms.

4.2.1 Effect of relative density on formability stress index (β_σ)

Figs 4.14 – 4.16 show the effect of relative density on the formability stress index of the Al–B_4C preforms with initial relative density of 0.9 for different deformation temperatures, such as 200 ^oC, 300 ^oC, 400 ^oC and 500 ^oC under the tri–axial stress state conditions. It is noticed from the plots that the formability stress index changed with respect to the attained relative density irrespective of the deformation temperatures and composition of B_4C in the Al composite. From Fig. 4.14, it is noticed that the formability curves increase with increasing deformation temperature with respect to the relative density and the formability stress index. With increasing deformation temperature the diffusion rate between atoms is more that leads to minimize the pore content in the preforms. Hence, the material density increases with increasing deformation temperature and it facilitates the increase the formability of the material irrespective of the B_4C content in the aluminium matrix. The fracture limit curve shifted down to the left side with increasing B_4C content in the aluminum matrix as shown in Figs. 4.14–4.16. It represents that the formability stress index and relative density decreases by the addition of B_4C content in the aluminum matrix. The porosity level increases with increasing B_4C content in the aluminum matrix, and it initiates the early fracture of the preforms and lower formability. The highest relative density and formability is

attained in the Al–2%B_4C composite for the 500 ^oC deformation temperatures for any given axial strains.

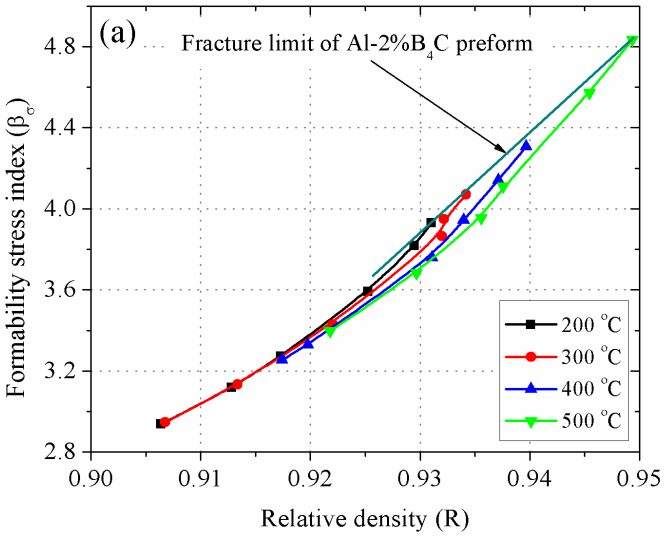

Fig. 4.14 Effect of relative density (R) on formability stress index (β_σ) of 2%B_4C composite for various temperatures under the tri–axial stress state condition.

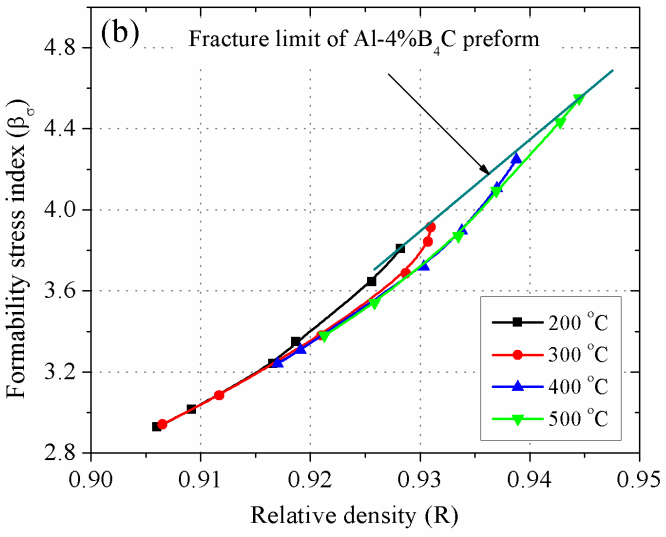

Fig. 4.15 Effect of relative density (R) on formability stress index (β_σ) of 4%B_4C composite for various temperatures under the tri–axial stress state condition.

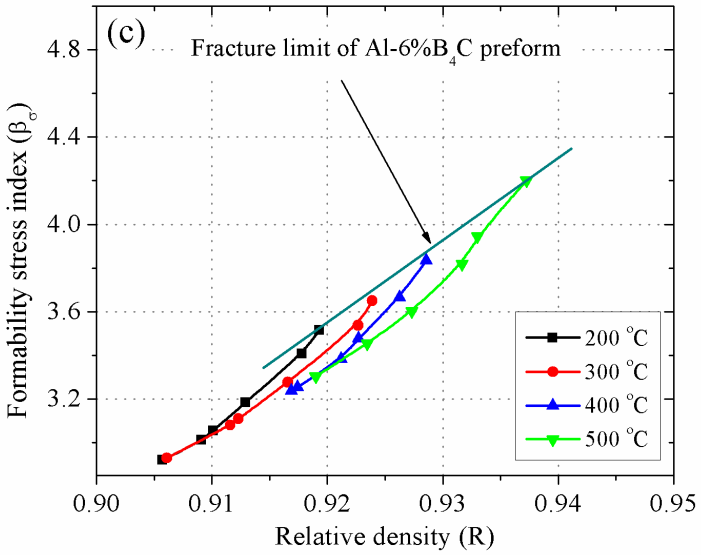

Fig. 4.16 Effect of relative density (R) on formability stress index (β_σ) of 6%B_4C composite for various temperatures under the tri–axial stress state condition.

4.4 Summary

The workability and densification behavior of sintered Al–B_4C composites (2%, 4% and 6% of B_4C) with 0.9 initial preform density have been studied by upsetting test over different deformation temperatures such as 200 ^oC – 500 ^oC under the tri–axial stress state condition. The workability and densification behavior of Al–B_4C preforms were analyzed till the initiation of cracks on the outer surface of the preform. The experimental results were analyzed for the various deformation parameters such as axial strain, relative density, formability stress index and different stress ratio parameter under the tri–axial stress state condition. The formability and densification behavior were discussed with the axial strain (ε_z) during the hot upsetting process. The relationships between the various stress ratio parameters ($\sigma_\theta/\sigma_{eff}$, σ_m/σ_{eff}) and formability stress index (β_σ) as a function of the relative density under the tri–axial stress state condition was established.

CHAPTER 5

Modelling Flow Behavior of Sintered Al–4wt.%B_4C Composite During High–Temperature Upsetting

5.1 Introduction

In the previous chapter, the hot workability and densification behavior of sintered Al–B_4C composite for different percentage of B_4C in the matrix was studied. It is noticed that the flow stress of sintered Al–B_4C preforms were also affected by the deformation conditions such as temperature, strain, strain rate and initial relative density during the upsetting process. In addition, the initial relative density of sintered composite may behave differently for various deformation conditions. Hence, it is necessary to study the flow behavior of aluminium and its alloys for a better understanding of metal forming processes. Only limited work related to the hot upsetting behavior of sintered material considering the various IRD and deformation conditions is found. Therefore, in this chapter the experimental works have been conducted on sintered Al–4wt.%B_4C composite to study the flow stress behavior for various IRDes and various deformation conditions during hot upsetting.

The main aim of this work is to estimate the effect of initial relative density (IRD), deformation temperature, and strain rate on the hot deformation behavior and development of constitutive equations for predicting the hot deformation behavior. For this purpose, upsetting tests have been performed in a hydraulic press for obtaining true stress–true strain curve data

of sintered Al–4wt.%B_4C composites. The compression test was performed on the hydraulic press at various temperatures of 300 ^oC, 400 ^oC and 500 ^oC and strain rates of 0.1s^{-1}, 0.2s^{-1} and 0.3s^{-1} and for IRDes of 80%, 85% and 90%. From the data–log unit of hydraulic press the load–displacement data are recorded.

5.2 Hot deformation curves

The true stress (σ) – true strain (ε) curves of sintered Al–4wt.%B_4C preforms with different IRDes for various temperatures and strain rate have been demonstrated in Figs. 5.1–5.9. It is noticed that the flow stress is varied for different temperatures, strain rates, and IRDes. Fig. 5.1 shows the relationship between σ–ε of sintered Al–4wt.%B_4C preforms with IRD of 80% and strain rate of 0.1 s^{-1} for various temperatures such as 300 ^oC, 400 ^oC and 500 ^oC. It is noticed that the flow stress decreased with increase in temperature because of thermal softening and the highest flow stress was found at low temperature. The same kind of behavior is observed for other preforms irrespective of strain rates and IRD of sintered Al–4wt.%B_4C preforms as shown in Figs. 5.1–5.9. The flow stress difference is more between 400 ^oC and 500 ^oC deformation temperatures for 80% IRD irrespective of the strain rate. During the deformation process with lower IRD, the dislocation movement increases with increase in deformation temperature and it probably peaks at 500 ^oC. In Fig. 5.1, the graphs have been drawn between σ–ε with IRD of 80% for various temperatures and strain rates. It is noticed that the flow stress increased with increasing strain rate because the resistance offered by the material increases with increase in strain rate; hence the higher amount of load is needed to deform the material.

Same kind of behavior is observed in the remaining IRD of 85% and 90% preforms as shown in Figs. 5.4 – 5.9 respectively. Further, it is noticed that the flow stress increases with increase in IRD irrespective of the temperatures and strain rates. This is because; the dislocation movement is decreased with increase in IRD and leads to increase in the deformation difficulties of preforms. Hence higher amount of load is required to deform the preforms.

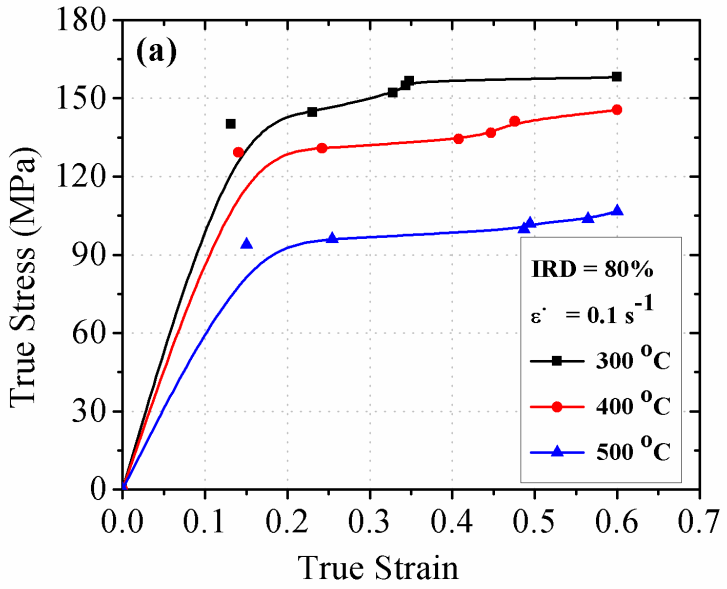

Fig. 5.1 True stress–true strain curves of Al–4wt.%B_4C composite during hot compression with IRD of 80% at strain rate (a) 0.1 s^{-1}.

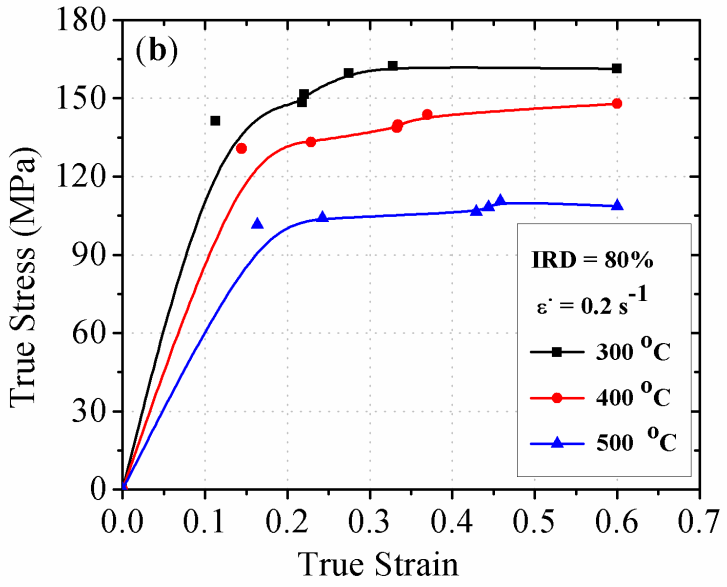

Fig. 5.2 True stress–true strain curves of Al–4wt.%B_4C composite during hot compression with IRD of 80% at strain rate (b) 0.2 s^{-1}.

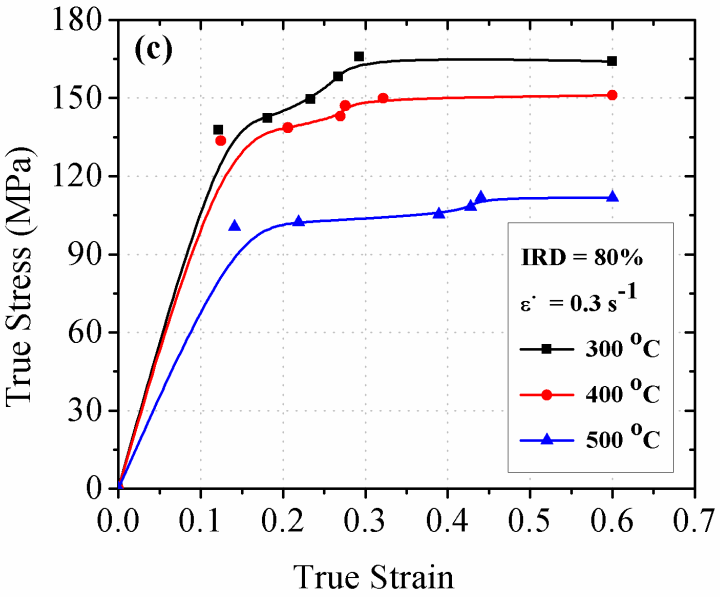

Fig. 5.3 True stress–true strain curves of Al–4wt.%B_4C composite during hot compression with IRD of 80% at strain rate (c) 0.3 s^{-1}.

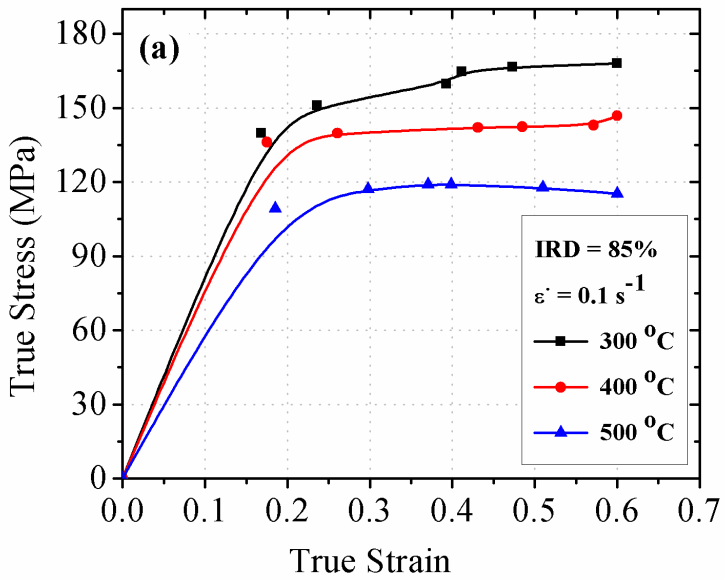

Fig. 5.4 True stress–true strain curves of Al–4wt.%B_4C composite during hot upsetting with IRD of 85% at strain rate (a) 0.1 s^{-1}.

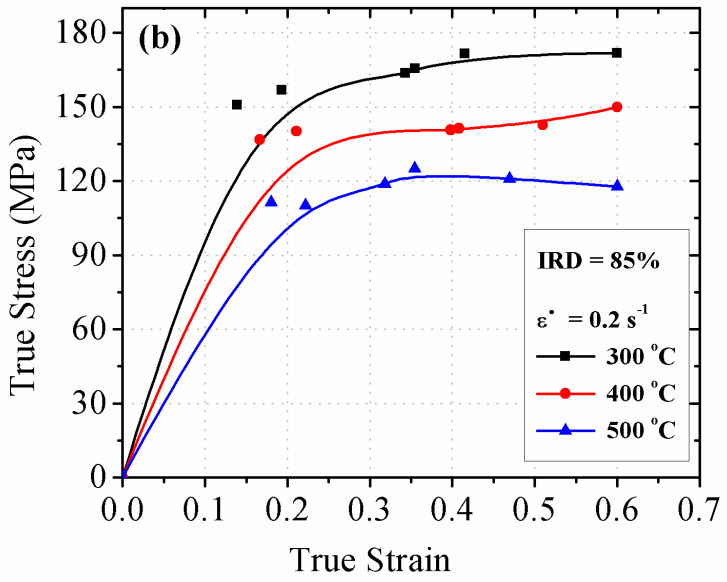

Fig. 5.5 True stress–true strain curves of Al–4wt.%B_4C composite during hot upsetting with IRD of 85% at strain rate (b) 0.2 s^{-1}.

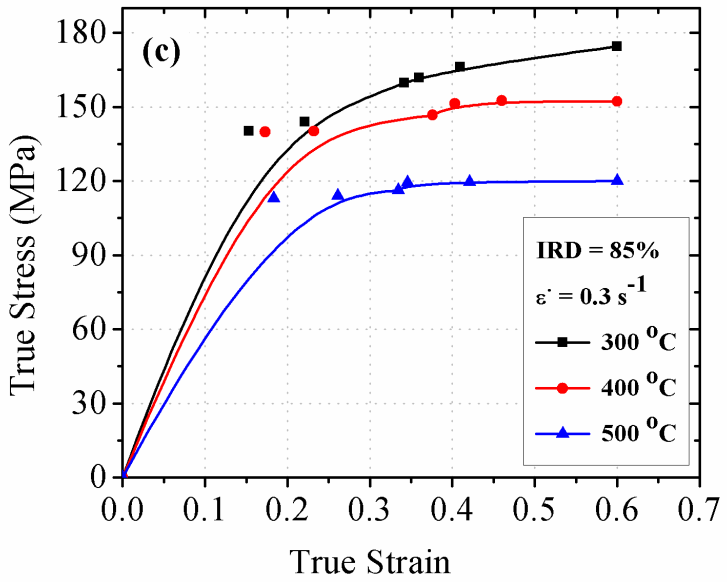

Fig. 5.6 True stress–true strain curves of Al–4wt.%B_4C composite during hot upsetting with IRD of 85% at strain rate (c) 0.3 s^{-1}.

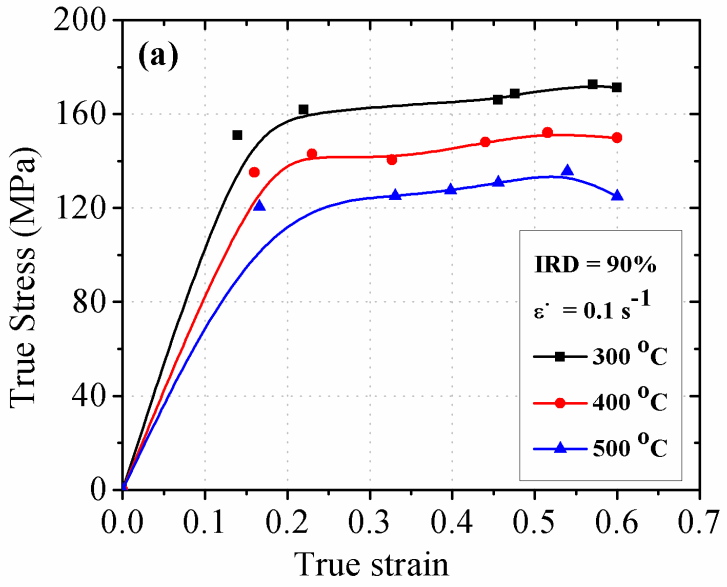

Fig. 5.7 True stress–true strain curves of Al–4wt.%B_4C composite during hot compression with IRD of 90% at strain rate (a) 0.1 s^{-1}.

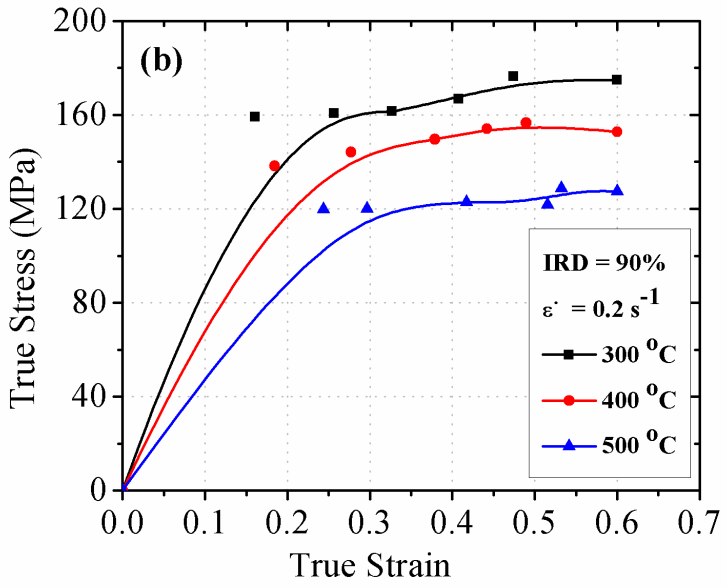

Fig. 5.8 True stress–true strain curves of Al–4wt.%B_4C composite during hot compression with IRD of 90% at strain rate (b) 0.2 s^{-1}.

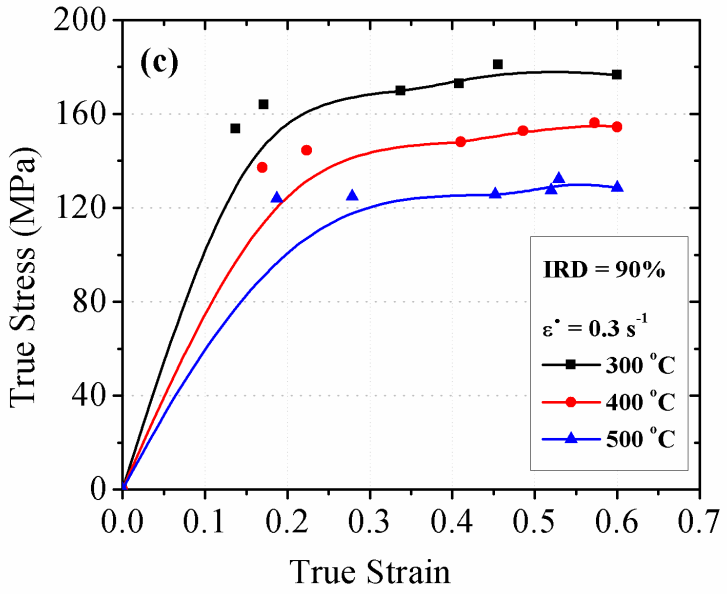

Fig. 5.9 True stress–true strain curves of Al–4wt.%B_4C composite during hot compression with IRD of 90% at strain rate (c) 0.3 s^{-1}.

At the initial stage, the σ–ε curves increase rapidly and then exhibit peak flow stress (PFS) at certain strain values and after that, it is constant until the end of the strain values due to work hardening and dynamic softening. Sun et al. [57] revealed that in the early part of the deformation curves, dislocations multiplied considerably and the work hardening mechanism plays an important role leading to rapid increase in flow stress for smaller strain values. The σ–ε curves are controlled by the work hardening before starting the DRX. After the PFS value, the σ–ε curves become constant until higher strain values thus show the dynamic softening process. DRX phenomenon is followed by the DRV, which describes that the WH rate decreased with increasing strains values. According to Taleghani et al. [52], during hot upsetting, the hardening and softening mechanism happens in the powder preforms at higher temperatures. Irrespective of the IRD, the dynamic softening is more at a higher temperature and lower strain rate as the mobility of grain boundaries increases and it accelerates the growth of DRX grains at the same condition [70]. Moreover, the effect of work hardening mechanism is partially or completely neutralized at higher strain values. Thus, the σ–ε curves become flat with a nearly zero slope at higher strain values.

5.3 Development of constitutive model of Al–4wt.%B_4C composite

Generally, the Arrhenius equation is commonly adapted to describe the relationship between the flow stress and deformation condition [71, 72]. This equation could be expressed as follows:

$$\acute{\varepsilon} = A\,[\sinh(\alpha\sigma)]^n\, exp\left(-Q/_{RT}\right) \tag{5.1}$$

Where έ = strain rate (s^{-1}); σ = flow stress (MPa); n = material constant; Q = activation energy of hot deformation (KJ mol^{-1}); R = universal gas constant (8.314 J mol^{-1} K^{-1}); T = absolute temperature in Kelvin (K); A and α are material constants.

For low stress levels (ασ < 0.8), $\sinh(\alpha\sigma)^n \cong \alpha\sigma$, for high stress levels (ασ > 1.2), $\sinh(\alpha\sigma) \cong 0.5\ \exp(\alpha\sigma)$ and hyperbolic sine law stress function can be used for any (ασ) values. Therefore, the Arrhenius equation can be rewritten as:

$$\acute{\varepsilon} = A_1\sigma^n \exp\left(-Q/_{RT}\right) \qquad [\alpha\sigma < 0.8] \tag{5.2}$$

$$\acute{\varepsilon} = A_2\ \exp(\beta\sigma)\ exp\left(-Q/_{RT}\right) \qquad [\alpha\sigma > 1.2] \tag{5.3}$$

$$\acute{\varepsilon} = A\,[\sinh(\alpha\sigma)]^n \exp\left(-Q/_{RT}\right) \qquad [\alpha\sigma \text{ taking any values}] \tag{5.4}$$

Where, $A_1 = A\alpha^n$, $A_2 = A/2^n$, and α = β/n are constants in which the β and n values are calculated from the experimental results.

In addition, Zener and Hollomon [72] explained the effect of temperature and strain rate on hot deformation behavior can be evaluated through a single parameter Z, Zener–Holloman parameters (Z):

$$Z = \acute{\varepsilon} \exp\left(Q/_{RT}\right) \tag{5.5}$$

By substituting Eq. (5.4) into Eq. (5.5), it gives:

$$Z = A\,[\sinh(\alpha\sigma)]^n \tag{5.6}$$

Furthermore, the σ can also be written in terms of Z and material constants by solving Eq. (5.6), according to the definition of the hyperbolic sine function.

$$\sigma = \frac{1}{\alpha}\ln\left\{\left(\frac{Z}{A}\right)^{\frac{1}{n}} + \left[\left(\frac{Z}{A}\right)^{\frac{2}{n}} + 1\right]^{\frac{1}{2}}\right\} \tag{5.7}$$

5.3.1 Calculation of material constants

As reported by Wolla et al. [56] at higher temperatures, there is no effect of strain values on flow stress curves and it is remaining unchanged at higher values. As a result, the effect of strain on the development of above mentioned Eq. (5.7) is not considered. Therefore, the material constants are determined at a strain value of 0.6 for sintered Al–4wt.%B_4C composite during the hot upsetting.

The Eqs. (5.8) and (5.9) are obtained from the Eqs. (5.2) and (5.3) by applying natural logarithm, respectively.

$$\ln \acute{\varepsilon} = \ln A_1 + n \ln \sigma - \frac{Q}{RT} \tag{5.8}$$

$$\ln \acute{\varepsilon} = \ln A_2 + \beta\sigma - \frac{Q}{RT} \tag{5.9}$$

The hot deformation process was done at a constant temperature and partial differentiation of Eqs. (5.8) and (5.9) can be simplified as:

$$n = \left[\frac{\partial ln\acute{\varepsilon}}{\partial ln\sigma}\right]_{T=const} \tag{5.10}$$

$$\beta = \left[\frac{\partial ln\,\acute{\varepsilon}}{\partial \sigma}\right]_{T=const} \tag{5.11}$$

The plots of lnέ–lnσ and lnέ–σ are obtained by inserting the values of flow stress and corresponding strain rate for various temperatures and IRDes into Eqs. (5.10) and (5.11) as shown in Figs. 5.10 – 5.15, respectively. And n and β values can be obtained by using the average slope values of the lines lnέ–lnσ and lnέ–σ plots for various temperatures, respectively. Therefore, α = β/n value is calculated. The values of n, β and α are shown in Table 5.1 for sintered Al–4wt.%B_4C composite during hot upsetting with different IRDes.

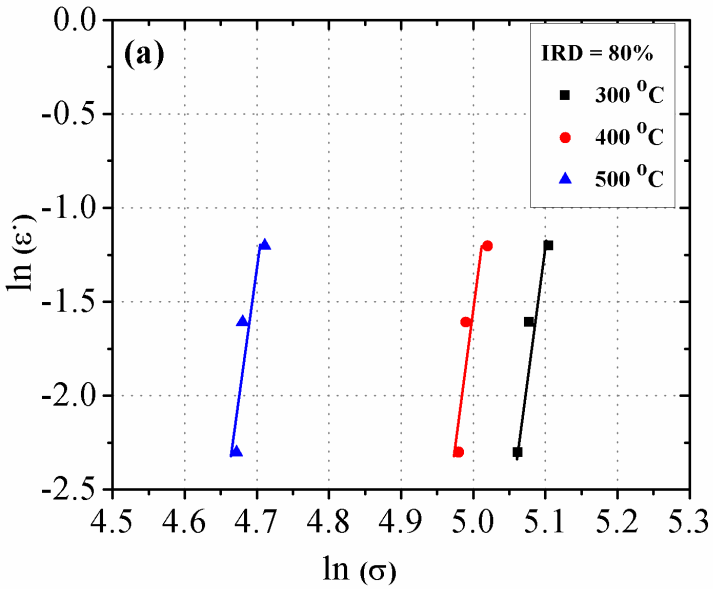

Fig. 5.10 Relationship between lnέ– lnσ of Al–4wt.%B_4C composite with IRD: (a) 80%.

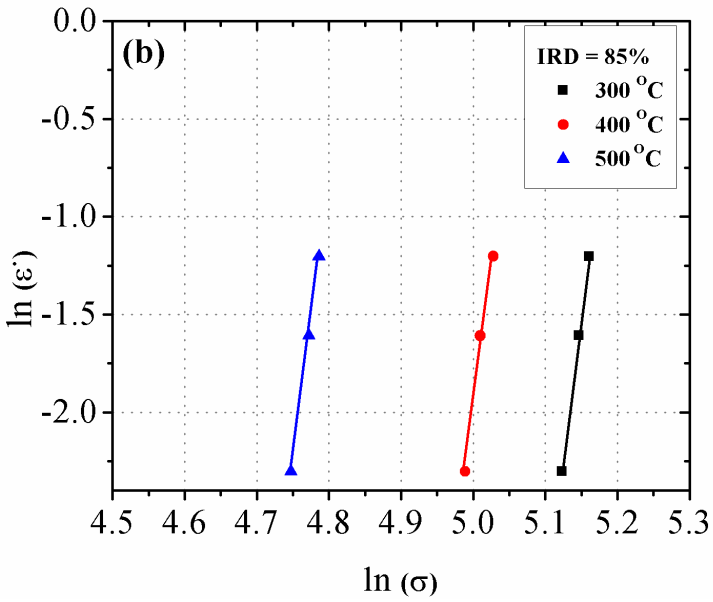

Fig. 5.11 Relationship between lnέ– lnσ of Al–4wt.%B_4C composite with IRD: (b) 85%.

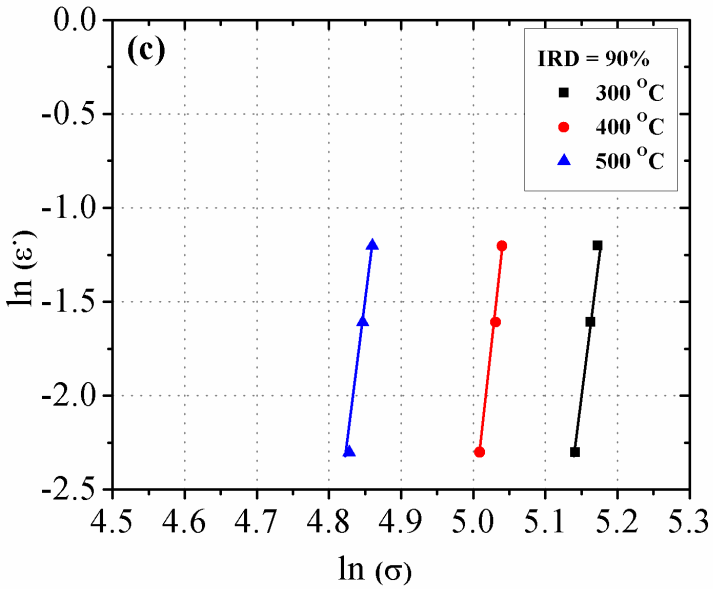

Fig. 5.12 Relationship between lnέ– lnσ of Al–4wt.%B_4C composite with IRD: (b) 90%.

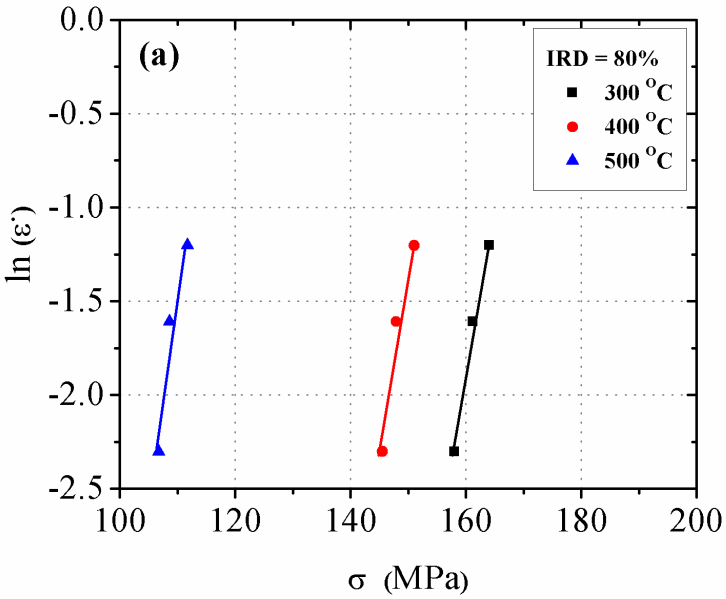

Fig. 5.13 Relationship between lnέ–σ of Al–4wt.%B_4C composite with IRD: (a) 80%.

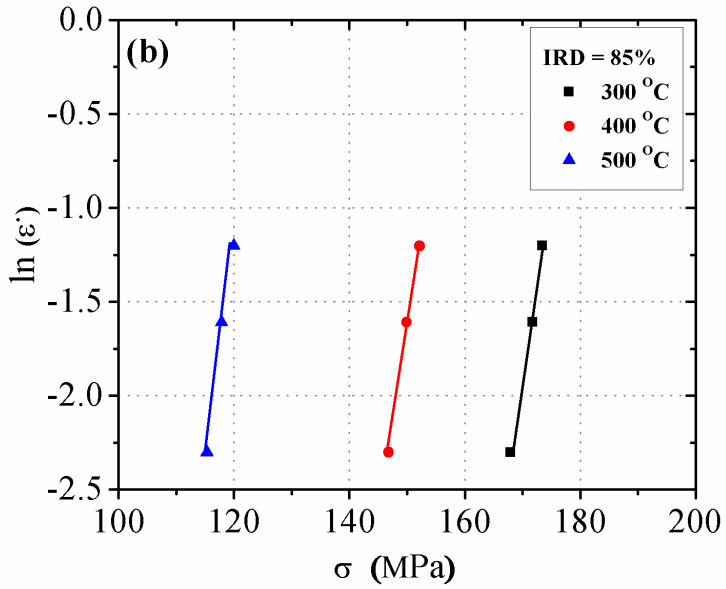

Fig. 5.14 Relationship between lnέ–σ of Al–4wt.%B_4C composite with IRD: (b) 85% .

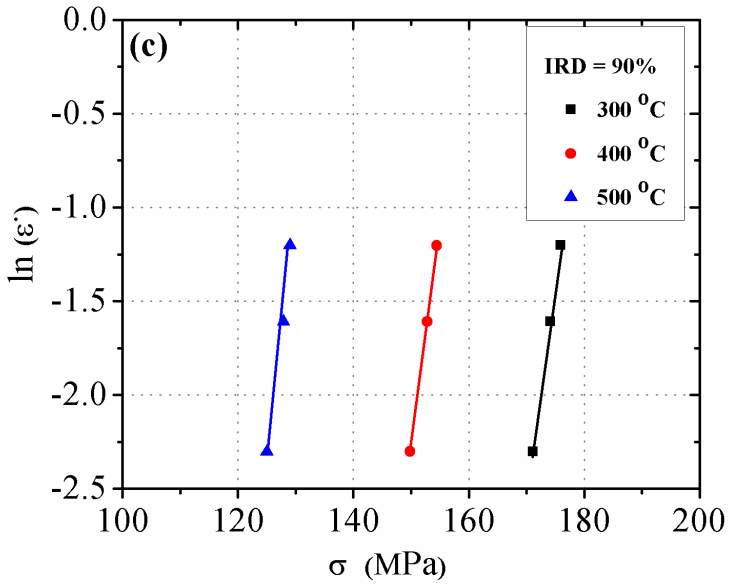

Fig. 5.15 Relationship between lnέ–σ of Al–4wt.%B_4C composite with IRD: (c) 90%.

Likewise, the activation energy (Q) of sintered Al–4wt.%B_4C composite during hot upsetting with different IRDes can be obtained by applying the natural logarithm on both sides of Eq. (5.4):

$$\ln \acute{\varepsilon} = \ln A + n \ln[\sinh(\alpha\sigma)] - \frac{Q}{RT} \tag{5.12}$$

For the given constant strain rate condition, partial differentiation of Eq. (5.12) gives:

$$Q = R \left\{\frac{\partial \ln \acute{\varepsilon}}{\partial \ln[\sinh(\alpha\sigma)]}\right\}_{T=const} \left\{\frac{\partial \ln[\sinh(\alpha\sigma)]}{\partial\left(\frac{1}{T}\right)}\right\}_{\acute{\varepsilon}=const} \tag{5.13}$$

Table 5.1 Values of β, n, α and Q with different IRDes of Al–4%B_4C composite.

IRD (%)	β	n	A	Q (KJ/mol)
80	0.197	24.23	0.0081	161.06
85	0.212	28.44	0.0074	172.28
90	0.243	34.76	0.007	181.05

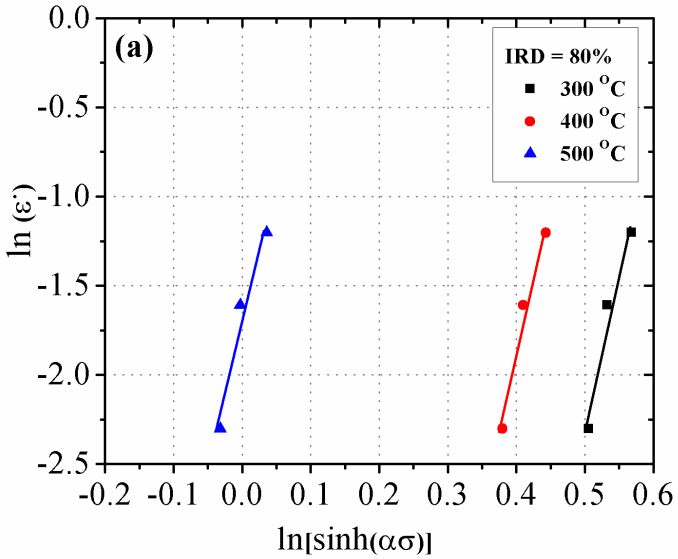

Fig. 5.16 Relationship between lnέ–ln[sinh(ασ)] of Al–4wt.%B_4C composite with IRD: (a) 80%.

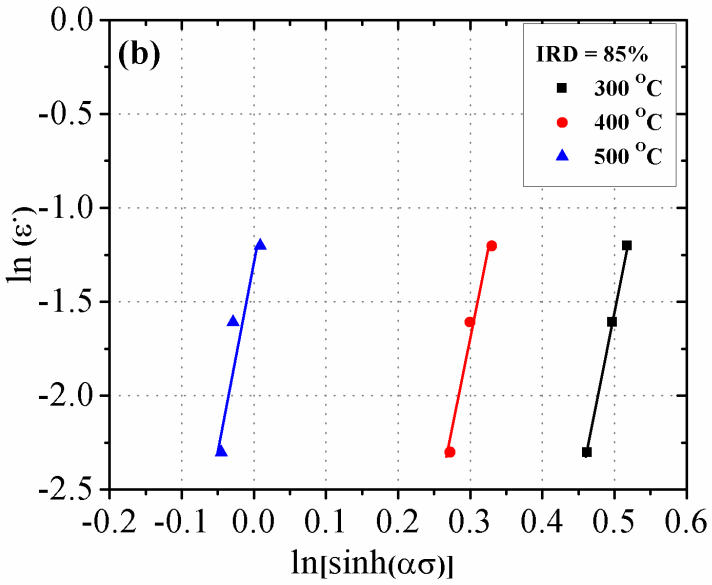

Fig. 5.17 Relationship between lnε̇–ln[sinh(ασ)] of Al–4wt.%B_4C composite with IRD: (b) 85%.

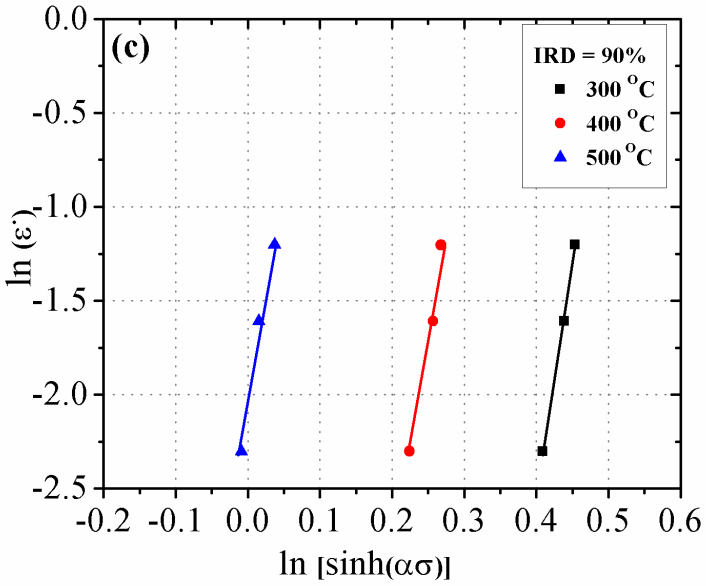

Fig. 5.18 Relationship between lnε̇–ln[sinh(ασ)] of Al–4wt.%B_4C composite with IRD: (c) 90%.

Therefore, the relationship of lnε̇–ln[sinh(ασ)] and ln[sinh(ασ)]–1/T will be obtained by inserting the values of σ, α and temperature and corresponding strain rate for different

IRDes into Eq. (5.13), respectively. The Q values mentioned in Table 5.1 for different IRDes which is calculated from the slope of lines lné–ln[sinh(ασ)] and ln[sinh(ασ)]–1/T plots are demonstrated in Figs. 5.16 – 21, respectively. It is clearly noticed that the value of n, β, and Q are greatly affected by the IRD. It is also noticed that the Q values required for hot deformation decreases with decrease in IRD because of the presence of more pores in the preforms, which reduce the resistance of the material to deform. The activation energy is one of the key parameters which measure the degree of difficulty of the hot deformation of the materials. As a result, plastic deformations become more difficult with increasing IRD. In another way, the values of α decrease with an increase in the IRD of sintered Al–4wt.%B_4C composite during the hot upsetting.

By applying the natural logarithm of Eq. (5.6), it gives:

$$\ln Z = \ln A + n \ln[\sinh(\alpha\sigma)] \tag{5.14}$$

By inserting the values of Q into Eq. (5.5) for corresponding strain rate at various deformation temperatures, the Z parameter can be evaluated. The values of lnA determined from the intercept of lines lnZ–ln[sinh(ασ)] plots for different IRDes are demonstrated in Fig. 5.22 – 5.24. The values of lnA for sintered Al–4wt.%B_4C composite with different IRDes of 80%, 85% and 90% can be found to be 21.27, 24.16 and 25.55, respectively.

Figs. 5.22 – 5.24 show that the slope values of lnZ–ln[sinh(ασ)] plots are decreasing with decrease in IRDes. When the slope of the plot lnZ–ln[sinh(ασ)] is low, the deformation conditions slightly affected on the PFS of the preforms, but it is significant for higher slope irrespective of the IRDes.

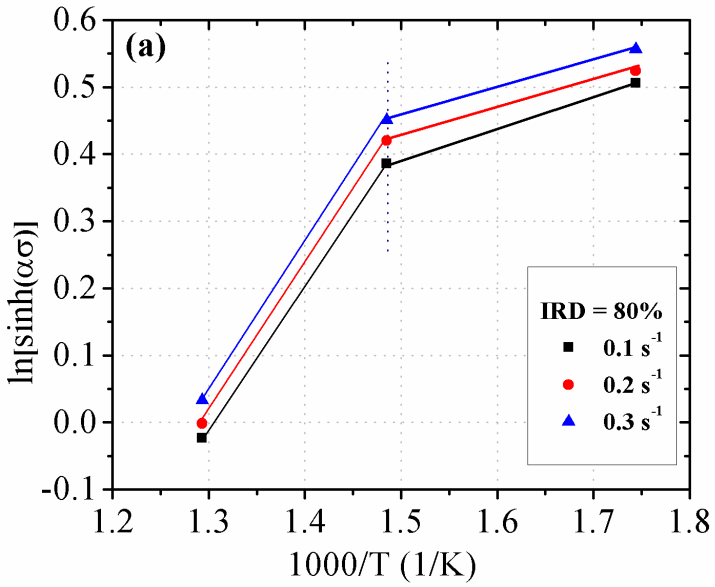

Fig. 5.19 Relationship between ln[sinh (ασ)]–1/T of Al–4wt%B_4C composite with IRD: (a) 80%.

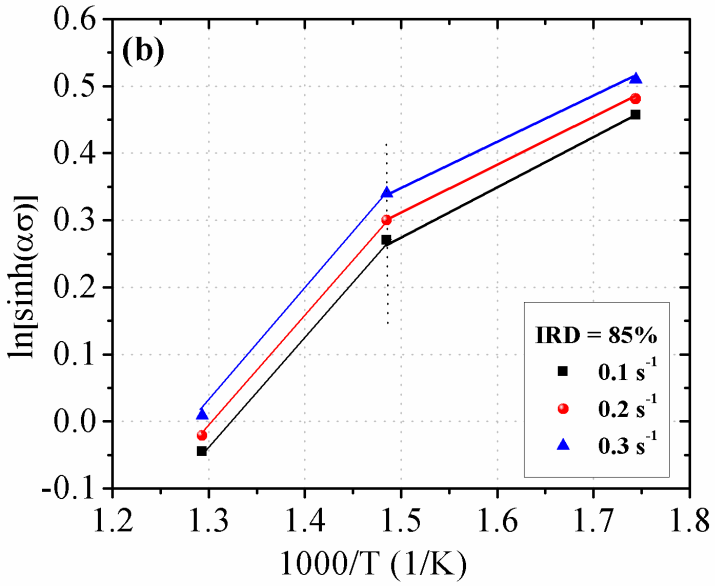

Fig. 5.20 Relationship between ln[sinh (ασ)]–1/T of Al–4wt.%B_4C composite with IRD: (b) 85%.

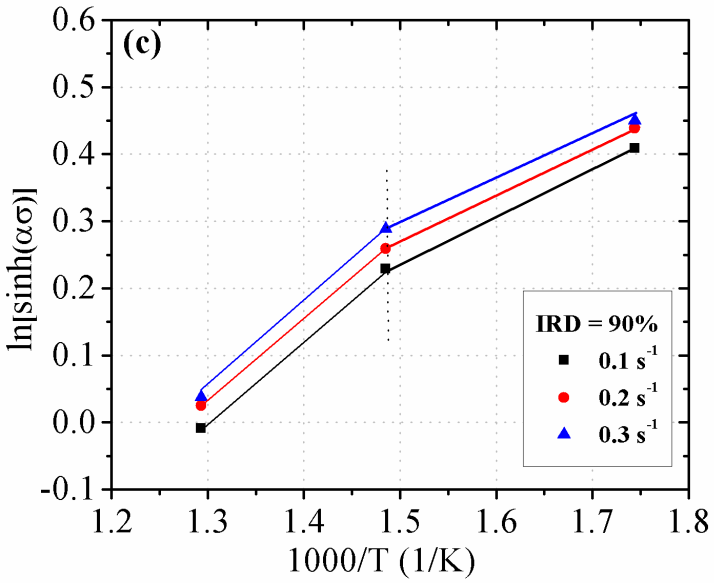

Fig. 5.21 Relationship between ln[sinh (ασ)]–1/T of Al–4wt.%B_4C composite with IRD: (c) 90%.

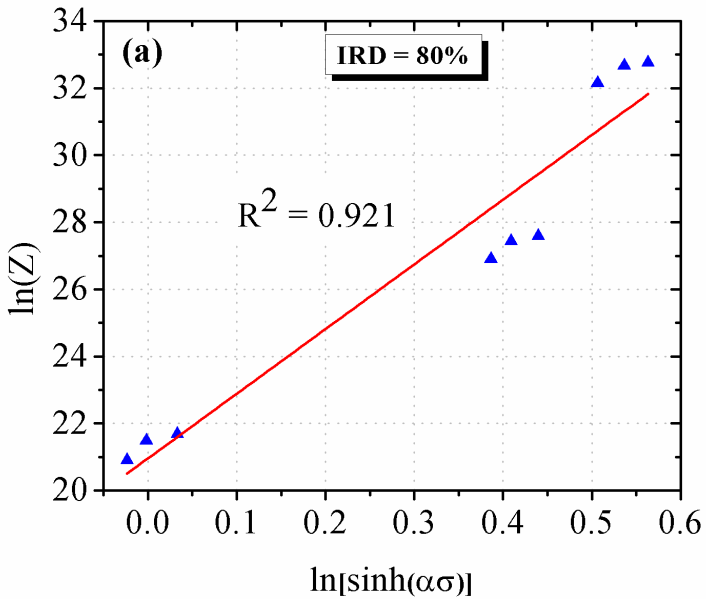

Fig. 5.22 Relationship between lnZ–ln[sinh(ασ)] of Al–4wt.%B_4C composite with IRD: (a) 80% .

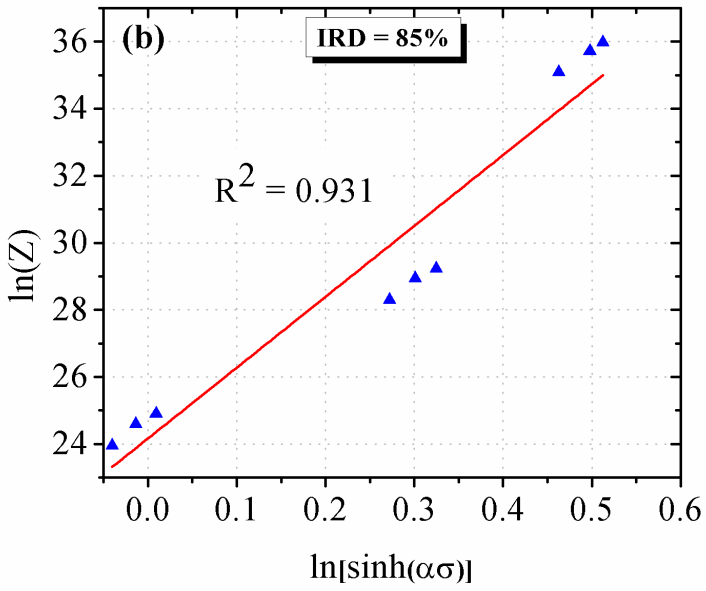

Fig. 5.23 Relationship between lnZ–ln[sinh(ασ)] of Al–4wt.%B_4C composite with IRD: (b) 85%.

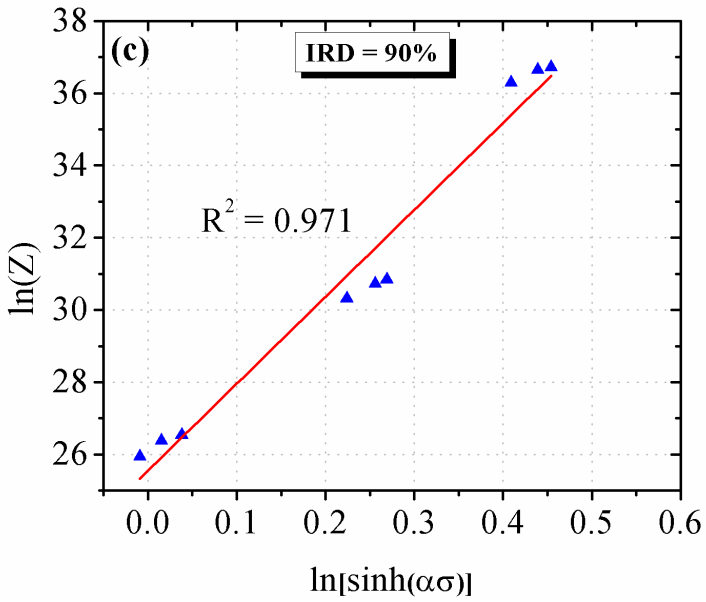

Fig. 5.24 Relationship between lnZ–ln[sinh(ασ)] of Al–4wt.%B_4C composite with IRD: (c) 90%.

The relationship between n, α, lnA and Q and IRD of sintered Al–4wt.%B_4C composite were established by fitting data point into a polynomial function as shown in Fig. 5.25 – 5.28. Thus, the developed mathematical expression between IRD and flow stress, deformation temperature, strain rate of sintered Al–4wt.%B_4C composite during hot upsetting tests can be expressed as follows.

$$n = 0.0422\ IRD^2 - 6.121\ IRD + 243.8 \quad (5.15)$$

$$\alpha = 6E-06\ IRD^2 - 0.00113\ IRD + 0.0601 \quad (5.16)$$

$$Q = -0.049\ IRD^2 + 10.329\ IRD - 351.66 \quad (5.17)$$

$$\ln A = -0.03\ IRD^2 + 5.528\ IRD - 228.97 \quad (5.18)$$

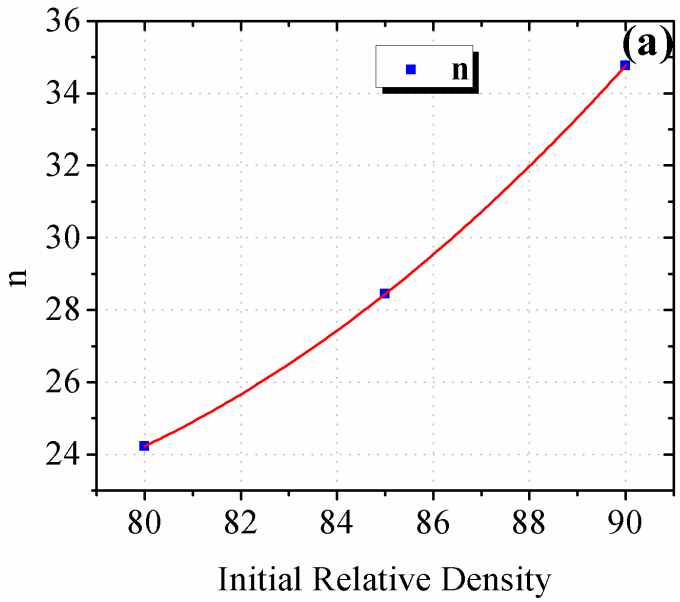

Fig. 5.25 Variation in (a) n with initial relative density in sintered Al–4wt.%B_4C composite during hot upsetting test.

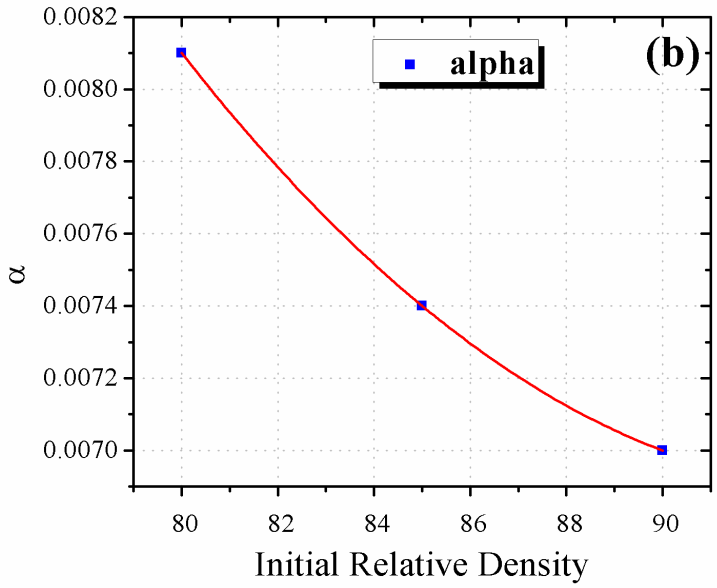

Fig. 5.26 Variation in (b) alpha (α) with initial relative density in sintered Al–4wt.%B_4C composite during hot upsetting test.

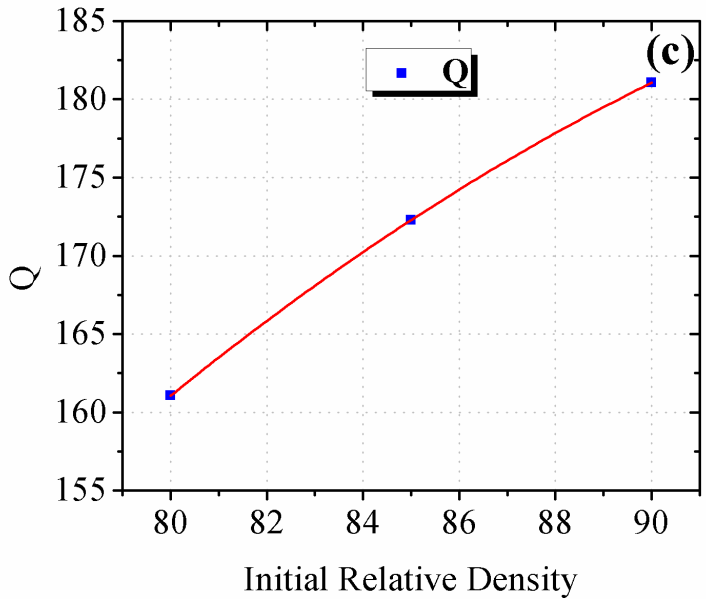

Fig. 5.27 Variation in (c) Q with initial relative density in sintered Al–4wt.%B_4C composite during hot upsetting test.

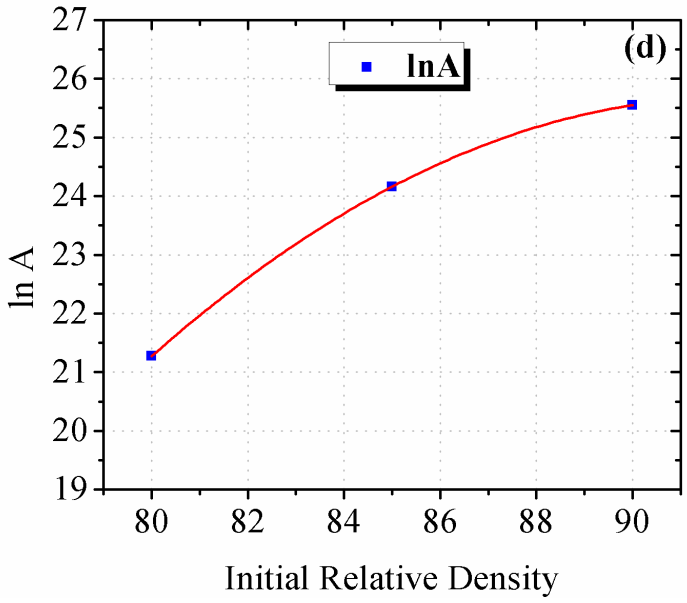

Fig. 5.28 Variation in (d) lnA with initial relative density in sintered Al–4wt.%B_4C composite during hot upsetting test.

5.3.2 Validation of developed constitute equations of Al–4wt.%B_4C composite

The predicted flow stress values determined according to Eqs. (5.7) and (5.15) – (5.18) is tabulated in Table 5.2. The values of predicted flow stress (σ_P) are compared with experimental flow stress (σ_E) values by plotting the graphs to assess the accuracy of the developed constitutive equation of sintered Al–4wt.%B_4C composite for different IRDes, and are shown in Figs. 5.29 to 30. All the experimental and predicted data are close to the best fit line which indicates the accuracy of the constitutive equation. The R^2 values are found to be 0.923, 0.977 and 0.994 for IRDes of 80%, 85% and 90%, respectively. It is noticed that the prediction capability of developed a constitutive model is better for higher IRD.

Moreover, the established constitutive models for sintered Al–4wt.%B_4C composite accuracy was confirmed by applying standard statistical parameter such as absolute error (δ) and mean absolute error (δ_m). The absolute error is calculated from predicted and experimental values by using Eq. (5.19).

$$\delta = \left|\frac{\sigma_P - \sigma_E}{\sigma_E}\right| X\ 100\ \% \quad (5.19)$$

The detailed comparisons were made between the predicted and experimental results of sintered Al–4wt.%B_4C composite for various temperatures and strain rates with different IRDes as shown in Table 5.2. The average percentage error for IRDes of 80%, 85%, and 90% was 7.61, 6.33, and 4.44, respectively and for deformation temperatures of 300 ^oC, 400 ^oC and 500 ^oC was 3.03, 6.64 and 8.76, respectively. It is observed that the developed constitutive equation has a better predictive capability for lower deformation temperature and higher IRD during hot upsetting. The maximum mean absolute error is not exceeding 9.95% and it is acceptable considering the complexity of the deformation behavior of porous materials.

It is suggested that the established constitutive model has the good predictive capability of Al–4wt.%B_4C composite during hot upsetting for lower temperature and higher IRD. Accordingly, the predicted results are well satisfied with the experimental result, which verifies the accuracy of the developed constitutive model for sintered Al–4wt.%B_4C composite during the hot upsetting test.

Table 5.2 Comparison between experimental and predicted peak flow stress of sintered Al–4wt.%B_4C composite.

Def. Tem. (K)	έ (s^{-1})	IRD = 80%				IRD = 85%				IRD = 90%				Avg.
		σ_E MPa	σ_P MPa	δ (%)	δ_m (%)	σ_E MPa	σ_P MPa	δ (%)	δ_m (%)	σ_E MPa	σ_P MPa	δ (%)	δ_m (%)	
573	0.1	158.02	169.41	7.21	6.4	167.97	172.26	2.55	1.67	171.13	174.00	1.68	1.02	3.03
573	0.2	160.90	171.64	6.71		171.98	174.89	1.69		173.16	175.28	1.22		
573	0.3	164.32	173.11	5.35		174.68	176.02	0.77		175.24	175.22	0.16		
673	0.1	145.54	134.26	7.75	8.1	146.81	136.49	7.03	7.54	150.26	144.37	3.92	4.27	6.64
673	0.2	147.67	136.42	7.67		149.93	138.86	7.39		151.61	145.68	3.91		
673	0.3	151.15	137.68	8.91		152.68	139.95	8.22		153.76	146.00	5.01		
773	0.1	106.78	98.38	7.87	8.31	115.28	104.37	9.46	9.95	124.87	115.48	7.52	8.02	8.76
773	0.2	108.65	100.19	7.78		117.21	106.31	9.30		127.10	116.68	8.20		
773	0.3	111.71	101.34	9.28		119.97	107.24	10.6		127.81	117.11	8.37		
Average					7.61				6.33				4.44	

Further, the ability of the developed constitutive equation for predicting the peak flow stress of sintered Al–4wt.%B_4C composite was evaluated by calculating the peak flow stress with IRD of 88%. The predicted flow stress of sintered Al–4wt.%B_4C composite of 88% initial relative density for various temperatures and strain rates are compared with experimental peak flow stress of the same condition and are shown in Table 5.3. The experimental peak flow stress values of sintered Al–4wt.%B_4C composite of 88% IRD was not used to develop the constitutive equation. It is clearly noticed from Table 5.3 that the average mean absolute error is 5.97, which indicate that the developed constitutive model is capable to predict accurately the peak flow stress of the preforms.

Table 5.3 Comparison between experimental and predicted peak flow stress of sintered Al–4wt.%B_4C composite of initial relative density 88%.

Def. Tem. (K)	**έ (s^{-1})**	**IRD = 88%**			
		σ_E MPa	**σ_P MPa**	**δ (%)**	**δ_m (%)**
573	0.1	169.25	156.61	7.46	7.97
573	0.2	173.17	159.07	8.13	
573	0.3	175.15	160.52	8.34	
673	0.1	148.41	137.59	7.28	7.49
673	0.2	151.17	139.90	7.45	
673	0.3	153.12	141.25	7.74	
773	0.1	122.08	124.37	1.88	2.47
773	0.2	123.26	126.55	2.67	
773	0.3	124.25	127.83	2.88	
Average					5.97

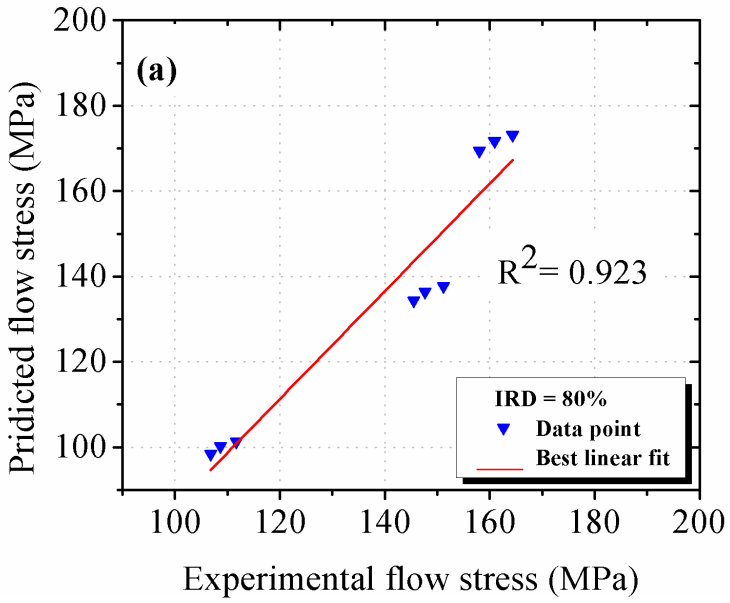

Fig. 5.29 Comparison between experimental and predicted flow stress of sintered Al–4wt.%B_4C composite with IRD: (a) 80%.

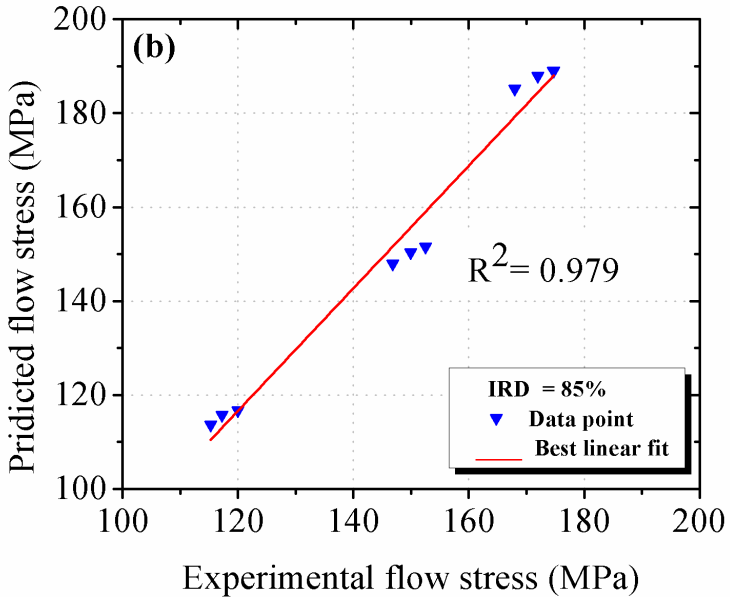

Fig. 5.30 Comparison between experimental and predicted flow stress of sintered Al–4wt.%B_4C composite with IRD: (b) 85%.

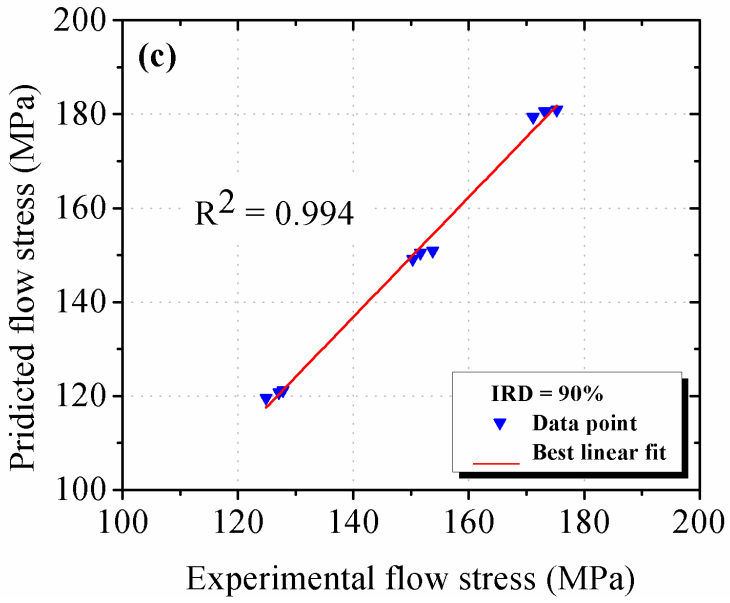

Fig. 5.31 Comparison between experimental and predicted flow stress of sintered Al–4wt.%B_4C composite with IRD: (c) 90%.

5.4 Activation energy of sintered Al–4wt.%B_4C composite

The average activation energy (Q) of sintered Al–4wt.%B_4C composite were calculated for various IRDes during the hot upsetting test, which is more than the value of self–diffusion of pure aluminum as shown in Table 5.4. It was reported [73,74] that the activation energy of aluminum metal matrix composite for hot deformation was higher than that of self–diffusion of aluminum. The dislocation motion is impeded by the existing B_4C particles in the composite. Gangolu et al. [54] reported that the average activation energy of Al–5wt.%B_4C composite prepared by casting route is more than the average activation energy of sintered Al–4wt.%B_4C preforms for investigated IRD as shown in Table 5.4. It was concluded that the obtained activation energy of sintered Al–4wt.%B_4C preforms for different IRDes are acceptable. The occurrence of higher activation energy during upsetting test of composite materials is due to the transformation of the deformation load to reinforcement by the matrix [73, 74]. Whereby an interfacial diffusion is considerably slower, which results in increase in the activation energy of composite materials.

Table 5.4 Activation energies (Q) (KJ/mol) for different composition

Composition	Fabrication Route	Activation energy (Q) (KJ/mol)			Reference
Al–4wt.%B_4C	Powder metallurgy	IRD			
		80%	85%	90%	
		161.08	172.28	181.05	
Al–5wt.%B_4C	Casting	200.1			[54]
Pure aluminum	Casting	144.3			[75]

5.5 Summary

The hot deformation behavior of sintered Al–4wt.%B_4C composite with various IRDes of 80%, 85% and 90% were studied by performing hot upsetting tests for various temperatures of 300 ^oC, 400 ^oC and 500 ^oC and strain rates of 0.1 s^{-1}, 0.2 s^{-1} and 0.3 s^{-1}. The flow stress behavior of sintered Al–4wt.%B_4C preforms with different IRDes for various temperatures and strain rate have been studied. A constitutive model was developed in terms of IRD of sintered Al–4wt.%B_4C composite to predict flow stress. Validation test was done between the predicted and experimental values. The activation energy of sintered Al–4%B_4C composites were calculated for different IRDes and compared with existing literatures.

CHAPTER 6

Analysis of Grain Size Evolution of Sintered Al–4wt.%B_4C Preforms Subjected to Hot Compression Test

6.1 Introduction

In the previous chapter the effect of deformation conditions on the flow behavior of sintered Al–4wt.%B_4C preforms subjected to hot compression test was discussed. It is observed that the changes in flow behavior of sintered Al–4wt.%B_4C preforms is significant for various deformation conditions. However, the grain size of the material also changes due to various deformation conditions namely deformation temperature, strain rate, deformation degree (strain) and initial relative density. Generally the grain size of material controls the mechanical properties of materials. Better mechanical properties such as strength and hardness are necessary to increase the lifetime of the final product. The grain size of the material can be controlled by controlling the evolution of microstructure of a material during hot deformation process. Limited researches have been done related to the microstructure evolution of powder preforms with deformation conditions.

Therefore, it is essential to understand the microstructure evolution of sintered Al–B_4C preforms during the hot deformation for controlling the grain size. Hence, this chapter discusses the evolution of microstructure of sintered Al–4wt.%B_4C composite for different deformation conditions such as temperature, strain rate, initial relative density and deformation degree during the hot compression test by metallurgical analysis. The

compression tests were performed on hydraulic press for different temperatures (300 ^{o}C, 400 ^{o}C and 500 ^{o}C), strain rates (0.1 s^{-1}, 0.2 s^{-1} and 0.3 s^{-1}), initial relative densities (80%, 85% and 90%) and deformation degree (reduction in preforms height of 10%, 20%, 30%, 40% and 50%).

6.2 Effect of temperature

Fig. 6.1 shows the optical microstructure of 90% initial relative density sintered Al–4wt.%B_4C preforms deformed under 0.1 s^{-1} strain rate for various temperatures. The DRXed grain size of Al–4wt%B_4C preform deformed under 0.1 s^{-1} strain rates were measured as 15.16 µm, 16.19 µm and 16.87 µm for different temperatures such as 300 ^{o}C, 400 ^{o}C and 500 ^{o}C, respectively.

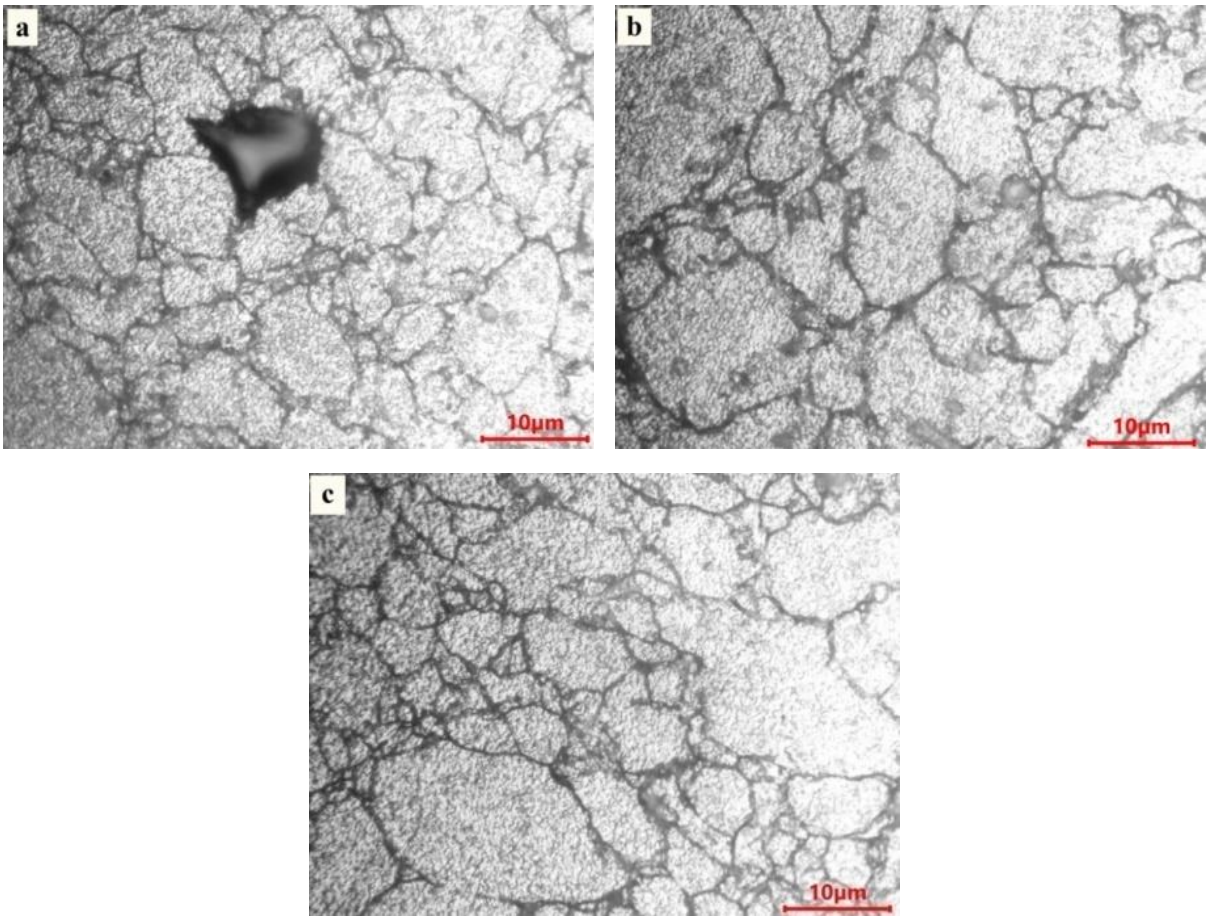

Fig. 6.1 Microstructures of 90% IRD Al–4wt.%B_4C preforms deformed for 0.1s^{-1} strain rate at different temperatures: (a) 300 ^{o}C (b) 400 ^{o}C and (c) 500 ^{o}C.

It is noticed from the microstructural analysis that the average DRX grain size of Al–4wt.%B_4C deformed preforms increases with increasing deformation temperature. During the hot deformation, the grain growth increase with increased deformation temperature due to which the diffusion rate between the grains is increased leading to increase in the grain size. In other words, the average DRX grain size of Al–4wt.%B_4C deformed preforms increases with increasing deformation temperature, because of higher mobility of DRX grain boundaries at the higher temperature [22,76]. Fig. 6.2 shows the relationship between deformation temperature and average grain size of 90% IRD for Al–4wt.%B_4C preforms deformed under 0.1 s^{-1} strain rate. It is observed that the average DRX grain size increases linearly with increasing deformation temperature. The same kind of behavior is observed for remaining initial relative densities of 80% and 85% with 0.2 s^{-1} and 0.3 s^{-1} strain rates.

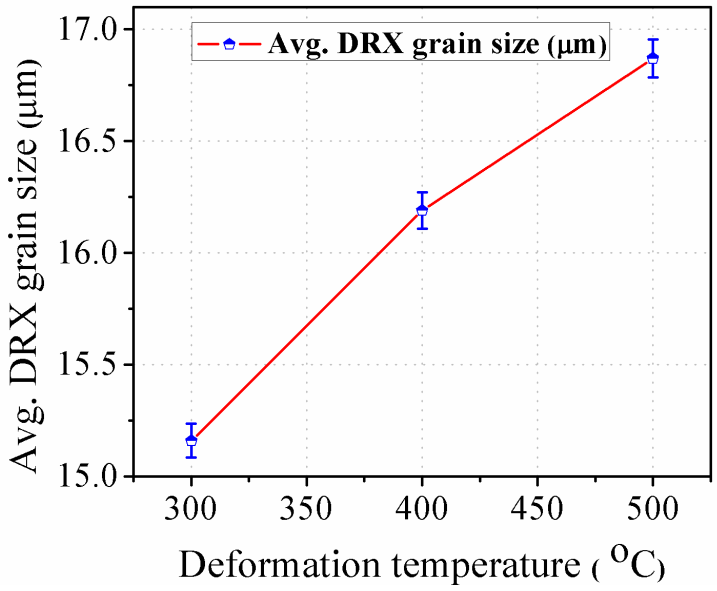

Fig. 6.2 Relationship between deformation temperature and average grain size of 90% IRD Al–4wt.%B_4C preforms deformed at 0.1 s^{-1} strain rate.

6.3 Effect of strain rate

Fig. 6.3 shows the optical microstructure of 90% IRD Al–4wt.%B_4C preforms deformed at 500 ^oC temperatures for various strain rates. The DRXed grain size of 90% IRD Al–4wt.%B_4C preforms deformed at 500 ^oC temperatures for different strain rate of 0.1 s^{-1}, 0.2 s^{-1} and 0.3 s^{-1} was 16.87 μm, 16.61 μm and 16.56 μm, respectively. As shown in Fig. 6.3

the average DRX grain size of Al–4wt.%B_4C deformed preforms decreases with increasing strain rate. With increase in the strain rate, the dynamic recovery rate is decreased whereas dislocation density is increased, resulting in more nucleation rates in the deformed structures [23, 77, 78]. The recrystallized grains have no enough time to grow at higher strain rates at constant deformation temperatures [23]. On the other hand, finer DRX grains are obtained at higher strain rate due to higher nucleation and lower growth. Thus, the grain size decreases with increase in strain rate of Al–4wt.%B_4C deformed preforms. Fig 6 represents the relationship between strain rate and average grain size of 90% IRD Al–4wt.%B_4C preforms deformed at 500 ^oC deformation temperature.

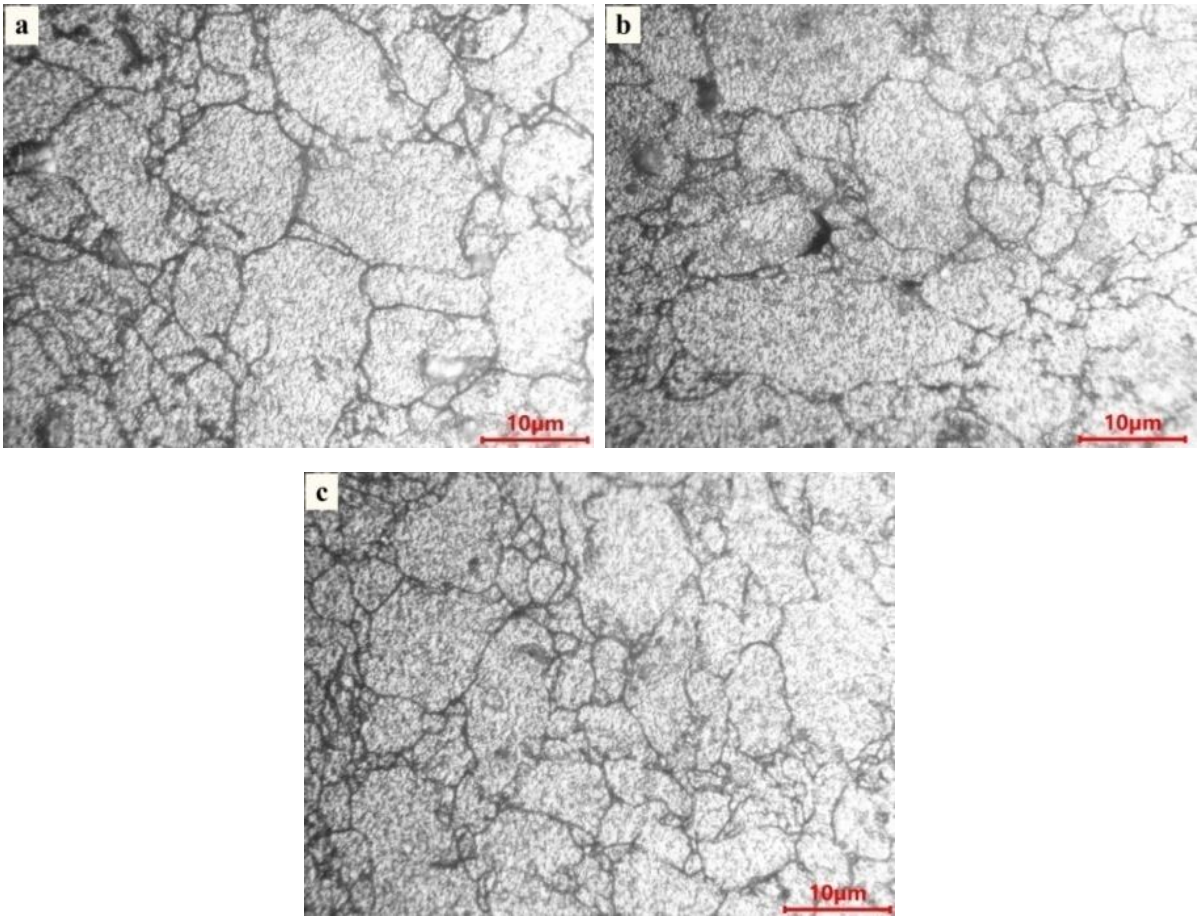

Fig. 6.3 Microstructures of 90% IRD Al–4wt.%B_4C preforms deformed at 500 ^oC temperature for different strain rates: (a) 0.1 s^{-1} (b) 0.2 s^{-1} and (c) 0.3 s^{-1}.

It is also noticed from Fig. 6.4, that the average grain size various with respect to strain rate at fixed temperature and initial relative density. From the strain rate 0.1 s^{-1} to 0.2 s^{-1}, the DRXed grain size is drastically changing because the nucleation rate is more in the

deformed structures at higher strain rates. On the other hand, the diffusion rate is less due to insufficient time at higher strain rates. The same sort of behavior is observed from the rest of temperatures and initial relative densities.

From the above results, it is observed that the DRX grain size of the sintered Al–4wt%B_4C deformed preforms is significantly sensitive to the deformation temperature and strain rate. Generally, Zener–Hollomon parameter (Z) [72] is used to study the combined effect of deformation temperature and strain rate on behavior of metals and alloys. The grain size of the sintered Al–4wt.%B_4C deformed preforms is also dependent on Z parameter that is a decreasing Z leads to more adequate proceedings of dynamic recrystallization.

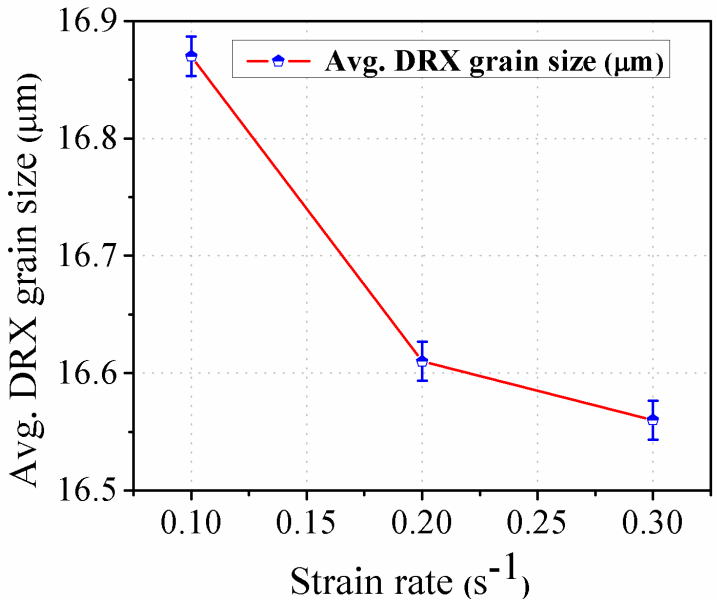

Fig. 6.4 Relationship between strain rate and average grain size of 90% IRD Al–4wt.%B_4C preforms deformed at 500 ^oC deformation temperature.

6.4 Effect of initial relative density

The effect of initial relative density on the average grain size of Al–4wt.%B_4Cpreforms deformed at different deformation conditions was studied. Fig. 6.5 shows the microstructure analysis of Al–4wt.%B_4C deformed preforms for various initial relative densities at a fixed temperature of 400^oC and strain rates of 0.2 s^{-1}. The average DRX grain size for different IRDes of 80%, 85% and 90% measured at 400 ^oC temperatures and 0.2 s^{-1}

strain rates were 8.17 µm, 9.41 µm and 15.17 µm, respectively. There is a significant role of initial relative density on average DRX grain size for all deformation conditions of Al–4wt.%B_4C composite during the hot compression test. From Fig. 6.5, it is observed that the average DRX grain size increases with increasing initial relative density. Porosity decreases with increasing initial relative density of preforms, which facilitate faster diffusion rates of the grains during hot deformation. Thus, the average DRX grain size increased at higher initial relative density. It is also observed in the grain size analysis with respect to initial relative density as shown in Fig. 6.6. It is noticed that the growth of DRXed grains is higher at 90% of IRD due to less amount of pores leading to increase in the diffusion rate between atoms. Similar behavior is observed for other deformation conditions of Al–4wt.%B_4C preforms during the hot compression test.

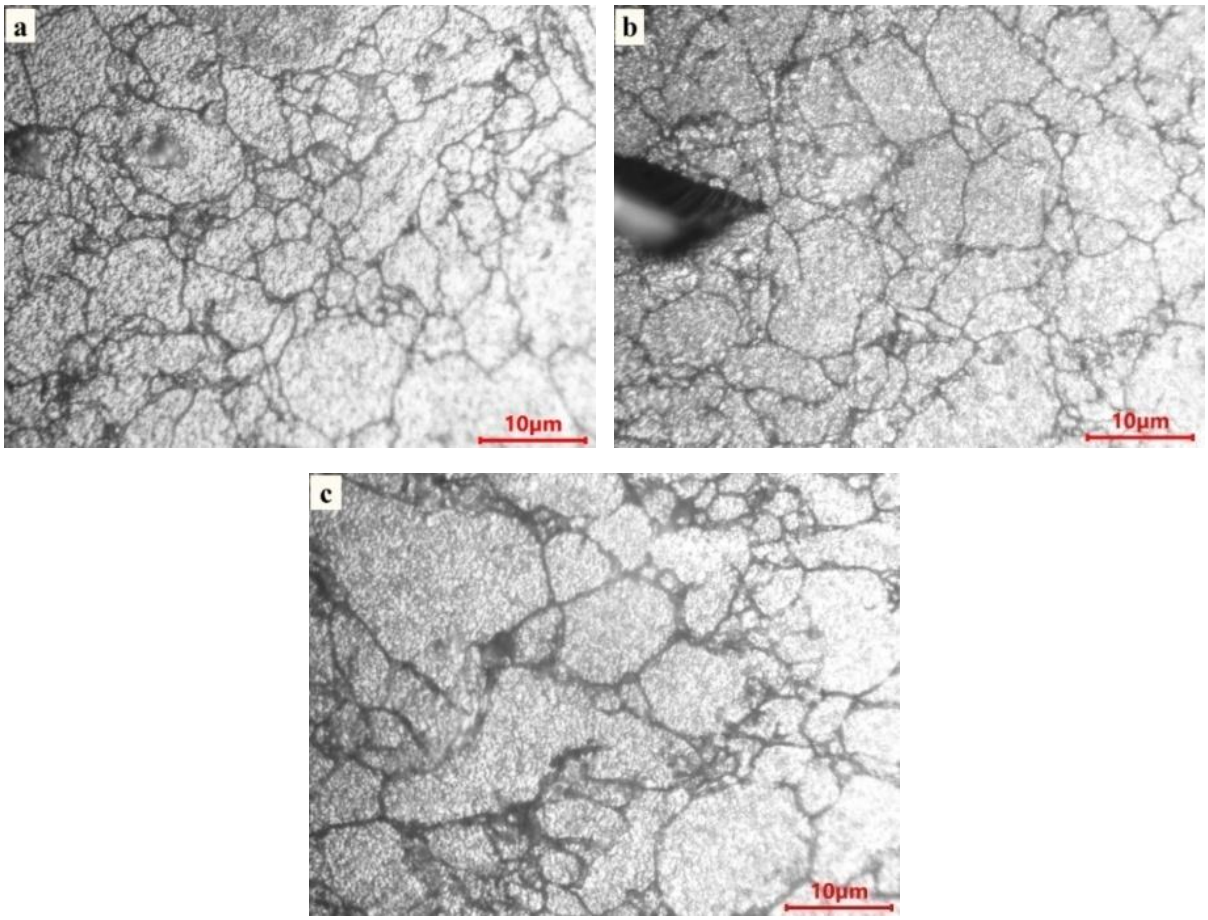

Fig. 6.5 Microstructures of Al–4wt.%B_4C preforms deformed with different IRDes (a) 80% (b) 85% (c) 95% for 400 ^oC temperature at 0.2 s^{-1} strain rate.

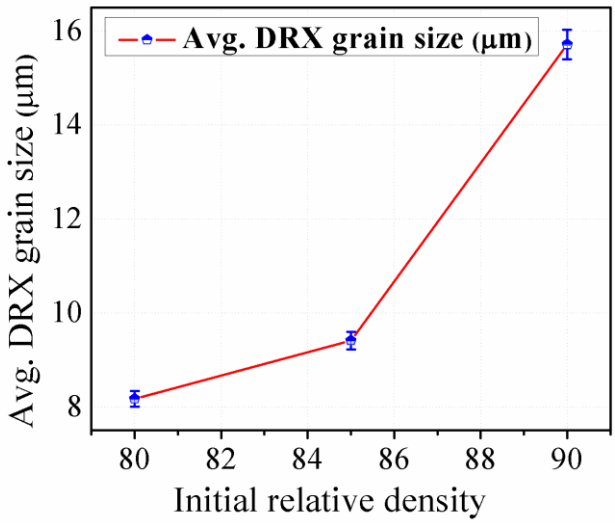

Fig. 6.6 Relationship between initial relative density and average grain size of Al–4wt.%B_4C preforms deformed for 400 ^oC temperature and 0.2 s^{-1} strain rate.

6.5 Effect of the deformation degree

The effect of deformation degree (reduction in preforms height) on the microstructure of sintered Al–4wt.%B_4C composite was studied. The microstructures of sintered Al–4wt.%B_4C composite with a deformation degree of 0 (undeformed preform), 10%, 20%, 30%, 40%, and 50% (fracture preform) are shown in Fig. 6.7 for 90% IRD at 500 ^oC deformation temperature and 0.1 s^{-1} strain rate. The effect of deformation degree on the average DRX grain size is more significant for all deformation conditions. It is noticed that the undeformed (prior to deformation) microstructure has an equiaxed grains structure with an average grain size of 25.43 µm. After the deformation degree of 10%, 20%, 30%, 40%, and 50% (fracture preform), the average grain sizes were measured as 21.23 µm, 18.22 µm, 17.22 µm, 16.17 µm and 14.72 µm, respectively.

It can be noticed from the results, that finer grains are obtained at higher deformation degree. With an increasing deformation degree, the dislocation density, dislocation generation rate and deformed stored energy have increased in the deformed structures, thereby the nucleation of recrystallized grains have occurred more easily [79]. For this reason, the recrystallized grain size is finer with increase in the deformation degree of the preforms and

the area of the grain boundary per unit volume is increased. It is a known fact that when the strain reaches the critical strain value, dynamic recrystallization will occur.

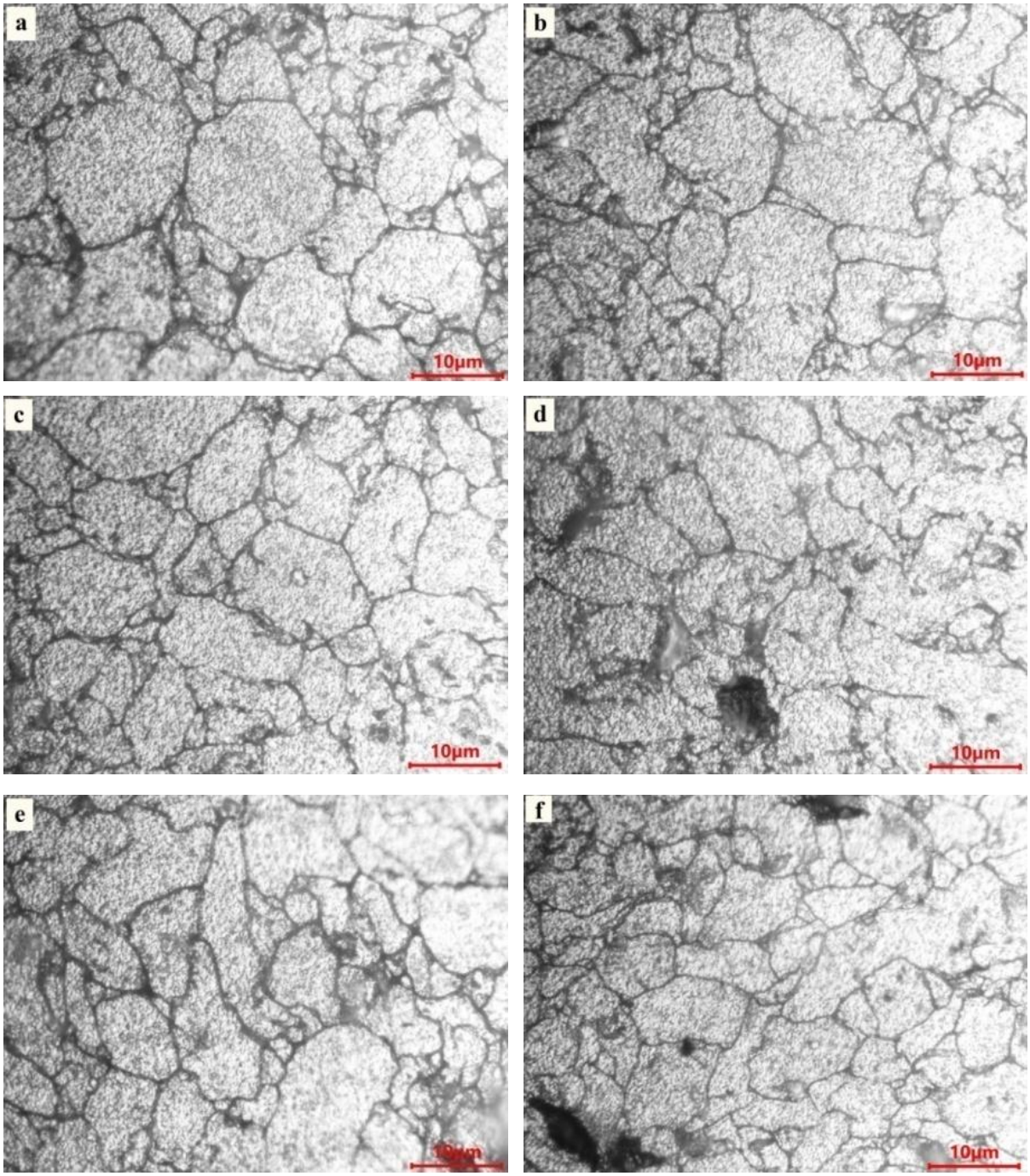

Fig. 6.7. Optical microstructures of 90% IRD sintered Al–4wt.%B_4C composite with a deformation degree of (a) 0 (undeformed preform) (b) 10% (c) 20% (d) 30% (e) 40% and (f) 50% (fracture preform) for 500 ^oC deformation temperature at 0.1 s^{-1} strain rate.

Fig. 6.8 shows the relationship between deformation degree and average DRXed grain size. It is noticed that at lower strain values the average grain size decreases rapidly than the higher strain values because during plastic deformation the dislocation density increase considerably in the lower strain values. The same sort of behavior is observed irrespective of the various initial relative densities, deformation temperatures and strain rates under all tested conditions.

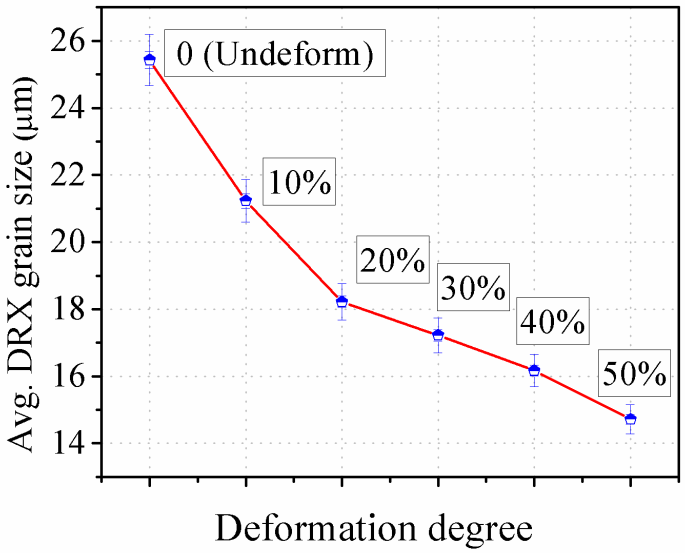

Fig. 6.8 Relationship between initial relative density and average grain size of Al–4wt.%B_4C preforms deformed for 500 ^oC deformation temperature and 0.1 s^{-1} strain rate.

6.6 Comparison between deformation conditions

Fig. 6.9 shows the relationship between deformation parameters and average DRX grain size. It is observed that the average DRX grain size increases with increase in the deformation temperature and initial relative density, and with decrease in the strain rate and deformation degree. The DRX grain size rapidly increased with increase in IRD and decrease in the deformation degree. Therefore, it is observed that the IRD and deformation degree are the more dominant parameters on the average DRX grain size of sintered Al–4wt%B_4C deformed preforms compared to deformation temperature and strain rate.

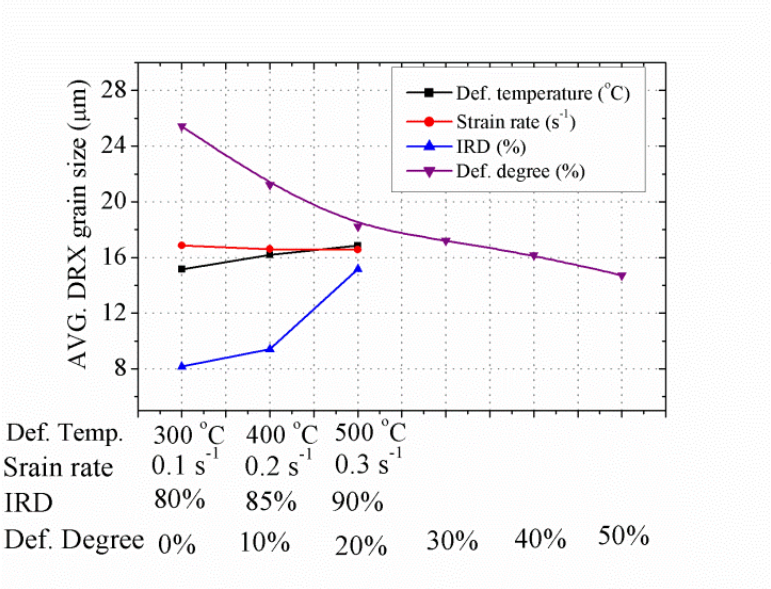

Fig. 6.9. Relationship between deformation parameters and average DRX grain size of Al–4wt%B_4C deformed preforms.

6.7 Summary

Hot upsetting test were performed on sintered Al–4wt%B_4C preforms to evaluated the grain sizes at different deformation conditions such as temperature (300 ^oC, 400 ^oC and 500 ^oC), strain rates (0.1 s^{-1}, 0.2 s^{-1} and 0.3 s^{-1}), initial relative density (80%, 85% and 90%) and deformation degree (reduction in preforms height such as 10%, 20%, 30%, 40% and 50%). The effect of deformation conditions on the average DRX grain size was characterized by an optical microscope. The effect of deformation conditions such as temperature, strain rate, initial relative density and deformation degree on the dynamic recrystallized grain size under steady-state conditions were examined during compression tests. The comparison was made between deformation conditions to know which parameter is more dominant on the dynamic recrystallized grain size.

CHAPTER 7

Microstructure Modeling of Dynamically Recrystallized Grain Size of Sintered Al–4wt.%B_4C Composite During Hot Upsetting

7.1 Introduction

The last chapter discussed the grain size control of any metal and alloy. It is an important technological feature in the forming process because it plays a vital role in the final product. Dynamic recrystallization is one of the key mechanisms for the grain size or microstructure control that reduces the material resistance force during the hot forming process [22, 23]. The deformation, microstructure and DRX grains behavior of the cast/wrought material (fully dense) are different from porous materials with the same chemical compositions because the geometry of the preforms, friction conditions and densification behavior is different [52]. Therefore, it is interesting to study the grain size evolution and the modeling aspects to predict the DRX grain size of powder preforms with different deformation parameters such as temperature strain rate and strain.

Hence, this chapter is to study the dynamic recrystallization (DRX) behavior and to develop a mathematical model to predict grain size of sintered Al–4wt.%B_4C composite during the hot upsetting test. Experimental works were performed on sintered Al–4wt.%B_4C preforms at various initial relative densities (IRD) values of 80%, 85% and 90%, and over the temperature range of 300 ^oC – 500 ^oC and strain rates range of 0.1 s^{-1} – 0.3 s^{-1}. The load–

displacement data were recorded during hot upsetting process. DRXed grain size of Al–4wt.%B_4C preforms for IRDes, temperatures and strain rates were evaluated.

7.2 Analysis of hot flow curves

The true stress (σ) – true strain (ε) curves of sintered Al–4wt.%B_4C preforms deformed at a temperature range of 300 ^oC – 500 ^oC with strain rates of 0.1 s^{-1} – 0.3 s^{-1} for various IRDes of 80%, 85% and 90%, are shown in Fig 7.1 to 7.3. It is noticed that the flow stress is significantly sensitive to the deformation conditions such as deformation temperatures and strain rates under the tested conditions [81 – 84]. The flow stress decreases with increasing deformation temperature and with decreasing strain rate irrespective of IRD. With increasing deformation temperature, the mobility of grain boundaries increases, thereby accelerating the growth of DRX grains [85]. In contrast, the vacancy diffusion and motion of dislocation rate increases with increasing deformation temperature [86]. Whereas, decreasing the strain rate provides sufficient time to deform the preforms leading to the growth of DRX grains. Thus, the dynamic softening is increased and facilitates the decrease in the flow stress [87]. It is also noticed that the effect of IRD on flow stress is significant for all tested conditions.

From Fig. 7.1 to 7.3 it is observed that the flow stress increases with increase in IRD irrespective of temperature and strain rate. The decrease in dislocation movement with increasing IRD leads to increase in the deformation difficulties of the preforms, as higher amount of load is required to deform the preforms. With increasing IRD, the strength and hardness of the preforms increases leading to increase in the deformation difficulties. The dislocation movement in response to deformation load is low for higher IRD when compared to lower IRD. Therefore, higher amount of load is required to overcome the deformation difficulties and to increase the dislocation movement in the preforms. The flow stress curves increase rapidly up to 0.2 strain value and then keep constant until the higher strain values. This happens because of dynamic balance between work hardening and dynamic softening. At lower strain, the work–hardening plays a dominant role, which is caused by the increase in dislocation density [78], leading to a rapid increase in the flow stress up to 0.2 strain values. After this, the flow stress curves follow a steady state stage at higher strain values, representing the DRX phenomenon during hot deformation. DRX phenomenon is followed by the dynamic recovery (DRV), which indicates that the work hardening can be neutralized or

partially neutralized with increasing strain. As a result, the σ–ε curves become flat with a nearly zero slope at higher strain values.

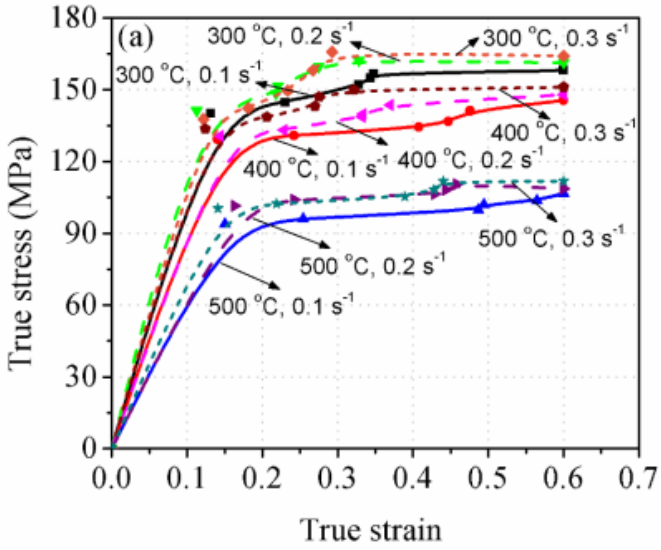

Fig. 7.1 True stress–true strain curves of Al–4wt. %B_4C composite for various deformation conditions and IRD of: (a) 80%.

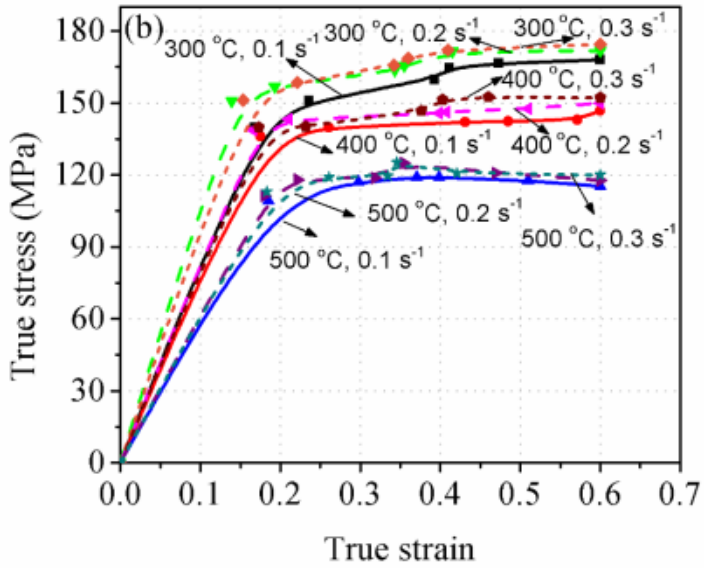

Fig. 7.2 True stress–true strain curves of Al–4wt. %B_4C composite for various deformation conditions and IRD of: (b) 85%.

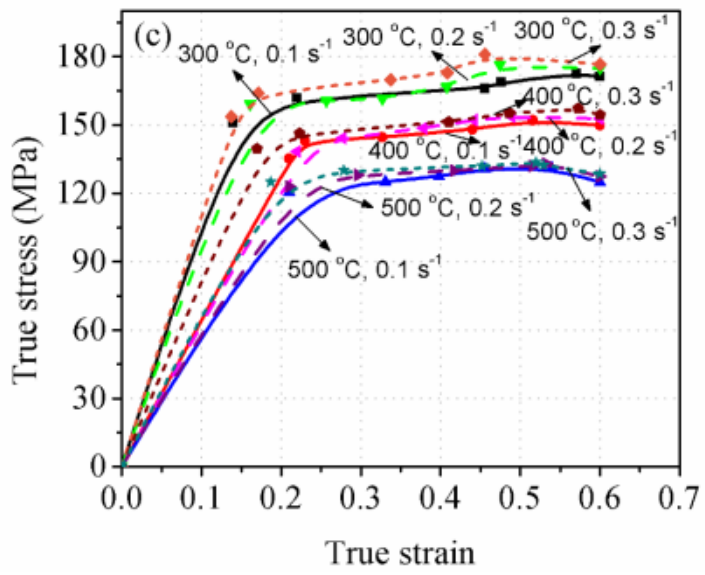

Fig. 7.3 True stress–true strain curves of Al–4wt. %B_4C composite for various deformation conditions and IRD of: (c) 90%.

7.3 Calculation of activation energy (Q) and Zener–Hollomon parameter (Z)

The DRX grain size depends only on the deformation conditions as reported elsewhere [23]. Accordingly, the combined effect of temperature and strain rate can be described as a function of Zener–Hollomon parameter [72]:

$$Z = \acute{\varepsilon} \exp\left(Q/_{RT}\right) \tag{7.1}$$

Where $\acute{\varepsilon}$ = strain rate (s^{-1}); Q = activation energy (KJ mol^{-1}) of hot deformation; R = universal gas constant (8.314 J mol^{-1} K^{-1}); T = absolute temperature (K).

First, it is better to calculate the hot deformation activation energy for finding Zener–Holloman parameters. Generally, Arrhenius [71, 72] type of constitutive equation is most commonly used to calculate activation energy during hot deformation. This equation could be expressed as follows:

$$\acute{\varepsilon} = A\,[\sinh(\alpha\sigma)]^n exp\left(-Q/_{RT}\right) \tag{7.2}$$

For low stress levels ($\alpha\sigma < 0.8$), $\sinh(\alpha\sigma)^n \cong \alpha\sigma$, whereas for high stress levels ($\alpha\sigma > 1.2$), $\sinh(\alpha\sigma) \cong 0.5\exp(\alpha\sigma)$ and hyperbolic sine law stress function can be used for any ($\alpha\sigma$) values.

The activation energy and Zener–Hollomon parameter calculation procedure were explained clearly in chapter 5. The Zener–Hollomon parameter values of Al–4wt.%B_4C composite for various deformation conditions are represented in Table 7.1.

Table 7.1 Values of activation energy (Q) and Zener–Holloman parameter with different IRDes of Al–4wt.%B_4C composite.

Def. Tem. (K)	**ε̇ (s^{-1})**	**IRD = 80%**		**IRD = 85%**		**IRD = 90%**	
		Q (KJ/mol)	Z (s^{-1})	Q (KJ/mol)	Z (s^{-1})	Q (KJ/mol)	Z (s^{-1})
573	0.1	167.72	1.9E+14	178.14	1.7E+15	183.92	5.8E+15
673	0.1	166.79	8.8E+11	171.25	1.9E+12	182.55	1.5E+13
773	0.1	151.11	1.6E+09	168.71	2.5E+10	181.49	1.8E+11
573	0.2	166.67	3.1E+14	177.81	3.2E+15	182.31	8.3E+15
673	0.2	165.74	3.7E+12	170.93	3.7E+12	180.95	2.2E+13
773	0.2	150.17	2.8E+09	168.40	4.8E+10	179.90	2.9E+11
573	0.3	166.22	4.2E+14	177.16	4.2E+15	180.69	8.8E+15
673	0.3	165.30	2.0E+12	170.31	4.9E+12	179.35	2.5E+13
773	0.3	149.77	3.9E+09	167.78	6.5E+10	178.31	3.3E+11

7.2.3 Development of microstructure model of Al–4wt.%B_4C composite

The correlation between average DRX grain size and Zener–Hollomon parameter (Z) can be expressed as follows [88]:

$$d_{dyn} = A_{dyn}\, Z^{n_{dyn}} \tag{7.3}$$

Where d_{dyn}–the dynamically recrystallized grain size, A_{dyn}, n_{dyn}–material constants.

The above equation was used to develop a mathematical model, which is useful for predicting the DRXed grain size. The correlation between Zener–Hollomon parameters and average DRX grain size of sintered Al–4wt.%B_4C composite were established by fitting power law in the form of an Eq. (7.3) for different initial relative densities as shown in Fig. 7.4 – 7.6. Thus, the mathematical models were developed between Zener–Hollomon parameters and average DRX grain size for different IRDes namely 80%, 85% and 90%. It can be expressed as follows.

For 80% IRD $d_{dyn} = 11.34Z^{-0.0121}$ $(R^2 = 0.908)$ (7.4)

For 85% IRD $d_{dyn} = 13.30Z^{-0.012}$ $(R^2 = 0.924)$ (7.5)

For 90% IRD $d_{dyn} = 22.56Z^{-0.011}$ $(R^2 = 0.931)$ (7.6)

Figures 7.4 – 7.6 describe the average DRX grain size as a function of the values of Zener–Hollomon parameter. It is noticed from the above developed mathematical model, the DRXed grain size is inversely proportional to the Z parameter. The average DRXed grain sizes decreases with decrease in the deformation temperature and increase in the strain rate, and are shown in Figs. 7.7 – 7.9. The mobility of DRX grain boundaries is slow at low temperature. At the same time, the nucleation rate increases with increasing strain rate, thus decreasing the average DRXed grain size. On the other hand, the average DRXed grain size increases with increasing in deformation temperature and with decreasing in strain rate. With increasing deformation temperature, the mobility of DRX grain boundaries increases, and at lower strain rates, due to the availability of sufficient time for grain growth the grain size increases. According to the Eq. (7.1), Z parameter increases with decreasing in deformation temperature and increasing in strain rate. Hence the grain size decreases with increasing Z parameter as shown in Fig. 7.4 – 7.6. On the other hand, the Z parameter decreases with increase in deformation temperature and with decrease in strain rate according to the Eq. (7.1). As a result grain size increases with decreasing Z parameter. Therefore, it is observed that the DRXed grain size is completely dependent on the temperature and strain rate (Z parameters) as shown in Figs. 7.7 – 7.9.

The material constants A_{dyn} and n_{dyn} were determined from the developed mathematical model (Eqs. 7.4–7.6) for various IRDes as shown in Table 7.2. It is noticed that the material constant n_{dyn} value increases with increasing IRD. A decrease in the Zener–Hollomon parameter leads to increase in the average DRXed grain size. Hence, average DRXed grain size increase with increasing IRD as shown in Fig. 7.9. The porosity decreases with increasing IRD of preforms, which facilitates faster diffusion rates of the grains during hot deformation. It is clearly observed from Table 7.3 that the average DRXed grain size increases with increasing IRD. On the other hand, the average DRXed grain size decreases with decreasing IRD. Therefore, the average DRXed grain size is also dependent on IRD. The above developed mathematical models of DRX can be used to calculate the DRXed grain size of sintered Al–4wt%B_4C composite for different IRDes.

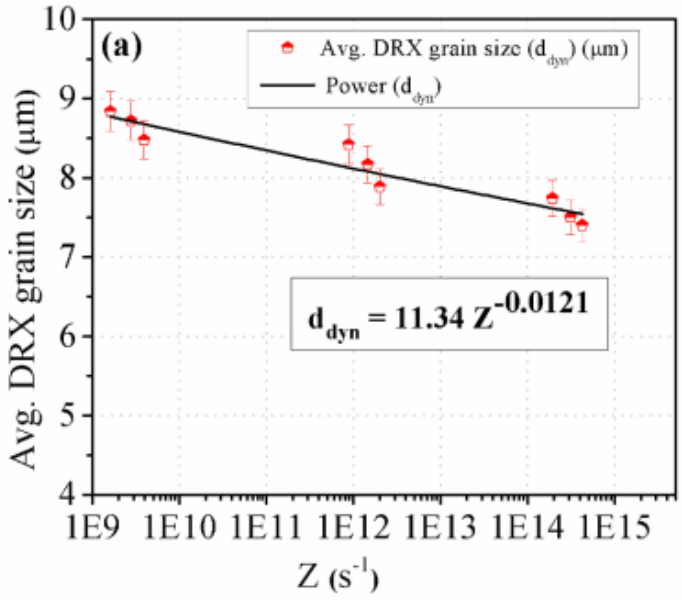

Fig. 7.4 Correlation between Zener–Hollomon parameters and average DRX grains size of P/M Al–4wt.%B_4C composite for IRD: (a) 80%.

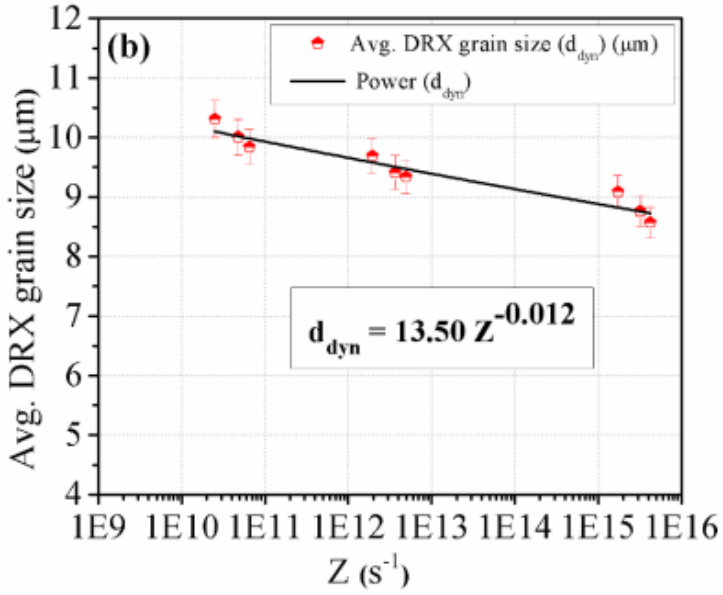

Fig. 7.5 Correlation between Zener–Hollomon parameters and average DRX grains size of P/M Al–4wt.%B_4C composite for IRD: (b) 85%.

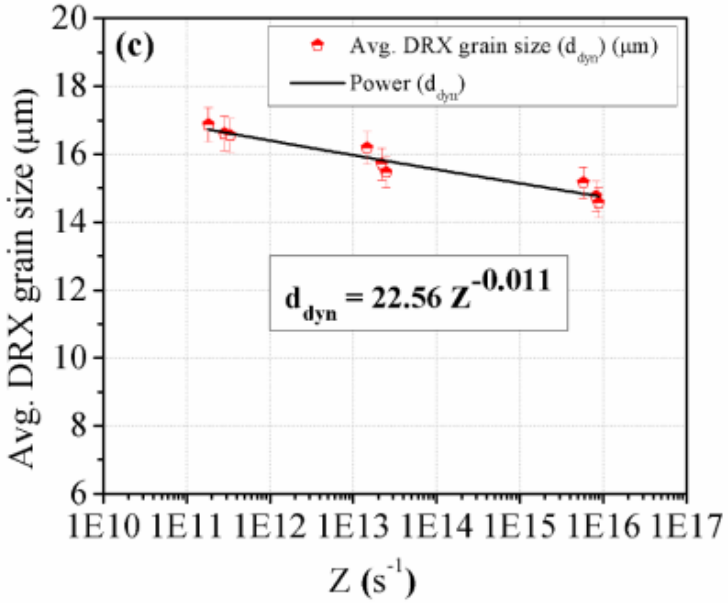

Fig. 7.6 Correlation between Zener–Hollomon parameters and average DRX grains size of P/M Al–4wt.%B_4C composite for IRD: (c) 90%.

Table 7.2 Values of A_{dyn} and n_{dyn} with different IRDes of Al–4wt.%B_4C composite

IRD (%)	A_{dyn}	n_{dyn}
80	11.34	-0.0121
85	13.50	-0.012
90	22.56	-0.011

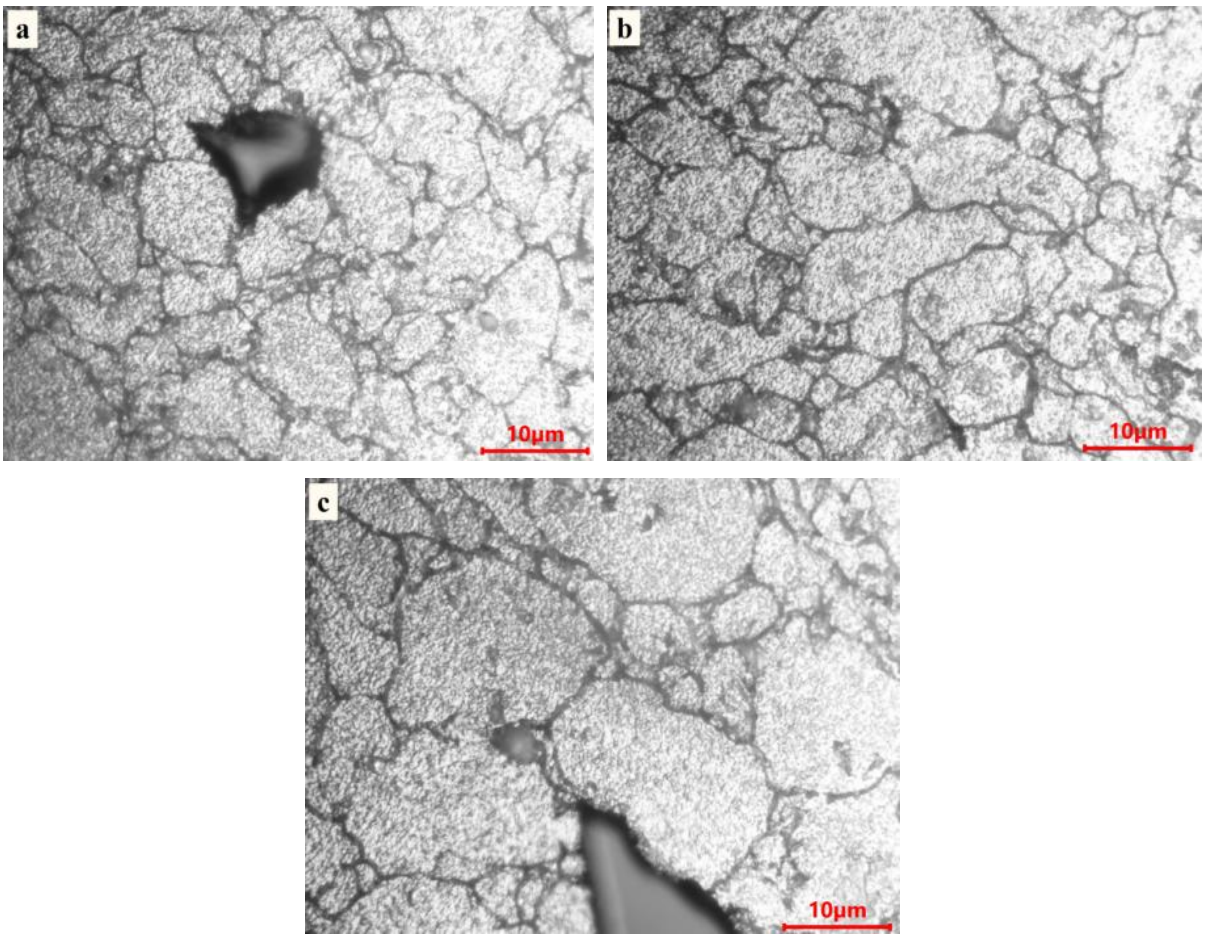

Fig. 7.7 Microstructures of Al–4wt.%B_4C deformed preforms for 90% IRD and strain rate of 0.1 s^{-1} at different temperatures: (a) 300 ^oC (b) 400 ^oC and (c) 500 ^oC.

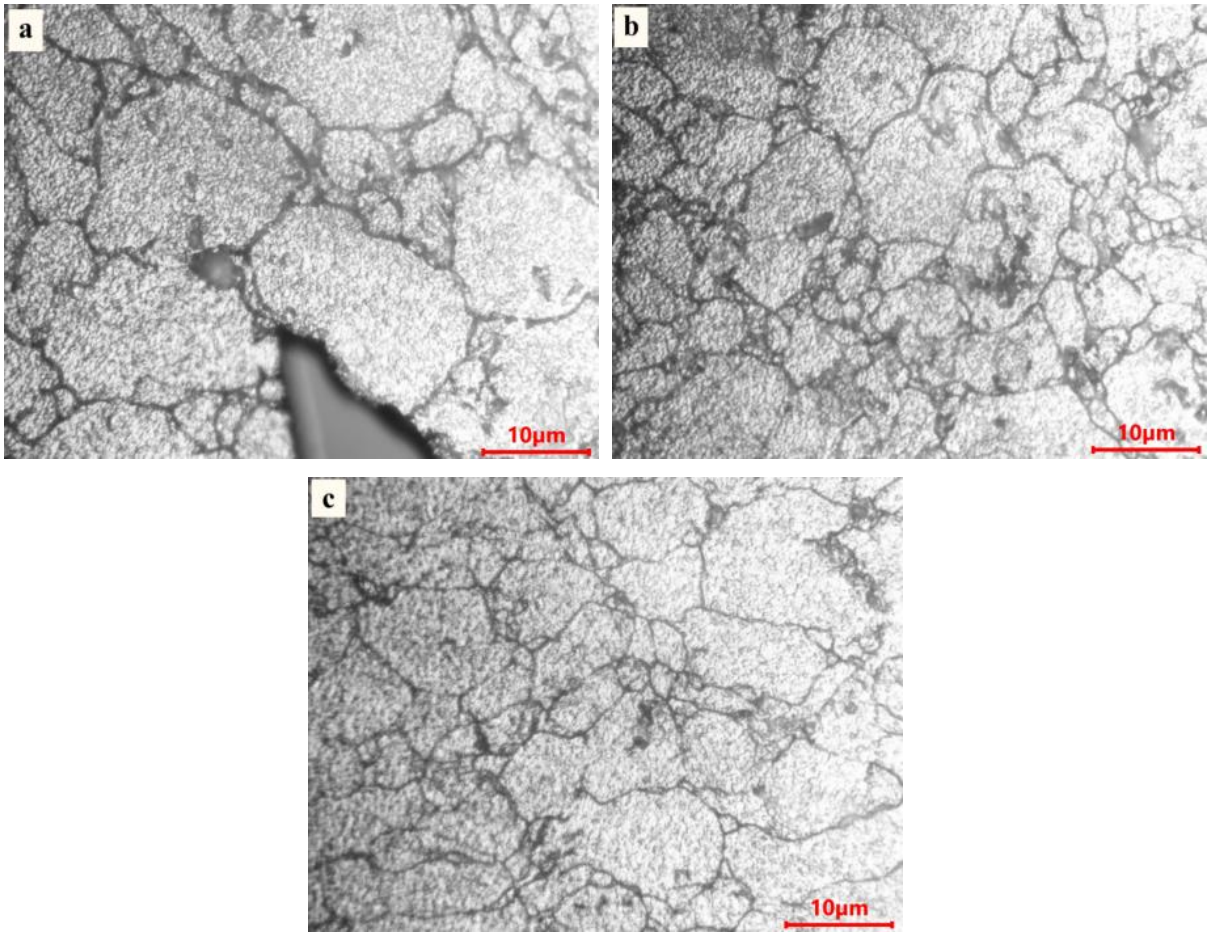

Fig. 7.8 Microstructures of Al–4wt.%B_4C deformed preforms for 90% IRD temperature of 500 ^oC at different strain rates: (a) 0.1 s^{-1} (b) 0.2 s^{-1} and (c) 0.3 s^{-1}.

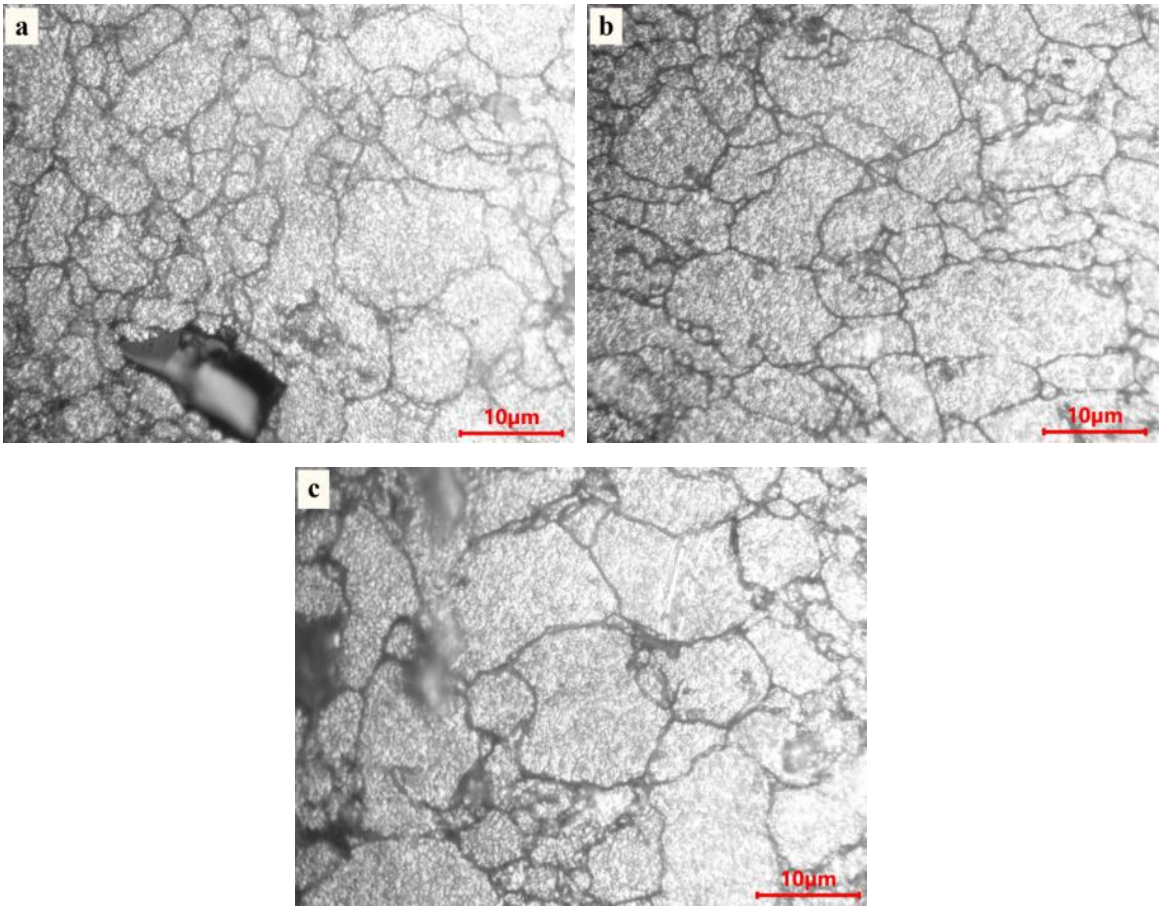

Fig. 7.9 Microstructures of Al–4wt.%B_4C deformed preforms with constant temperature of 400 ^oC and strain rate 0.2 s^{-1}at different IRDes: (a) 80% (b) 85% and (c) 95%.

7.4 Verification of developed mathematical model of sintered Al–4wt.%B_4C composite

The sizes of DRXed grains were calculated for each deformation condition using the developed model for various initial relative densities and are provided in Table 7.3. The calculated DRXed grains (d_c) are compared with measured DRXed grains (d_m) to evaluate the accuracy of the developed mathematical model of sintered Al–4wt.%B_4C composite for different IRDes. The plots drawn between measured and calculated average DRXed grain size for various IRDes are shown in Fig. 7.10 – 7.12. It is observed that most of the measured and calculated average DRXed grains are close to the best fit line which reflects the accuracy of the developed mathematical model. The R^2 values between measured and calculated average DRXed grain size are found to be 0.91, 0.92 and 0.93 for different IRDes of 80%, 85% and

90%, respectively, which indicates the calculated DRXed grains is well agreed with the measured DRXed grains for tested deformation conditions. It is also noticed that the prediction capability of the developed model is better for the higher IRD.

Moreover, the accuracy of the above developed mathematical model for sintered Al–4wt.%B_4C composite during hot deformation are confirmed by applying standard statistical parameter such as absolute error (δ) and mean absolute error (δ_m). The absolute error is determined from calculated and measured average DRXed grain size values by using Eq. (7.16).

$$\delta = \left|\frac{d_c - d_m}{d_m}\right| X\ 100\ \% \tag{7.16}$$

The detailed comparison made between the calculated and measured average DRXed grain sizes of sintered Al–4wt.%B_4C composite with different IRDes for each deformation condition are shown in Table 7.3. The average percentage error for various IRDes and deformation conditions were not exceeding 9.92% and mean absolute error does not exceed 8.58%. Further, it is observed that the developed mathematical models have the better predictive capability for lower strain rates and higher IRD during hot upsetting. Accordingly, the complete result shows that the calculated results have good agreement with the measured DRXed grain size results. This proves the precision and reliability of the developed mathematical model for sintered Al–4wt.%B_4C composite for various IRDes.

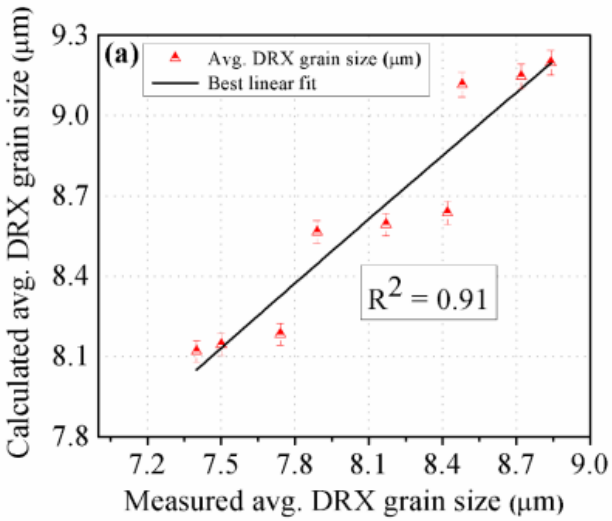

Fig. 7.10 Relationship between calculated and measured average DRX grain size of sintered Al–4wt.%B_4C composite for IRD: (a) 80%.

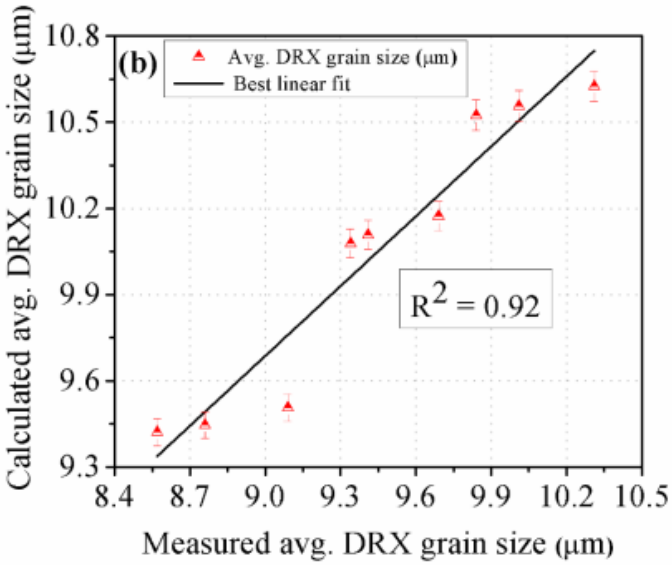

Fig. 7.11 Relationship between calculated and measured average DRX grain size of sintered Al–4wt.%B_4C composite for IRD: (b) 85%.

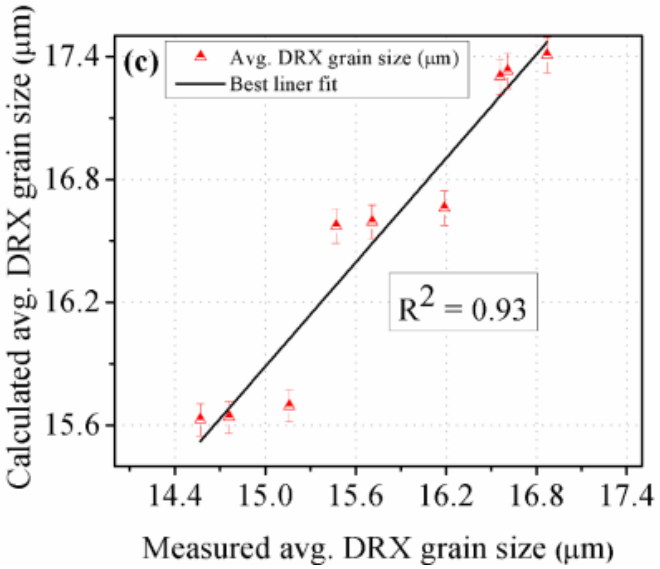

Fig. 7.12 Relationship between calculated and measured average DRX grain size of sintered Al–4wt.%B_4C composite for IRD: (c) 90%.

Table 7.3 Comparison between measured and calculated grains size of sintered Al–4wt.%B_4C composite for various IRDes, temperatures and strain rates

Def. Tem. (K)	ε̇ (s^{-1})	IRD = 80%				IRD = 85%				IRD = 90%			
		d_m (µm)	d_c (µm)	δ (%)	δ_m (%)	d_m (µm)	d_c (µm)	δ (%)	δ_m (%)	d_m (µm)	d_c (µm)	δ (%)	δ_m (%)
573	0.1	7.74	8.18	5.72	4.10	9.09	9.50	4.57	4.42	15.16	15.69	3.51	2.63
673	0.1	8.42	8.63	2.56		9.69	10.17	4.98		16.19	16.66	2.90	
773	0.1	8.84	9.19	4.04		10.31	10.62	3.05		16.87	17.40	3.18	
573	0.2	7.50	8.14	8.58	6.19	8.76	9.44	7.83	6.90	14.76	15.63	5.94	3.27
673	0.2	8.17	8.59	5.10		9.41	10.10	7.42		15.71	16.59	5.61	
773	0.2	8.72	9.14	4.89		10.01	10.55	5.46		16.61	17.32	4.33	
573	0.3	7.40	8.11	9.71	8.58	8.57	9.42	9.92	8.25	14.57	15.62	7.25	7.74
673	0.3	7.89	8.56	8.55		9.34	10.00	7.90		15.47	16.57	7.12	
773	0.3	8.48	9.11	7.49		9.84	10.52	6.95		16.56	17.30	4.48	

7.5 Summary

The DRX behavior of sintered Al–4wt.%B_4C preforms were studied by performing hot upsetting tests for different IRDes of 80%, 85% and 90%, and temperature range of 300 ^oC – 500 ^oC and strain rate range of 0.1 s^{-1} – 0.3 s^{-1}. The true stress (σ) – true strain (ε) curves of sintered Al–4wt.%B_4C deformed preforms were analyzed at various deformation condition. The activation energy and Zener–Hollomon parameter of sintered Al–4wt.%B_4C preforms were calculated for different deformation conditions. Mathematical models were developed between DRX size and Zener–Hollomon parameter to predict the DRXed grain size for various IRDes, temperatures and strain rates. The developed mathematical models were validated between the measured and calculated DRXed grain size for various deformation conditions.

CHAPTER 8

Conclusions and Scope for Future Work

8.1 Conclusions

The workability and densification behavior of sintered Al–B_4C composites (2%, 4% and 6% of B_4C) with 0.9 initial preform density have been studied by upsetting test over different deformation temperatures such as 200 ^oC, 300 ^oC, 400 ^oC and 500^oC under the tri–axial stress state condition. The hot deformation behavior and DRX grain behavior of sintered Al–4wt.%B_4C preforms were studied by performing hot upsetting tests for different IRDes of 80%, 85% and 90%, and temperature range of 300 ^oC – 500 ^oC and strain rate range of 0.1 s^{-1} – 0.3 s^{-1}. And also, mathematical models were developed for predicting the flow stress and grain size of the material for different deformation conditions. The following major observations are made from the studies such as

Workability and Densification Behavior of Al–B_4C Composite

- The three different stages of densification mechanism relating to the axial strain have been observed during hot deformation. In the stage-1, densification rate is faster with little increase of axial strain as the deformation load would be spending on closing the pores on the stage-1 of deformation.

- Densification rate gradually decreases during the stage-2 of the deformation path with increased axial strain and very little amount of densification was achieved during the stage-3 of the deformation.
- The amount of densification has been found to be higher for the higher deformation temperature and low percentage of B_4C content in the Al metal matrix. A maximum relative density of 0.95 was obtained at 500 ^oC deformation temperature for 2%B_4C content in the composite.
- The formability stress index has increased with the increase in the axial strain and relative density irrespective of the deformation temperature and B_4C content in the Al composite. The high formability stress index was observed in the case of 2%B_4C preforms composite for 500 ^oC deformation temperature.
- The plots drawn between the stress ratio parameters, namely ($\sigma_\theta/\sigma_{eff}$) and ($\sigma_m/\sigma_{eff}$) under the tri–axial stress state condition as a function of relative density revealed that the formability increased with the increase in deformation temperature and decrease in B_4C content.
- The formability stress index and relative density decrease with decreasing deformation temperature and increasing B_4C percentage in the aluminum matrix. The highest relative density and formability is attained in the Al–2%B_4C composite for 500 ^oC deformation temperatures for any given axial strains.

Constitute Modelling of Al–4wt. %B_4C Composite

- The influences of the IRD and deformation conditions on the σ–ε curves are significant for all tested conditions. The flow stress curves increases with increasing IRD and strain rate, and it decreases with deformation temperature.
- The IRD has a great influence on the hot deformation behavior of sintered Al–4wt.%B_4C composite. The activation energy of hot deformation exhibited higher values due to increase in IRD. In another way, the values of α decrease with increase in the IRD.
- The constitutive equations were developed between material constants and IRD for predicting the flow stress of sintered Al–4wt.%B_4C composite precisely.

- Comparison was made between the predicted and experimental values and it shows good agreement. The absolute error were not exceeding 10.6% and mean absolute error does not exceed 9.95% for various IRDes and deformation conditions.
- The activation energy (Q) calculated for sintered Al–4wt.%B_4C composite with IRDes of 80%, 85% and 90% was 161.06, 172.28 and 181.05 KJ/mol, respectively. This range of values is more than the value of self–diffusion of pure aluminum (144.3 KJ/mol).

Microstructure Evolution of Al–4wt. %B_4C Composite

- The DRXed grain size was measured by an intercept line method and it varies from 2 to 36 μm depending on the deformation conditions and IRDes.
- The dynamically recrystallized grain of sintered Al–4wt%B_4C preforms is significantly sensitive to the deformation condition such as temperature, strain, strain rate and initial relative density. The average DRX grain size increases with increase in the deformation temperature and IRD or with decrease in the strain rate and deformation degree.
- The grain size of the deformed Al–4wt%B_4C is also dependent on Z parameter that is a decreasing Z value leads to more adequate dynamic recrystallization.
- At the initial stage of deformation, the average DRX grain size considerably decreases with lower strain values than the higher strain values as during plastic deformation, the dislocation density increases considerably in the lower strain values.
- It is essential to increase the deformation degree and decrease the deformation temperature at appropriate strain rate to get uniform fine-grain microstructure in the forming process.
- Deformation degree and IRD appear to be the more dominant parameters on the grain size of the sintered Al–4wt%B_4C deformed preforms compared to deformation temperature and strain rate.

Microstructure modeling of Al–4wt.%B_4C Composite

- The activation energy and Zener–Hollomon parameter of sintered Al–4wt.%B_4C preforms were calculated for different temperatures, strain rates and IRDes and the investigated activation energies were more than the self–diffusion of pure aluminum (144.3 KJ/mol).
- Mathematical models were developed between dynamic recrystallization grain size and Zener–Hollomon parameter, which helps in calculating the DRXed grain size for various IRDes, temperatures and strain rates.

- Validation tests performed between the measured and calculated DRXed grain size revealed that the average percentage error for various IRDes and deformation conditions were not exceeding 9.92% and mean absolute error does not exceed 8.58%.
- The results of this work can be used to develop hot deformation regimes of Al–4wt.%B_4C preforms, providing a required DRXed grain size.

8.2 Scope for Future Work

The intensive work on experimental investigation and simulation on deformation and densification behavior of sintered Al–B_4C preforms can be extended to various dimensions such as:

1) The plastic deformation behavior and densification of sintered Al–B_4C preforms can be studied during extrusion process and development of flow stress model for the extruded billets at elevated temperature.
2) The grain size evolution and grain size model prediction work may be extended to various powder materials and forming processes.
3) Experimental investigation on the development of functionally graded materials (FGM) from Al and B_4C materials can be carried out for various applications through P/M process.
4) The friction behavior between tool-workpiece interfaces of sintered Al–B_4C preforms during deformation at elevated temperature can be studied.

REFERENCES

[1] C.C. Huang, J.H. Cheng, An investigation into the forming limits of sintered porous materials under different operational conditions, J. Mater. Process. Technol. 148 (2004) 382-393.

[2] R. Chanramouli, T.K. Kandavel, D. Shanmugasundaram, T. Ashok Kumar, Deformation and densification and corrosion studies of sinterd powder metallurgy plain carbon steel preform, Mater. Des. 28 (2007) 2260-2264.

[3] A. Badawy, Survey and recommendations on the selection of optimum powder forging temperature, J. Mater. Process. Technol. 6(1) (1998) 31-40.

[4] A. Rajeshkannan, K.S. Pandey, Some studies on barreling of powder preforms during cold upsetting, J. Mech. Beha. Mater. 17(6) (2006) 415-430.

[5] G. Poshal, P. Ganesan, An analysis of formability of aluminium preforms using neural network, J. Mater. Process. Technol. 205 (2008) 272-282

[6] R. Narayansamy, V. Anandakrishnan, K.S. Pandey, Effect of geometric work-hardening and matrix work-hardening on new constitutive relationship for aluminium-alumina P/M composite during upsetting, Int. J. Mech. Mater. Des. 4 (2008) 301-315.

[7] G.T. Brown, The powder forging process: a review of basic concept and development prospect, Powder Metall. 14(27) (1971) 124-143.

[8] K.S. Pandey, Salient characteristics of high temperature forging of ferrous preforms, Key Eng. Mater. 29-31(1989) 465-486.

[9] G. Sjoberg, Material flow and cracking in powder forging, Powder Metall. Inst. 7(1) (1975) 30-33.

[10] R. Narayansamy, T. Ramesh, K.S. Pandey, Some aspects on strain hardening behaviour in three dimensions of aluminium–iron powder metallurgy composite during cold upsetting, Mater. Des. 27 (2006) 640–650.

[11] M.A Rahman, M.N. El-Sheikh, Workability in forging of powder metallurgy compacts, J. Mater. Process. Technol. 54 (1995) 97-102.

[12] R. Narayanasamy, T. Ramesh, K.S. Pandey, Some aspects of workability studies in cold forging of pure aluminum powder metallurgy compacts, J. Mater. Sci. Technol. 21 (2005) 912-916.

[13] K.T. Kim, S.C. Lee, H.S. Ryu, Densification behavior of aluminium powder mixed with zirconia powder inclusion under cold compaction, Mater. Sci. Eng. A, 340 (2003) 41-48.

[14] S. Narayan, A. Rajeshkannan, Densification behaviour in forming of sintered iron-0.35% carbon powder metallurgy preform during cold upsetting, Mater. Des. 32(2011) 1006-1013.

[15] Y.C. Lin, C. Ming-Song, J. Zhong, Constitutive modeling for elevated temperature flow behavior of 42CrMo steel, Comput. Mater. Sci. 42 (2008) 470–477.

[16] Y. Yang, F. Li, Z. Yuan, H. Qiao, A modified constitutive equation for aluminium alloy reinforce by silicon carbide particles at elevated temperature, J. Mater. Eng. Perform. 22 (2013) 2641-2655.

[17] A. Etaati, K. Dehghani, A study on hot deformation behaviour of Ni-42.5Ti-7.5Cu alloy, Mater. Chem. Phys. (2013) 1-8.

[18] T. Senthilvelan, K. Raghukandan, A. Venkatraman, Modeling of process parameters on the working of P/M copper preforms, J. Mater. Process. Technol. 142 (2003) 767–772.

[19] H.A. Kuhn, C.L. Downey, Deformation characteristics and plasticity theory of sintered powder materials, Int. J. Powder Metall. 7 (1971) 15- 25.

[20] P. Venugopal, S. Venkatraman, Ring-compression tests on sintered iron preforms, J. Mech. Work. Technol. 16(1) (1988) 51–64.

[21] R. Narayanasamy, R. Ponalausamy, K.R. Subramanian, Generalized yield criteria of porous sintered powder metallurgy metals, J. Mater. Process. Technol. 110(2) (2001) 182-185.

[22] D. Li, Q. Guo, S. Guo, H. Peng, Z. Wu, The microstructure evolution and nucleation mechanisms of dynamic recrystallization in hot-deformed Inconel 625 superalloy, Mater. Des. 32 (2011) 696–705.

[23] M. Shaban, B. Eghbali, Characterization of austenite dynamic recrystallization under different Z parameters in a microalloyed steel, J. Mater. Sci. Technol. 27(4) (2011) 359-363.

[24] G.E. Kodzhaspirov, M.I. Terentyev, Modeling the dynamically recrystallized grain size evolution of a superalloy, Mater. Phys. Mech. 13 (2012) 70–76.

[25] H.C.H. Carpenter, J.M. Robertson, The metallography of some ancient Egyptian implements, J. Iron. Steel. Inst. 121 (1930) 417-448.

[26] G.S. Upadhyaya, Powder metallurgy technology, Cambridge International Science Publishing, 7 Meadow Walk, Great Abirgton, Cambridge CB1 6AZ, England, 1st ed. 2002, ISISN: 189826401.

[27] S.S.M. Nor, M.M. Rahman, F. Tarlochan, B. Shahida, A.K. Ariffin, The effect of lubrication in reducing net friction in warm powder compaction process, J. Mater. Process. Technol. 207 (2008) 118-124.

[28] H.A. Al-Qureshi, M.R.F. Soares, D. Hotza, M.C. Alves, A.N. Klein, Analyses of the fundamental parameters of cold die compaction of powder metallurgy, J. Mater. Process. Technol. 199 (2008) 417-424.

[29] W. Li, S.J. Park, P. Suri, A. Antonyraj, R.M. German, Investigation on die wear behaviour during compaction of aluminium matrix composite powders, Powder Metall. 54 (2011) 202-208.

[30] Z. Wang, X.H. Qu, H.Q. Yin, M.J. Yi, X.J. Yuan, High velocity compaction of ferrous powder, Powder Technol. 192 (2009) 131-136.

[31] J. Duszczyk, D. Bialo, The compaction of metal powders in rotary die pressing, Powder Metall. Int. 11(3) (1979) 103-105.

[32] G. Bockstiegel, O. Svensson, The influence of lubrication, die material and tool design upon die-wear in the compacting of iron powders, Modern Developments in

Powder Metallurgy, Proceedings of the International Conference sponsored by MPIF & APMI, 4 (1971) 87-125.

[33] J. Robertson, J.T. Im, I. Karaman, K.T. Hartwig, I.E. Anderson, Consolidation of amorphous copper based powder by equal channel angular extrusion, J.Non-Cryst. Solids 317 (2003) 144-151.

[34] A. Dudek, R. Wlodarczyk, Effect of sintering atmosphere on properties of porous stainless steel for biomedical applications, Mater. Sci. Eng. C, 33 (2013) 434-439.

[35] ASM International Handbook Committee, ASM Handbook-Powder Metal Technologies and Applications, ASM International 07 (1998).

[36] A.P.M. raj, N. Selvakumar, Deformation behavior of sintered Fe-C-Mnc composite during cold upset forming, Mater. Manuf. Process. 26 (2011) 1388–1392.

[37] A. Rajeshkannan, U. Mehta, Deformation Study of Sintered Iron – Carbon – Silicon – Copper Steel Compacts during Cold Forging, Mater. Manuf. Process. 29 (2014) 442–447.

[38] R. Narayanasamy, T. Ramesh, K.S. Pandey, An experimental investigation on strain hardening behavior of aluminium-3.5% alumina powder metallurgy composite preform under various stress states during cold upset forming, Mater. Des. 28 (2007) 1211-1223.

[39] K. Baskaran, R. Narayanasamy, An experimental investigation on work hardening behaviour of elliptical shaped billets of aluminium during cold upsetting, Mater. Des. 29 (2008) 1240–1265.

[40] N. Selvakumar, A.P. Mohan Raj, R. Narayanasamy, Experimental investigation on workability and strain hardening behaviour of Fe–C–0.5Mn sintered composites, Mater. Des. 41 (2012) 349–357.

[41] T.K Kandavel, R. Chandramouli, D. Shanmugasundaram, Experimental study of the plastic deformation and densification behaviour of some sintered low alloy P/M steels, Mater. Des. 30 (2009) 1768–1776.

[42] E. Parteder, H. Riedel, R. Kopp, Densification of sintered molybdenum during hot upsetting: experiments and modeling, Mater. Sci. Eng. A, 264 (1999) 17–25.

[43] D. Shanmugasundaram, R. Chandramouli, T.K. Kandavel, Cold and hot deformation and densification studies on sintered Fe-C-Cr-Ni low alloy P/M steels, Int. J. Adv. Manuf. Technol. 41 (2009) 8–15.

[44] J. Lu, J. Ma, Densification modeling studies on porous Al_2O_3 component, Powder Metall. Met. Ceram. 49(3-4) (2010)167-173.

[45] M. Abdel-Rahman, M.N. El-Sheikh, Workability in forging of powder metallurgy compacts, J. Mater. Sci. Process. Technol. 54(1–4) (1995) 97–102.

[46] V. Vujovic, A.H. Shabaik, A new workability criterion for ductile metals. J. Eng. Mater. Technol. 108 (1986) 245–249.

[47] S. Narayan, A. Rajeshkannan, Some Aspects of barreling in sintered plain carbon steel powder metallurgy preforms during cold upsetting, Mater. Res.15(2) (2012) 291- 299.

[48] R. Narayansamy, T. Ramesh, K.S. Pandey, Workability studies on cold upsetting of Al-Al_2O_3 composite material, Mater. Des. 27 (2006) 566-575.

[49] A.P.M. Raj, N. Selvakumar, R. Narayanasamy, C. Kailasanathan, Experimental investigation on workability and strain hardening behaviour of Fe–C–Mn sintered composites with different percentage of carbon and manganese content, Mater. Des. 49 (2013) 791–801

[50] Jin W, Jun C, Zhen Z, Xue-yu R, Hot deformation behavior and flow stress model of F40MnV steel, J. Cent. South Univ. Technol. 14 (1) (2007) 19−23.

[51] Y. Li, T.G. Langdon, High strain rate superplastisity in metal matrix composites: The role of load transfer, Acta mater. 46(11) (1998) 3937–3948.

[52] M.A.J. Taleghani, E.M.R. Navas, M. Salehi, J.M. Torralba, Hot deformation behaviour and flow stress prediction of 7075 aluminium alloy powder compacts during compression at elevated temperatures, Mater Sci. Eng: A 534 (2012) 624–631.

[53] J. Guo, S. Zhao, R. Murakami, R. Ding, S. Fan. Modeling the hot deformation behavior of Al alloy 3003, J. Alloys Compd. 566 (2013) 62–67.

[54] S. Gangolu, A.G. Rao, N. Prabhu, V.P. Deshmukh, B.P. Kashyap, Hot workability and flow characteristics of aluminum–5wt.% B_4C composite, J. Mater. Eng. Perform. 23(4) (2014) 1366–1373.

[55] R.Y. Zhang, Z.M. Shi, X.M. Zhang, Hot deformation behavior and microstructure evolution of TiC–Al_2O_3/Al composites, Rare Met. 34(10) (2015) 725–730.

[56] W.D. Wolla, M.J. Davidson, A.K. Khanra, Constitutive modeling of powder metallurgy processed Al–4%Cu preforms during compression at elevated temperature, Mater. Des. 65 (2015) 83–93.

[57] Y. Sun, W.H. Ye, L.X. Hu, Constitutive modeling of high–temperature flow behavior of Al–0.62Mg 0.73 Si aluminum alloy, J. Mater. Eng. Perform. 25(4) (2016) 1621–1630.

[58] R. Narayanasamy, V. Anandakrishnan, K.S. Pandey. Effect of geometric work–hardening and matrix work-hardening on workability and densification of aluminium–3.5% alumina composite during cold upsetting. Mater Des. 2008;29(8):1582–99.

[59] S. Serajzadeh, A.K. Taheri, Prediction of flow stress at hot working condition, Mech. Res. Commun. 30 (2002) 87-93.

[60] H. Mirzadeh, A. Najafizadeh, Flow stress prediction at hot working conditions, Mater. Sci. Eng. A, 527 (2010) 1160-1164.

[61] Q. Guo, D. Li, S. Guo, H. Peng, J. Hu, The effect of deformation temperature on the microstructure evolution of Inconel 625 superalloy, J. Nucl. Mater. 414(3) (2011) 440–450.

[62] T.W. Clyne, P.J. Withers, An introduction to metal matrix composites, Cambridge university press: Cambridge; 1993.

[63] T. Thevenot, Boron carbide – a comprehensive review, J. Eur. Ceram. Soc. 6(4) (1990) 205–225.

[64] R.M. Mohanty, K. Balasubramanian, Boron rich boron carbide: An emerging high performance material, Key. Eng. Mater. 395 (2009) 125–42.

[65] J. Abenojar, F. Velasco, M.A. Martinez, Optimization of processing parameters for the Al+10%B_4C systemobtained by mechanical alloying. J. Mater. Process. Technol. 184(1) (2007) 441–446.

[66] X.G. Chen, L. St-Georges, M. Roux, Mechanical behavior of high boron content Al-B_4C metal matrix composites at elevated temperatures, Mater. Sci. Forum. 706 (2012) 631–637.

[67] D.R. Kumar, R. Narayanasamy, C. Loganathan, Effect of glass and SiC in aluminum matrix on workability and strain hardening behavior of powder metallurgy hybrid composites, Mater. Des. 34 (2012) 120–136.

[68] R. Narayanasamy, T. Ramesh, K.S. Pandey, Some aspects on workability of aluminium–iron powder metallurgy composite during cold upsetting. J. Mater. Sci. Eng. A, 391(1) (2005) 418–26.

[69] N. Selvakumar, R. Narayanasamy, Phenomenon of strain hardening behaviour of sintered aluminium preforms during cold axial forming, J. Mater. Process. Technol. 142(2) (2003) 347–354.

[70] S. Mandal, V. Rakesh, P.V. Sivaprasad, S. Venugopal, K.V. Kasiviswanathan, Constitutive equations to predict high temperature flow stress in a Ti-modified austenitic stainless steel, Mater. Sci. Eng: A, 500(1) (2009) 114–121.

[71] M.R. Rokni, A. Zarei-Hanzaki, A.A. Roostaei, A. Abolhasani. Constitutive base analysis of a 7075 aluminum alloy during hot compression testing, Mater. Des. 32(10) (2011) 4955–4960.

[72] C. Zener, J.H. Hollomon, Effect of strain rate upon plastic flow of steel, J. Appl. Phys. 15(1) (1944) 22–32.

[73] R.S. Mishra, T.R. Bieler, A.K. Mukherjee, Superplastisity in powder metallurgy aluminum alloys and composites, Acta metall. Mater. 43(3) (1995) 877–891.

[74] Y. Li, T.G. Langdon. High strain rate superplastisity in metal matrix composites: The role of load transfer. Acta mater. 46(11) (1998) 3937–3948.

[75] W.F. Gale, T.C. Totemeier, Smithells metals reference book. 7th ed. Butterworth-Heinemann: Woburn, 1992.

[76] H. Zhang, K. Zhang, S. Jiang, H. Zhou, C. Zhao, X. Yang, Dynamic recrystallization behavior of a γ'-hardened nickel-based superalloy during hot deformation, J. Alloys Compd. 623 (2015) 374–385.

[77] H. Zhang, K. Zhang, H. Zhou, Z. Lu, C. Zhao, X. Yang, Effect of strain rate on microstructure evolution of a nickel-based superalloy during hot deformation, Mater. Des. 80 (2015) 51–62.

[78] Q. M. Guo, D. F. Li, S. L. Guo, Microstructural models of dynamic recrystallization in hot-deformed Inconel 625 superalloy, Mater. Manuf. Process. 27 (2012) 990–995.

[79] Y.C. Lin, M.S. Chen, J. Zhong, Microstructural evolution in 42CrMo steel during compression at elevated temperatures, Mater. Lett. 62 (2008) 2132–2135.

[80] C.Z. Nie, J.J. Gu, J.L. Liu, D. Zhang, Production of boron carbide reinforced 2024 aluminum matrix composites by mechanical alloying, Mater. Trans. 48(5) (2007) 990–995.

[81] X.M. Chen, Y.C. Lin, D.X. Wen, J.L. Zhang, M. He, Dynamic recrystallization behavior of a typical Nickel-based superalloy during hot deformation, Mater. Des. 57 (2014) 568–577.

[82] K.V.A. Chakravarthi, N.T.B. Koundinya, S.V.S.N. Murty, B.N. Rao, Microstructural evolution and constitutive relationship of M350 grade maraging steel during hot deformation, J. Mater. Eng. Perform. 26(3) (2017) 1174–1185.

[83] X.M. Chen, Y.C. Lin, M.S. Chen, H.B. Li, D.X. Wena, J.L. Zhang, M. He, Microstructural evolution of a Nickel-based during hot deformation, Mater. Des. 77 (2015) 41–49.

[84] F. Ren, F. Chen, J. Chen, Investigation on dynamic recrystallization behavior of martensitic stainless steel, Adv. Mater. Sci. Eng. (2014).

[85] F. Bedir, Modeling approach and plastic deformation analysis of 6063 aluminum alloy during compression at elevated temperatures, Mater. Des. 49 (2013) 953–956.

[86] F. Chen, Z. Cui, S. Chen, Recrystallization of 30Cr2Ni4MoV ultra-super-critical rotor steel during hot deformation. Part I: dynamic recrystallization, Mater. Sci. Eng. A, 528 (2011) 5073–5080.

[87] M. Zhou, Y.C. Lin, J. Deng, Y.Q. Jiang, Hot Tensile deformation behaviors and constitutive model of an Al–Zn–Mg–Cu alloy, Mater. Des. 59 (2014) 141–150.

[88] T. Matsui, H. Takizawa, H. Kikuchi, S. Wakita, The Microstructure prediction of alloy 720LI for turbine disk applications, Superalloys, (2000) 127–133.

LIST OF PUBLICATIONS

Journals

1. R. Seetharam, S. Kanmani Subbu, M. J. Davidson. Hot workability and densification behavior of sintered powder metallurgy Al-B_4C preforms during upsetting. ***Journal of Manufacturing Processes, 28 (2017) 309 – 318 Elsevier. Impact Factor = 2.322 (SCI).***

2. R. Seetharam, S. Kanmani Subbu, M. J. Davidson. Microstructure modeling of dynamically recrystallization grain size of sintered Al–4%B_4C composite during hot upsetting. ***Journal of Engineering Materials and Technology 140(2) (2018), 021003. ASME. Impact Factor = 1.141 (SCI).***

3. R. Seetharam, S. Kanmani Subbu, M. J. Davidson. Analysis of grain size evolution of sintered Al–4wt%B_4C preforms subjected to hot compression. ***Journal of Metallography, Microstructure and Analysis, 7(2018), 176-183. (ESCI, Spinger)***

4. R. Seetharam, S. Kanmani Subbu and M. J. Davidson. Workability behavior of sintered Al-4%B_4C preforms during cold and hot upsetting. ***Procedia Engineering, 173 (2017) 910–917. Elsevier (Scopus).***

5. R. Seetharam, S. Kanmani Subbu, M. J. Davidson. Modeling flow behavior of sintered Al-4%B_4C composite during high-temperature upsetting. ***Submitted in Journals of Materials Engineering and Performance. (SCI), (Under review).***

Internationals Conferences

1. R. Seetharam, S. Kanmani Subbu and M. J. Davidson. Workability Behavior of Sintered Al-4%B_4C Preforms During Cold and Hot Upsetting. ***11th International Symposium on Plasticity and Impact Mechanics (IMPLAST-2016), IIT Delhi.***

2. R. Seetharam, S. Kanmani Subbu and M. J. Davidson. Densification and Flow Behavior of Sintered Al-4%B_4C Composite during Hot Upsetting. ***Proceedings of 6th International & 27th All India Manufacturing Technology, Design and Research Conference (AIMTDR-2016). College of Engineering, Pune.***

Brief Biography of the Candidate

Mr. R Seetharam comes from Nagarkarnool, Telangana. He attended the Osmania University, Hyderabad where he received his B.E degree in Mechanical (Production) Engineering with first class in June 2011. He then went for advanced degrees, M.Tech, in Production Engineering with specialization in Manufacturing Technology from National Institute of Technology, Trichy, with distinction, in June 2013. He then worked for one year as an Assistant professor in Vivekananda Group of Institutions, Hyderabad from July 2013 to July 2014. **Mr. R Seetharam** joined the Department of Mechanical Engineering, National Institute of Technology, Warangal, India for pursuing his Ph.D degree in June, 2014. His research works focus on metal forming of composite materials namely, aluminium-boron carbide composite, processed by powder metallurgical route which is mainly used in various applications such as defense, nuclear industry, and other areas. **Mr. Seetharam** is submitting his Ph.D. research work on metal flow analysis and microstructure modelling of hot upset Al-B_4C composite. He published his research findings in SCI Journals. **Mr. Seetharam** has a strong desire and passion to continue his research works after Ph.D. on various areas namely, processing of advanced materials, modeling and simulation of advanced manufacturing processes, functionally graded materials, and nanomaterials.

APPENDICES

Appendix I Hot compression test data of P/M Al–2wt.%B_4C preforms at 200 ^oC deformation temperature and 90% of IRD.

Sample No.	D_o (mm)	H_o (mm)	D_{tc} (mm)	D_{bc} (mm)	D_b (mm)	H_f (mm)	Load (kN)	ρ_{final}	σ_z (MPa)	ε_z	σ_θ (MPa)	ε_θ	σ_m (MPa)	α	σ_{eff} (MPa)	β_σ	$\sigma_\theta/\sigma_{eff}$	σ_m/σ_{eff}
1	15.07	15.24	15.07	15.07	15.07	15.24	0	0.899	0	0	-	0	-	-	-	-	-	-
2	15.05	14.98	15.1	15.14	15.16	14.74	9.16	0.906	50.99	0.016	44.99	0.01	46.99	0.396	43.48	3.24	1.03	1.08
3	15.06	15.04	15.22	15.24	15.4	14.40	18.32	0.912	100.5	0.043	90.34	0.03	93.73	0.428	82.10	3.42	1.10	1.14
4	15.05	14.94	15.66	15.73	16.52	12.74	27.48	0.917	142	0.159	130.12	0.15	134.07	0.481	112.76	3.56	1.15	1.18
5	15.06	15.00	16.44	16.48	18.03	10.87	36.64	0.925	172.1	0.322	158.65	0.30	163.14	0.470	127.97	3.82	1.23	1.27
6	15.06	15.01	17.58	17.6	19.81	9.42	46	0.929	189.2	0.466	176.70	0.47	180.87	0.509	136.22	3.98	1.29	1.32
7	15.06	15.02	18.76	18.84	21.00	8.40	55	0.931	198.1	0.581	185.36	0.59	189.59	0.513	140.64	4.04	1.31	1.34

Model Calculations of Appendix I– XXIX

Sample No-2 (Appendix-I)

Initial Daimeter (D_o) = 15.05 mm

Initial Height (H_o) = 14.98 mm

Top Contact Daimeter (D_{tc}) = 15.1 mm

Bottom Contact Daimeter (D_{bc}) = 15.14 mm

Bulge Diameter (D_b) = 15.16 mm

Final Height (H_f) = 14.74 mm

Final Density (ρ_f) = 0.906

Load = 9.16 kN = 9160 N

Average Contact Diameter (D_c) = (D_{ct} + D_{cb})/2

= (15.1+15.14)/2

= 15.12 mm

Average Contact Area (Contact surface area) = $\frac{\pi}{4} D_c^2$

= $\frac{\pi}{4} 15.12^2$

= 179.11 mm^2

Axial Strain $(\varepsilon_z) = \ln\left(\frac{H_f}{H_o}\right)$

$(\varepsilon_z) = \ln\left(\frac{14.74}{14.98}\right)$

= 0.016

Axial Stress (σ_z) = $\frac{load}{contact\ surface\ area}$

$\sigma_z = \frac{9160}{179.11}$

σ_z = 50.99 MPa

Hoop Strain $(\varepsilon_\theta) = \ln\left[\frac{2D_B^2 + D_C^2}{3D_o^2}\right]$

$$\varepsilon_\theta = \ln\left[\frac{2\ X\ 15.16^2 + 15.12^2}{3\ X\ 15.05^2}\right]$$

$$\varepsilon_\theta = 0.012$$

Poisson's Ratio $(\alpha) = \frac{\varepsilon_\theta}{2\varepsilon_z}$

$$(\alpha) = \frac{0.012}{2\ X\ 0.016}$$

$$\alpha = 0.396$$

Hoop Stress$(\sigma_\theta) = \left[\frac{2\alpha + R^2}{2 - R^2 + 2R^2\alpha}\right]\ \sigma_z$

$$= \left[\frac{2\ X\ 0.396 + 0.906^2}{2 - 0.906^2 + 2X\ 0.906^2 X\ 0.396}\right]\ X\ 50.99$$

$$\sigma_\theta = 44.99 \text{ MPa}$$

Hydrostatic Stress (σ_m) = $\sigma_m = \frac{\sigma_r + \sigma_\theta + \sigma_z}{3} = \frac{2\ \sigma_\theta + \sigma_z}{3}$

$$\sigma_m = \frac{2\ X\ 44.9 + 50.99}{3}$$

$$\sigma_m = 46.99 \text{ MPa}$$

Sffective Stress $(\sigma_{eff}) = \left[\frac{\sigma_z^2 + 2\sigma_\theta^2 - R^2(\sigma_\theta^2 + 2\sigma_z\sigma_\theta)}{2R^2 - 1}\right]^{0.5}$

$$\sigma_{eff} = \left[\frac{50.99^2 + 2\ X\ 44.99^2 - 0.906^2(44.99^2 + 2\ X\ 50.99\ X\ 44.99)}{2\ X\ 0.906^2 - 1}\right]^{0.5}$$

$$\sigma_{eff} = 43.48 \text{ MPa}$$

Formability Stress Index $(\beta_\sigma) = \left(\frac{3\sigma_m}{\sigma_{eff}}\right)$

$$\beta_\sigma = \left(\frac{3\ X\ 46.99}{43.48}\right)$$

$$\beta_\sigma = 3.24$$

Hoop Stress Ratio Parameter ($\sigma_\theta/\sigma_{eff}$) = 44.99/43.48

$$\sigma_\theta/\sigma_{eff} = 1.03$$

Hydrostatic Stress Ratio Parameter (σ_m/σ_{eff}) = 46.99/43.48

$$\sigma_m/\sigma_{eff} = 1.08$$

Similarly, all stresses and strains and formability stress index were calculated for various deformation temperatures, strain rates and compositions as shown in Appendix I-XXXIX.

Appendix II Hot compression test data of P/M Al–2wt.%B_4C preforms at 300 ^oC deformation temperature and 90% of IRD.

Sample No.	D_o (mm)	H_o (mm)	D_{tc} (mm)	D_{bc} (mm)	D_b (mm)	H_f (mm)	Load (kN)	ρ_{final}	σ_z (MPa)	ε_z	σ_θ (MPa)	ε_θ	σ_m (MPa)	α	σ_{eff} (MPa)	β_σ	$\sigma_\theta/\sigma_{eff}$	σ_m/σ_{eff}
1	15.05	14.8	15.05	15.05	15.05	14.8	0	0.898	0	0	-	0	-	-	-	-	-	-
2	15.05	14.92	15.13	15.15	15.17	14.66	8.83	0.907	49.02	0.02	43.53	0.01	45.36	0.414	41.80	3.26	1.04	1.09
3	15.06	15.01	15.33	15.25	15.56	14.21	17.66	0.913	96.14	0.05	87.96	0.05	90.69	0.491	78.82	3.45	1.11	1.15
4	15.04	15.02	15.7	15.87	16.8	12.7	26.49	0.922	135.31	0.17	126.31	0.18	129.31	0.541	104.12	3.73	1.21	1.24
5	15.05	14.95	16.64	16.89	18.69	10.61	35.32	0.932	159.94	0.34	150.41	0.37	153.59	0.533	112.82	4.08	1.33	1.36
6	15.04	14.9	18.16	18.53	20.71	9.12	44.1	0.932	166.78	0.49	158.08	0.57	160.98	0.576	117.91	4.1	1.34	1.37
7	15.04	14.85	19	19.33	21.64	8.24	53	0.934	183.65	0.59	173.71	0.65	177.02	0.554	127.19	4.18	1.36	1.39

Appendix III Hot compression test data of P/M Al–2wt.%B_4C preforms at 400 ^oC deformation temperature and 90% of IRD.

Sample No.	D_o (mm)	H_o (mm)	D_{tc} (mm)	D_{bc} (mm)	D_b (mm)	H_f (mm)	Load (kN)	ρ_{final}	σ_z (MPa)	ε_z	σ_θ (MPa)	ε_θ	σ_m (MPa)	α	σ_{eff} (MPa)	β_σ	$\sigma_\theta/\sigma_{eff}$	σ_m/σ_{eff}
1	15.06	14.97	15.06	15.06	15.06	14.97	0	0.9	0	0	-	0	-	-	-	-	-	-
2	15.05	14.98	15.1	15.12	15.16	14.7	6.83	0.917	38.07	0.02	33.33	0.01	34.91	0.328	29.64	3.53	1.124	1.18
3	15.06	14.97	15.16	15.18	15.32	14.16	13.7	0.92	75.76	0.06	64.64	0.03	68.35	0.249	57.35	3.58	1.127	1.19
4	15.04	14.93	15.54	15.86	16.64	12.6	20.5	0.931	105.85	0.17	98.52	0.16	100.96	0.486	74.92	4.04	1.315	1.35
5	15.05	14.98	16.44	16.76	18.44	10.39	28	0.934	129.32	0.37	120.23	0.34	123.26	0.466	89.02	4.15	1.351	1.38
6	15.05	14.93	17.34	17.63	19.65	9.02	34.17	0.937	142.25	0.5	132.50	0.46	135.75	0.458	94.96	4.29	1.395	1.43
7	15.05	14.99	18.46	18.64	20.98	8.08	41	0.940	151.65	0.62	142.16	0.59	145.32	0.476	98.94	4.41	1.437	1.47

Appendix IV Hot compression test data of P/M Al–2wt.%B_4C preforms at 500 ^oC deformation temperature and 90% of IRD.

Sample No.	D_o (mm)	H_o (mm)	D_{tc} (mm)	D_{bc} (mm)	D_b (mm)	H_f (mm)	Load (kN)	ρ_{final}	σ_z (MPa)	ε_z	σ_θ (MPa)	ε_θ	σ_m (MPa)	α	σ_{eff} (MPa)	β_σ	$\sigma_\theta/\sigma_{eff}$	σ_m/σ_{eff}
1	15	14.96	15	15	15.00	14.96	0	0.901	0	-	-	0	-	-	-	-	-	-
2	15.05	14.9	15.14	15.16	15.26	14.58	5.94	0.922	32.93	0.02	30.653	0.02	31.41	0.528	25.36	3.72	1.208	1.24
3	15.06	14.95	15.21	15.25	15.60	13.96	11.87	0.93	65.13	0.07	59.314	0.05	61.25	0.399	46.27	3.97	1.282	1.32
4	15.07	14.99	15.55	16.02	16.82	12.1	17.81	0.936	90.97	0.21	83.866	0.18	86.23	0.418	61.39	4.21	1.366	1.40
5	15.05	14.9	16.36	16.88	18.50	9.96	23.75	0.938	109.43	0.4	101.37	0.35	104.06	0.429	72.56	4.3	1.397	1.43
6	15.05	14.92	17.5	18.06	20.22	8.52	29.66	0.945	119.41	0.56	112.25	0.51	114.64	0.457	73.32	4.69	1.531	1.56
7	15.06	14.95	18.05	18.66	21.98	7.92	35.6	0.949	134.49	0.64	128.06	0.65	130.2	0.511	79.42	4.92	1.612	1.64

Appendix V Hot compression test data of P/M Al–4wt.%B_4C preforms at 200 ^oC deformation temperature and 90% of IRD.

Sample No.	D_o (mm)	H_o (mm)	D_{tc} (mm)	D_{bc} (mm)	D_b (mm)	H_f (mm)	Load (kN)	ρ_{final}	σ_z (MPa)	ε_z	σ_θ (MPa)	ε_θ	σ_m (MPa)	α	σ_{eff} (MPa)	β_σ	$\sigma_\theta/\sigma_{eff}$	σ_m/σ_{eff}
1	15.08	15.36	15.08	15.08	15.08	15.36	0	0.901	0	0	-	0	-	-	-	-	-	-
2	15.09	15.23	15.16	15.18	15.22	15.01	8	0.906	44.24	0.01	40.43	0.01	41.70	0.514	38.443	3.25	1.05	1.08
3	15.11	15.36	15.23	15.24	15.36	14.75	16	0.909	87.73	0.04	76.10	0.03	79.98	0.338	72.737	3.30	1.05	1.10
4	15.09	15.09	15.48	15.54	16.13	13.31	24	0.917	126.98	0.13	114.67	0.11	118.77	0.430	100.77	3.54	1.14	1.18
5	15.08	15.2	16.08	16.09	17.51	11.66	32	0.919	157.41	0.27	143.79	0.25	148.33	0.463	123.36	3.61	1.17	1.20
6	15.08	15.21	17.11	17.26	19.01	10.14	40	0.926	172.38	0.41	159.82	0.40	164.01	0.494	128.07	3.84	1.25	1.28
7	15.08	15.32	18.24	18.29	20.64	8.83	48	0.928	183.12	0.55	170.51	0.55	174.71	0.502	133.14	3.94	1.28	1.31

Appendix VI Hot compression test data of P/M Al–4wt.%B_4C preforms at 300 ^oC deformation temperature and 90% of IRD.

Sample No.	D_o (mm)	H_o (mm)	D_{tc} (mm)	D_{bc} (mm)	D_b (mm)	H_f (mm)	Load (kN)	ρ_{final}	σ_z (MPa)	ε_z	σ_θ (MPa)	ε_θ	σ_m (MPa)	α	σ_{eff} (MPa)	β_σ	$\sigma_\theta/\sigma_{eff}$	σ_m/σ_{eff}
1	15.09	15.09	15.09	15.09	15.09	15.09	0	0.894	0	0	-	0	-	-	-	-	-	-
2	15.08	15.09	15.11	15.13	15.15	14.84	6.83	0.907	38.02	0.02	31.43	0.01	33.63	0.238	31.67	3.19	0.99	1.06
3	15.08	15.31	15.16	15.19	15.24	14.57	13.66	0.912	75.49	0.05	61.40	0.02	66.10	0.184	60.20	3.29	1.02	1.1
4	15.08	15.36	15.45	15.5	15.94	13.49	20.49	0.921	108.90	0.13	96.67	0.09	100.75	0.353	82.67	3.66	1.17	1.22
5	15.08	15.31	15.83	15.88	16.92	11.61	27.33	0.929	138.37	0.28	123.85	0.19	128.69	0.341	98.48	3.92	1.26	1.31
6	15.08	15.22	16.6	16.94	18.69	9.42	34.16	0.931	154.59	0.48	140.19	0.36	144.99	0.377	108.55	4.01	1.29	1.34
7	15.08	15.29	18.13	18.34	20.41	8.59	41	0.931	156.93	0.58	145.37	0.54	149.23	0.465	110.97	4.03	1.31	1.34

Appendix VII Hot compression test data of P/M Al–4wt.%B_4C preforms at 400 ^oC deformation temperature and 90% of IRD.

Sample No.	D_o (mm)	H_o (mm)	D_{tc} (mm)	D_{bc} (mm)	D_b (mm)	H_f (mm)	Load (kN)	ρ_{final}	σ_z (MPa)	ε_z	σ_θ (MPa)	ε_θ	σ_m (MPa)	α	σ_{eff} (MPa)	β_σ	$\sigma_\theta/\sigma_{eff}$	σ_m/σ_{eff}
1	15.08	15.13	15.08	15.08	15.08	15.13	0	0.897	0	0	0	0	0	0	0	0	0	0
2	15.08	15.24	15.11	15.13	15.16	14.98	6	0.917	33.40	0.02	28.43	0.01	30.09	0.256	25.84	3.49	1.1	1.16
3	15.08	15.27	15.17	15.18	15.26	14.49	12	0.919	66.32	0.05	55.04	0.02	58.80	0.191	50.10	3.52	1.1	1.17
4	15.08	15.25	15.36	15.45	15.95	12.94	19	0.93	101.90	0.16	89.48	0.09	93.62	0.273	70.98	3.96	1.26	1.32
5	15.08	15.25	15.57	15.64	16.86	10.67	24	0.934	125.44	0.36	109.81	0.17	115.02	0.244	84.50	4.08	1.3	1.36
6	15.08	15.13	16.6	16.96	18.57	9.19	30	0.937	135.6	0.50	123.35	0.35	127.43	0.354	89.75	4.26	1.37	1.42
7	15.08	15.21	17.84	18.24	20.13	8.29	36	0.939	140.79	0.61	130.36	0.51	133.83	0.42	92.2	4.35	1.41	1.45

Appendix VIII Hot compression test data of P/M Al–4wt.%B_4C preforms at 500 ^oC deformation temperature and 90% of IRD.

Sample No.	D_o (mm)	H_o (mm)	D_{tc} (mm)	D_{bc} (mm)	D_b (mm)	H_f (mm)	Load (kN)	ρ_{final}	σ_z (MPa)	ε_z	σ_θ (MPa)	ε_θ	σ_m (MPa)	α	σ_{eff} (MPa)	β_σ	$\sigma_\theta/\sigma_{eff}$	σ_m/σ_{eff}
1	15.08	15.16	15.08	15.08	15.08	15.16	0	0.897	0	0	-	0	-	-	-	-	-	-
2	15.08	15.14	15.19	15.21	15.3	14.83	7	0.921	38.56	0.02	36.37	0.02	37.10	0.595	30.03	3.71	1.21	1.24
3	15.08	15.31	15.29	15.31	15.65	14.35	12	0.926	65.24	0.06	60.00	0.06	61.75	0.458	48.19	3.84	1.25	1.28
4	15.08	15.14	15.76	16.06	17.14	12.26	19	0.933	95.53	0.21	89.30	0.21	91.37	0.495	66.22	4.14	1.35	1.38
5	15.08	15.32	16.72	17.15	18.9	10.29	26.66	0.937	118.31	0.4	110.71	0.38	113.24	0.482	79.29	4.28	1.4	1.43
6	15.08	15.16	17.94	18.34	20.24	8.69	32	0.943	123.77	0.56	116.23	0.52	118.74	0.468	78.22	4.55	1.49	1.52
7	15.08	15.08	18.24	18.86	21.02	8.07	34.16	0.945	126.35	0.63	118.92	0.59	121.40	0.47	78.42	4.64	1.52	1.55

Appendix IX Hot compression test data of P/M Al–6wt.%B_4C preforms at 200 ^oC deformation temperature and 90% of IRD.

Sample No.	D_o (mm)	H_o (mm)	D_{tc} (mm)	D_{bc} (mm)	D_b (mm)	H_f (mm)	Load (kN)	ρ_{final}	σ_z (MPa)	ε_z	σ_θ (MPa)	ε_θ	σ_m (MPa)	α	σ_{eff} (MPa)	β_σ	$\sigma_\theta/\sigma_{eff}$	σ_m/σ_{eff}
1	15.08	15.15	15.08	15.08	15.08	15.15	0	0.905	0	0	-	0	-	-	-	-	-	-
2	15.06	15.1	15.11	15.13	15.14	14.9	8.66	0.906	48.21	0.01	42.01	0.01	44.08	0.364	41.12	3.22	1.02	1.07
3	15.06	15.00	15.21	15.25	15.35	14.51	17.36	0.909	95.25	0.03	86.89	0.03	89.68	0.496	80.70	3.33	1.08	1.11
4	15.06	15.21	15.90	16.02	16.83	13.66	26.02	0.910	130.00	0.11	127.88	0.19	128.59	0.875	113.94	3.39	1.12	1.13
5	15.06	15.18	16.84	16.91	18.32	11.85	34.68	0.913	155.00	0.25	147.99	0.34	150.33	0.687	130.43	3.46	1.13	1.15
6	15.06	15.10	18.00	18.36	20.07	10.11	43.34	0.918	166.90	0.4	158.39	0.51	161.22	0.639	134.38	3.6	1.18	1.2
7	15.06	15.18	19.27	19.32	21.46	8.85	52.00	0.919	177.80	0.54	167.45	0.64	170.89	0.595	140.74	3.64	1.19	1.21

Appendix X Hot compression test data of P/M Al–6wt.%B_4C preforms at 300 ^oC deformation temperature and 90% of IRD.

Sample No.	D_o (mm)	H_o (mm)	D_{tc} (mm)	D_{bc} (mm)	D_b (mm)	H_f (mm)	Load (kN)	ρ_{final}	σ_z (MPa)	ε_z	σ_θ (MPa)	ε_θ	σ_m (MPa)	α	σ_{eff} (MPa)	β_σ	$\sigma_\theta/\sigma_{eff}$	σ_m/σ_{eff}
1	15.07	15.23	15.07	15.07	15.07	15.23	0	0.901	0	0	-	0	-	-	-	-	-	-
2	15.06	15.15	15.1	15.12	15.14	14.94	7.13	0.906	39.75	0.01	34.23	0.01	36.07	0.332	33.65	3.22	1.02	1.07
3	15.06	15.12	15.15	15.19	15.24	14.59	14.26	0.912	78.86	0.04	67.40	0.02	71.22	0.29	63.82	3.35	1.06	1.12
4	15.06	15.00	15.29	15.43	16.07	13.41	21.39	0.912	115.40	0.11	104.25	0.1	107.96	0.449	94.87	3.41	1.1	1.14
5	15.06	15.09	15.83	16.23	17.26	11.63	28.37	0.917	140.50	0.26	127.04	0.23	131.53	0.433	111.58	3.54	1.14	1.18
6	15.06	15.00	16.81	17.18	18.67	9.86	35.50	0.923	156.40	0.42	142.78	0.37	147.33	0.442	118.46	3.73	1.21	1.24
7	15.06	15.05	18.12	18.48	20.46	8.65	41.00	0.924	155.80	0.55	144.11	0.54	148.02	0.491	117.45	3.78	1.23	1.26

Appendix XI Hot compression test data of P/M Al–6wt.%B_4C preforms at 400 ^oC deformation temperature and 90% of IRD.

Sample No.	D_o (mm)	H_o (mm)	D_{tc} (mm)	D_{bc} (mm)	D_b (mm)	H_f (mm)	Load (kN)	ρ_{final}	σ_z (MPa)	ε_z	σ_θ (MPa)	ε_θ	σ_m (MPa)	α	σ_{eff} (MPa)	β_σ	$\sigma_\theta/\sigma_{eff}$	σ_m/σ_{eff}
1	15.07	15.16	15.07	15.07	15.07	15.16	0	0.896	0	0	-	0	-	-	-	-	-	-
2	15.06	15.05	15.08	15.10	15.16	14.84	6.16	0.917	34.43	0.01	30.46	0.01	31.78	0.362	27.03	3.53	1.13	1.18
3	15.06	15.17	15.09	15.10	15.16	14.61	12.41	0.917	69.32	0.04	55.70	0.01	60.24	0.138	52.73	3.43	1.06	1.14
4	15.04	15.06	15.43	15.55	15.92	13.36	19.00	0.921	100.80	0.12	90.77	0.1	94.11	0.4	76.86	3.67	1.18	1.22
5	15.03	15.03	15.80	16.09	17.18	11.23	24.73	0.923	123.80	0.29	111.01	0.22	115.27	0.378	93.01	3.72	1.19	1.24
6	15.03	15.07	16.60	16.92	18.60	9.69	30.81	0.926	139.60	0.44	126.90	0.36	131.13	0.409	102.22	3.85	1.24	1.28
7	15.07	14.85	18.34	18.84	20.96	8.21	37.00	0.929	136.30	0.59	126.73	0.59	129.91	0.494	98.72	3.95	1.28	1.32

Appendix XII Hot compression test data of P/M Al–6wt.%B_4C preforms at 500 ^oC deformation temperature and 90% of IRD.

Sample No.	D_o (mm)	H_o (mm)	D_{tc} (mm)	D_{bc} (mm)	D_b (mm)	H_f (mm)	Load (kN)	ρ_{final}	σ_z (MPa)	ε_z	σ_0 (MPa)	ε_θ	σ_m (MPa)	α	σ_{eff} (MPa)	β_σ	$\sigma_\theta/\sigma_{eff}$	σ_m/σ_{eff}
1	15.08	15.21	15.08	15.08	15.08	15.21	0	0.903	0	0	-	0	-	-	-	-	-	-
2	15.05	15.11	15.18	15.24	15.3	14.67	6.33	0.919	34.82	0.03	32.049	0.03	32.97	0.491	27.322	3.62	1.17	1.21
3	15.04	15.1	15.18	15.22	15.31	14.3	12.66	0.923	69.74	0.05	60.70	0.03	63.71	0.283	51.501	3.71	1.18	1.24
4	15.04	15.04	15.45	15.5	16.00	13.22	18.00	0.927	95.66	0.13	86.76	0.10	89.72	0.395	69.317	3.88	1.25	1.29
5	15.09	15.17	15.87	16.21	17.67	11.29	21.00	0.932	103.90	0.30	95.60	0.26	98.36	0.432	72.766	4.06	1.31	1.35
6	15.07	15.06	17.00	17.61	19.20	9.49	27.30	0.933	116.00	0.46	107.49	0.42	110.34	0.455	80.47	4.11	1.34	1.37
7	15.08	15.07	18.56	18.97	21.31	8.12	33.00	0.937	119.30	0.62	111.95	0.61	114.39	0.496	79.833	4.30	1.40	1.43

Appendix XIII Hot compression test data of P/M Al–4wt.%B_4C preforms at deformation condition of Temperature = 300 ^oC, Strain rate = 0.1 s^{-1}, IRD = 80%.

Sample No.	D_o (mm)	H_o (mm)	D_{tc} (mm)	D_{bc} (mm)	D_b (mm)	H_f (mm)	Load (kN)	Average contact diameter	σ_Z (MPa)
1	15.08	15.36	15.05	15.05	15.05	15.14	0	15.05	0
2	15.07	15.39	15.92	16.1	17.29	11.5	28.2	16.01	140.02
3	15.07	15.19	16.01	16.27	17.6	11.21	29.6	16.14	144.61
4	15.08	15.26	16	16.34	17.7	10.99	30	16.17	146.02
5	15.08	15.33	16.18	16.28	18.03	10.87	31	16.23	149.78
6	15.08	15.28	16.31	16.44	17.96	10.79	33	16.375	156.63
7	15.06	15.31	16.71	16.86	19.24	9.62	34.99	16.785	158.06

Appendix XIV Hot compression test data of P/M Al–4wt.%B_4C preforms at deformation condition of Temperature = 400 ^oC, Strain rate = 0.1 s^{-1}, IRD = 80%.

Sample No.	D_o (mm)	H_o (mm)	D_{tc} (mm)	D_{bc} (mm)	D_b (mm)	H_f (mm)	Load (kN)	Average contact diameter	σ_Z (MPa)
1	15.06	15.13	15.06	15.06	15.06	15.13	0	15.06	0
2	15.06	15.48	16.09	16.34	17.77	11.01	26.7	16.215	129.24
3	15.09	15.29	16.16	16.26	17.9	10.86	27	16.21	130.77
4	15.08	15.38	16.51	16.64	18.47	10.23	29	16.575	134.34
5	15.07	15.31	16.63	16.79	18.87	9.79	30	16.71	136.74
6	15.06	15.29	16.78	17.2	19.14	9.5	32	16.99	141.09
7	15.09	15.37	17.01	17.8	19.68	9.13	34.64	17.405	145.53

Appendix XV Hot compression test data of P/M Al–4wt.%B_4C preforms at deformation condition of Temperature = 500 ^oC, Strain rate = 0.1 s^{-1}, IRD = 80%.

Sample No.	D_o (mm)	H_o (mm)	D_{tc} (mm)	D_{bc} (mm)	D_b (mm)	H_f (mm)	Load (kN)	Average contact diameter	σ_Z (MPa)
1	15.06	15.13	15.06	15.06	15.06	15.13	0	15.06	0
2	15.07	15.24	16.26	16.68	18.23	10.42	20	16.47	93.838
3	15.08	15.25	16.37	16.99	18.83	9.81	21	16.68	96.064
4	15.05	15.07	16.69	17.68	19.52	9.26	22	17.185	94.811
5	15.05	15.34	16.66	17.24	19.31	9.36	23	16.95	101.89
6	15.06	15.34	17.38	18.07	19.94	8.72	25.6	17.725	103.71
7	15.05	15.54	17.46	18.06	20.25	8.53	26.44	17.76	106.69

Appendix XVI Hot compression test data of P/M Al–4wt.%B_4C preforms at deformation conditions of Temperature = 300 ^oC, Strain rate = 0.2 s^{-1}, IRD = 80%.

Sample No.	D_o (mm)	H_o (mm)	D_{tc} (mm)	D_{bc} (mm)	D_b (mm)	H_f (mm)	Load (kN)	Average contact diameter	σ_Z (MPa)
1	15.04	15	15.04	15.04	15.04	15	0	15.04	0
2	15.07	15.29	15.57	15.58	16.78	12.36	25	15.575	131.17
3	15.07	15.3	15.8	15.6	16.8	12.3	26	15.7	134.25
4	15.05	15.3	15.6	15.72	16.81	12.27	29	15.66	150.5
5	15.07	15.35	15.71	15.74	17.28	11.66	31	15.725	159.56
6	15.08	15.38	16.01	16.16	17.71	11.08	33	16.085	162.33
7	15.07	15.43	16.64	16.71	18.96	9.94	35.22	16.675	161.21

Appendix XVII Hot compression test data of P/M Al–4wt.%B_4C preforms at deformation conditions of Temperature = 400 ^oC, Strain rate = 0.2 s^{-1}, IRD = 80%.

Sample No.	D_o (mm)	H_o (mm)	D_{tc} (mm)	D_{bc} (mm)	D_b (mm)	H_f (mm)	Load (kN)	Average contact diameter	σ_Z (MPa)
1	15.04	14.98	15.04	15.04	15.04	14.98	0	15.04	0
2	15.07	15.36	15.5	15.71	17.05	12.03	25	15.605	130.66
3	15.08	15.28	15.77	16.06	17.45	11.45	26.5	15.915	133.16
4	15.08	15.33	16.16	16.38	17.87	10.99	27.6	16.27	132.7
5	15.07	15.21	16.17	16.35	17.84	10.89	28	16.26	134.79
6	15.05	15.33	16.07	16.37	18.15	10.59	29.7	16.22	143.68
7	15.07	15.38	16.45	16.7	19.21	9.66	31.92	16.575	147.87

Appendix XVIII Hot compression test data of P/M Al–4wt.%B_4C preforms at deformation condition of Temperature = 500 ^oC, Strain rate = 0.2 s^{-1}, IRD = 80%.

Sample No.	D_o (mm)	H_o (mm)	D_{tc} (mm)	D_{bc} (mm)	D_b (mm)	H_f (mm)	Load (kN)	Average contact diameter	σ_Z (MPa)
1	15.04	15	15.04	15.04	15.04	15	0	15.04	0
2	15.07	15.34	15.82	16.26	17.62	11.44	20.5	16.04	101.41
3	15.09	15.43	15.92	16.51	18.05	10.74	21.5	16.215	104.07
4	15.07	15.25	16.34	16.95	18.7	9.93	22.5	16.645	103.36
5	15.09	15.32	16.25	17.01	18.9	9.83	23.5	16.63	108.15
6	15.08	15.39	16.36	17.23	19.03	9.73	24.5	16.795	110.55
7	15.09	15.35	16.67	17.91	19.62	9.11	25.52	17.29	108.65

Appendix XIX Hot compression test data of P/M Al–4wt.%B_4C preforms at deformation condition of Temperature = 300 ^oC, Strain rate = 0.3 s^{-1}, IRD = 80%.

Sample No.	D_o (mm)	H_o (mm)	D_{tc} (mm)	D_{bc} (mm)	D_b (mm)	H_f (mm)	Load (kN)	Average contact diameter	σ_Z (MPa)
1	15.07	15.24	15.07	15.07	15.07	15.24	0	15.07	0
2	15.07	15.39	15.4	15.61	16.52	12.83	26	15.505	137.65
3	15.08	15.29	15.43	15.72	16.79	12.33	27.12	15.575	142.29
4	15.05	15.36	15.61	15.81	16.98	12.16	29	15.71	149.55
5	15.05	15.19	15.74	15.91	17.22	11.63	31.1	15.825	158.06
6	15.05	15.3	15.87	15.96	17.46	11.42	33	15.915	165.82
7	15.05	15.31	16.38	16.48	18.49	10.24	34.81	16.43	164.12

Appendix XX Hot compression test data of P/M Al–4wt.%B_4C preforms at deformation condition of Temperature = 400 ^oC, Strain rate = 0.3 s^{-1}, IRD = 80%.

Sample No.	D_o (mm)	H_o (mm)	D_{tc} (mm)	D_{bc} (mm)	D_b (mm)	H_f (mm)	Load (kN)	Average contact diameter	σ_Z (MPa)
1	15.05	14.8	15.05	15.05	15.05	14.8	0	15.05	0
2	15.07	15.27	15.66	15.82	16.89	12.2	26	15.74	133.57
3	15.09	15.22	15.65	15.84	17.04	11.9	27	15.745	138.62
4	15.05	15.31	15.65	15.92	17.53	11.69	28	15.785	143.02
5	15.08	15.24	15.65	16.09	17.35	11.57	29.1	15.87	147.05
6	15.08	15.19	15.84	16.24	17.73	11.01	30.3	16.04	149.89
7	15.08	15.36	16.11	16.68	18.67	10.08	31.9	16.395	151.04

Appendix XXI Hot compression test data of P/M Al–4wt.%B_4C preforms at deformation condition of Temperature = 500 ^oC, Strain rate = 0.3 s^{-1}, IRD = 80%.

Sample No.	D_o (mm)	H_o (mm)	D_{tc} (mm)	D_{bc} (mm)	D_b (mm)	H_f (mm)	Load (kN)	Average contact diameter	σ_Z (MPa)
1	15.06	14.97	15.06	15.06	15.06	14.97	0	15.06	0
2	15.07	15.26	15.72	16.12	17.76	10.85	20	15.92	100.43
3	15.09	15.27	15.92	16.4	18.01	10.56	21	16.16	102.35
4	15.09	15.35	16	16.61	18.26	10.4	22	16.305	105.32
5	15.09	15.22	16.14	16.76	18.46	9.92	23	16.45	108.18
6	15.07	15.27	16.21	16.86	18.66	9.83	24	16.535	111.72
7	15.07	15.35	16.78	17.44	19.86	9.22	25.7	17.11	111.73

Appendix XXII Hot compression test data of P/M Al–4wt.%B_4C preforms at deformation condition of Temperature = 300 ^oC, Strain rate = 0.1 s^{-1}, IRD = 85%.

Sample No.	D_o (mm)	H_o (mm)	D_{tc} (mm)	D_{bc} (mm)	D_b (mm)	H_f (mm)	Load (kN)	Average contact diameter	σ_Z (MPa)
1	15.08	15.36	15.05	15.05	15.05	15.14	0	15.05	0
2	15.08	15.08	15.95	16.1	17.41	11.53	28.2	16.025	139.76
3	15.07	14.91	15.98	16.2	17.68	11.09	30.7	16.09	150.93
4	15.06	15.08	16.34	16.71	18.6	10.18	33.2	16.525	154.74
5	15.07	15.06	16.45	16.77	18.69	9.98	35.7	16.61	164.69
6	15.05	15.1	17.02	17.16	19.21	9.41	38.2	17.09	166.46
7	15.05	15.1	17.57	17.52	20.01	8.79	40.63	17.545	167.99

Appendix XXIII Hot compression test data of P/M Al–4wt.%B_4C preforms at deformation condition of Temperature = 400 ^oC, Strain rate = 0.1 s^{-1}, IRD = 85%.

Sample No.	D_o (mm)	H_o (mm)	D_{tc} (mm)	D_{bc} (mm)	D_b (mm)	H_f (mm)	Load (kN)	Average contact diameter	σ_Z (MPa)
1	15.06	15.13	15.06	15.06	15.06	15.13	0	15.06	0
2	15.06	15.13	16.26	16.39	18.01	10.82	28.5	16.325	136.1
3	15.07	15.01	16.38	16.96	18.78	10	30.5	16.67	139.69
4	15.07	15.05	16.6	17	18.93	9.78	31.5	16.8	142.05
5	15.06	15.07	17.3	17.31	19.38	9.28	33.5	17.305	142.38
6	15.06	15	17.59	18.02	20.45	8.47	35.6	17.805	142.92
7	15.07	15.02	17.67	17.97	20.28	8.44	36.63	17.82	146.81

Appendix XXIV Hot compression test data of P/M Al–4wt.%B_4C preforms at deformation condition of Temperature = 500 ^oC, Strain rate = 0.1 s^{-1}, IRD = 85%.

Sample No.	D_o (mm)	H_o (mm)	D_{tc} (mm)	D_{bc} (mm)	D_b (mm)	H_f (mm)	Load (kN)	Average contact diameter	σ_Z (MPa)
1	15.06	15.13	15.06	15.06	15.06	15.13	0	15.06	0
2	15.08	15	16.08	16.3	17.61	11.28	22.5	16.19	109.25
3	15.08	14.91	16.11	16.39	17.68	11.07	24.3	16.25	117.12
4	15.05	15.15	16.32	16.4	18.22	10.46	25	16.36	118.88
5	15.06	15.06	16.66	16.82	18.51	10.11	26.2	16.74	118.99
6	15.09	15.05	17.04	17.89	19.79	9.04	28.2	17.465	117.66
7	15.08	15.06	18.08	18.43	20.7	8.23	30.2	18.255	115.34

Appendix XXV Hot compression test data of P/M Al–4wt.%B_4C preforms at deformation condition of Temperature = 300 ^oC, Strain rate = 0.2 s^{-1}, IRD = 85%.

Sample No.	D_o (mm)	H_o (mm)	D_{tc} (mm)	D_{bc} (mm)	D_b (mm)	H_f (mm)	Load (kN)	Average contact diameter	σ_Z (MPa)
1	15.04	15	15.04	15.04	15.04	15	0	15.04	0
2	15.06	15.04	15.9	16.03	17.14	11.84	30.2	15.965	150.8
3	15.06	15	16.11	16.28	17.6	11.19	32.3	16.195	156.74
4	15.09	14.98	16.34	17.04	18.11	10.52	34.7	16.69	158.54
5	15.05	14.97	16.58	16.71	18.16	10.5	36	16.645	165.38
6	15.08	15.04	16.71	16.88	18.75	9.93	38	16.795	171.46
7	15.09	15.01	17.07	17.34	19.22	9.4	39.95	17.205	171.77

Appendix XXVI Hot compression test data of P/M Al–4wt.%B_4C preforms at deformation condition of Temperature = 400 ^oC, Strain rate = 0.2 s^{-1}, IRD = 85%.

Sample No.	D_o (mm)	H_o (mm)	D_{tc} (mm)	D_{bc} (mm)	D_b (mm)	H_f (mm)	Load (kN)	Average contact diameter	σ_Z (MPa)
1	15.04	14.98	15.04	15.04	15.04	14.98	0	15.04	0
2	15.07	14.96	15.75	16.07	17.36	11.46	27.2	15.91	136.76
3	15.08	15.16	15.99	16.24	17.74	11.11	28.6	16.115	140.17
4	15.05	15.13	16.33	16.73	18.59	10.16	30.2	16.53	140.67
5	15.09	15.13	16.4	16.63	18.55	10.06	32.2	16.515	150.26
6	15.09	14.87	17.24	17.75	19.78	8.93	34.3	17.495	142.63
7	15.07	15.11	17.64	18.09	20.17	8.72	37.6	17.865	149.94

Appendix XXVII Hot compression test data of P/M Al–4wt.%B_4C preforms at deformation condition of Temperature = 500 ^oC, Strain rate = 0.2 s^{-1}, IRD = 85%.

Sample No.	D_o (mm)	H_o (mm)	D_{tc} (mm)	D_{bc} (mm)	D_b (mm)	H_f (mm)	Load (kN)	Average contact diameter	σ_Z (MPa)
1	15.04	15	15.04	15.04	15.04	15	0	15.04	0
2	15.08	15	15.44	15.54	16.87	12.24	21	15.49	111.39
3	15.05	15.14	15.85	16.27	17.55	11.42	22.3	16.06	110.04
4	15.08	15.05	16.01	16.39	17.88	10.95	24.5	16.2	118.82
5	15.08	15.11	16.08	16.47	18.17	10.6	26	16.275	124.93
6	15.07	15	16.71	17.32	19.34	9.38	27.5	17.015	120.89
7	15.05	15.14	17.36	18.1	20.22	8.62	29.1	17.73	117.82

Appendix XXVIII Hot compression test data of P/M Al–4wt.%B_4C preforms at deformation condition of Temperature = 300 ^oC, Strain rate = 0.3 s^{-1}, IRD = 85%.

Sample No.	D_o (mm)	H_o (mm)	D_{tc} (mm)	D_{bc} (mm)	D_b (mm)	H_f (mm)	Load (kN)	Average contact diameter	σ_Z (MPa)
1	15.07	15.24	15.07	15.07	15.07	15.24	0	15.07	0
2	15.07	14.88	15.93	15.96	17.16	11.64	28	15.945	140.17
3	15.09	15	15.88	16.15	17.43	11.38	29	16.015	143.91
4	15.08	15.08	16.27	16.64	18.06	10.71	31	16.455	145.71
5	15.09	15.08	16.6	16.6	18.22	10.48	35	16.6	161.65
6	15.09	15.02	16.74	17.03	18.74	9.97	37.2	16.885	166.06
7	15.07	15.1	16.91	16.92	19.18	9.58	39.23	16.915	174.51

Appendix XXIX Hot compression test data of P/M Al–4wt.%B_4C preforms at deformation condition of Temperature = 400 ^oC, Strain rate = 0.3 s^{-1}, IRD = 85%.

Sample No.	D_o (mm)	H_o (mm)	D_{tc} (mm)	D_{bc} (mm)	D_b (mm)	H_f (mm)	Load (kN)	Average contact diameter	σ_Z (MPa)
1	15.05	14.8	15.05	15.05	15.05	14.8	0	15.05	0
2	15.05	14.94	16.01	16.14	17.48	11.37	28.4	16.075	139.88
3	15.05	15.02	16.24	16.44	17.86	10.91	29.4	16.34	140.15
4	15.07	15.06	16.42	16.84	18.34	10.34	31	16.63	142.66
5	15.07	15.13	16.45	16.87	18.6	10.11	33	16.66	151.32
6	15.06	15.02	16.87	17.31	19.19	9.48	35	17.09	152.52
7	15.08	15.09	17.42	17.92	19.94	8.77	37.33	17.67	152.17

Appendix XXX Hot compression test data of P/M Al–4wt.%B_4C preforms at deformation condition of Temperature = 500 ^oC, Strain rate = 0.3 s^{-1}, IRD = 85%.

Sample No.	D_o (mm)	H_o (mm)	D_{tc} (mm)	D_{bc} (mm)	D_b (mm)	H_f (mm)	Load (kN)	Average contact diameter	σ_Z (MPa)
1	15.06	14.97	15.06	15.06	15.06	14.97	0	15.06	0
2	15.08	14.95	15.55	15.93	17.07	11.84	22	15.74	113.02
3	15.08	15	15.85	16.21	17.45	11.44	23	16.03	113.92
4	15.06	15.06	16.41	17.06	18.38	10.78	24.7	16.735	112.25
5	15.08	15.09	16.35	16.63	18.13	10.68	25.5	16.49	119.35
6	15.07	15.08	16.71	17.18	18.81	9.9	27	16.945	119.68
7	15.09	15.1	17	17.83	19.73	9.08	28.59	17.415	119.98

Appendix XXXI Hot compression test data of P/M Al–4wt.%B_4C preforms at deformation condition of Temperature = 300 ^oC, Strain rate = 0.1 s^{-1}, IRD = 90%.

Sample No.	D_o (mm)	H_o (mm)	D_{tc} (mm)	D_{bc} (mm)	D_b (mm)	H_f (mm)	Load (kN)	Average contact diameter	σ_Z (MPa)
1	15.08	15.36	15.05	15.05	15.11	15.14	15.08	15.05	0
2	15.05	15.19	16.29	16.31	17.97	11.19	15.05	16.3	150.89
3	15.07	15.3	16.82	16.84	18.39	10.9	15.07	16.83	161.76
4	15.09	15.17	17.22	17.38	19.19	9.62	15.09	17.3	165.85
5	15.08	15.17	17.68	17.5	19.52	9.42	15.08	17.59	168.65
6	15.06	15.13	18.42	18.63	20.37	8.55	15.06	18.525	172.45
7	15.07	14.8	19.05	19.9	21.21	7.99	15.07	19.475	171.14

Appendix XXXII Hot compression test data of P/M Al–4wt.%B_4C preforms at deformation condition of Temperature = 400 ^oC, Strain rate = 0.1 s^{-1}, IRD = 90%.

Sample No.	D_o (mm)	H_o (mm)	D_{tc} (mm)	D_{bc} (mm)	D_b (mm)	H_f (mm)	Load (kN)	Average contact diameter	σ_Z (MPa)
1	15.06	15.13	15.06	15.06	15.06	15.13	0	15.06	0
2	15.08	15.17	15.74	15.67	16.51	11.4	26.2	15.705	135.2
3	15.05	14.73	15.9	15.73	16.97	10.91	28.1	15.815	142.99
4	15.06	15.13	16.54	16.48	18.05	10.91	30.1	16.51	140.54
5	15.09	15.19	16.89	17.46	19.2	9.78	34.3	17.175	147.99
6	15.08	15.16	17.61	18.06	19.99	9.05	38	17.835	152.05
7	15.07	15.14	18.65	18.84	21.19	8.15	41.37	18.745	149.85

Appendix XXXIII Hot compression test data of P/M Al–4wt.%B_4C preforms at deformation condition of Temperature = 500 ^oC, Strain rate = 0.1 s^{-1}, IRD = 90%.

Sample No.	D_o (mm)	H_o (mm)	D_{tc} (mm)	D_{bc} (mm)	D_b (mm)	H_f (mm)	Load (kN)	Average contact diameter	σ_Z (MPa)
1	15.06	15.13	15.06	15.06	15.06	15.13	0	15.06	0
2	15.05	15.29	16.41	16.74	18.36	10.7	26	16.575	120.45
3	15.07	15.35	16.33	16.88	18.53	10.57	27.1	16.605	125.09
4	15.09	15.17	16.64	17.1	18.81	10.19	28.5	16.87	127.45
5	15.08	14.94	16.88	17.36	19.25	9.47	30.1	17.12	130.71
6	15.06	15.11	17.63	17.62	20.23	8.81	33.1	17.625	135.61
7	15.07	15.21	19.22	19.09	21.44	8.01	36	19.155	124.87

Appendix XXXIV Hot compression test data of P/M Al–4wt.%B_4C preforms at deformation condition of Temperature = 300 ^oC, Strain rate = 0.2 s^{-1}, IRD = 90%.

Sample No.	D_o (mm)	H_o (mm)	D_{tc} (mm)	D_{bc} (mm)	D_b (mm)	H_f (mm)	Load (kN)	Average contact diameter	σ_Z (MPa)
1	15.04	15	15.04	15.04	15.04	15	0	15.04	0
2	15.05	15.3	15.9	15.96	17	12.43	28.6	15.13	159.01
3	15.08	15.18	15.88	16.27	17.48	11.74	31	16.075	152.68
4	15.06	15.23	16.48	16.35	18.15	10.98	34.2	16.415	161.54
5	15.09	15.28	17	17.06	18.82	10.16	38	17.03	166.76
6	15.08	15.14	17.33	17.53	19.5	9.42	42.1	17.43	176.37
7	15.07	15.22	18.16	18.37	20.55	8.52	45.81	18.265	174.77

Appendix XXXV Hot compression test data of P/M Al–4wt.%B_4C preforms at deformation condition of Temperature = 400 ^oC, Strain rate = 0.2 s^{-1}, IRD = 90%.

Sample No.	D_o (mm)	H_o (mm)	D_{tc} (mm)	D_{bc} (mm)	D_b (mm)	H_f (mm)	Load (kN)	Average contact diameter	σ_Z (MPa)
1	15.04	14.98	15.04	15.04	15.04	14.98	0	15.04	0
2	15.05	15.27	16	16.28	17.51	11.72	28.3	16.14	138.27
3	15.07	15.28	16.2	16.4	17.94	11.24	30.1	16.3	144.19
4	15.09	15.22	16.59	16.72	18.63	10.42	32.6	16.655	149.58
5	15.08	15.31	16.81	17.2	19.21	9.84	35	17.005	154.05
6	15.06	15.11	17.31	17.65	19.64	9.26	37.6	17.48	156.62
7	15.07	14.8	18.17	18.38	20.44	8.42	40.1	18.275	152.81

Appendix XXXVI Hot compression test data of P/M Al–4wt.%B_4C preforms at deformation condition of Temperature = 500 ^oC, Strain rate = 0.2 s^{-1} IRD = 90%.

Sample No.	D_o (mm)	H_o (mm)	D_{tc} (mm)	D_{bc} (mm)	D_b (mm)	H_f (mm)	Load (kN)	Average contact diameter	σ_Z (MPa)
1	15.04	15	15.04	15.04	15.04	15	0	15.04	0
2	15.08	15.24	16.58	16.98	18.45	10.65	26.5	16.78	119.78
3	15.05	15.14	17.46	17.48	18.45	10.08	27.1	17.47	113.01
4	15.06	15.24	16.84	17.23	18.96	10.04	28	17.035	122.8
5	15.09	15.22	17.35	18.12	20.02	9.09	30.1	17.735	121.8
6	15.08	15.31	17.6	18.08	20.11	8.99	32.2	17.84	128.77
7	15.07	15.26	18.14	18.72	20.92	8.33	34	18.43	127.4

Appendix XXXVII Hot compression test data of P/M Al–4wt.%B_4C preforms at deformation condition of Temperature = 300 ^oC, Strain rate = 0.3 s^{-1}, IRD = 90%.

Sample No.	D_o (mm)	H_o (mm)	D_{tc} (mm)	D_{bc} (mm)	D_b (mm)	H_f (mm)	Load (kN)	Average contact diameter	σ_Z (MPa)
1	15.07	15.24	15.07	15.07	15.07	15.24	0	15.07	0
2	15.05	15.28	15.77	15.81	17.25	12.05	30.1	15.79	153.65
3	15.07	15.24	15.92	15.94	17.56	11.62	32.7	15.93	164
4	15.09	15.16	16.33	16.38	18.25	10.82	35.7	16.355	169.86
5	15.08	15.27	16.74	16.98	18.88	10.15	38.6	16.86	172.83
6	15.06	15.14	17.07	17.18	19.37	9.6	41.7	17.125	180.97
7	15.07	15.19	17.66	17.75	19.82	9.18	43.5	17.705	176.62

Appendix XXXVIII Hot compression test data of P/M Al–4wt.%B_4C preforms at deformation condition of Temperature = 400 ^oC, Strain rate = 0.3 s^{-1}, IRD = 90%.

Sample No.	D_o (mm)	H_o (mm)	D_{tc} (mm)	D_{bc} (mm)	D_b (mm)	H_f (mm)	Load (kN)	Average contact diameter	σ_Z (MPa)
1	15.05	14.8	15.05	15.05	15.05	14.8	0	15.05	0
2	15.08	15.23	16.06	16.35	17.8	11.4	28.3	16.205	137.16
3	15.05	15.31	16.21	16.36	18.05	11.08	30.1	16.285	144.45
4	15.06	15.12	16.71	17.03	18.96	10.03	33.1	16.87	148.02
5	15.09	15.3	17.16	17.47	19.54	9.41	36	17.315	152.82
6	15.08	15.25	17.73	18.15	20.64	8.6	39.5	17.94	156.2
7	15.07	15.1	18.43	18.82	21.01	8.17	42.1	18.625	154.46

Appendix XXXIX Hot compression test data of P/M Al–4wt.%B_4C preforms at deformation condition of Temperature = 500 ^oC, Strain rate = 0.3 s^{-1}, IRD = 90%.

Sample No.	D_o (mm)	H_o (mm)	D_{tc} (mm)	D_{bc} (mm)	D_b (mm)	H_f (mm)	Load (kN)	Average contact diameter	σ_Z (MPa)
1	15.06	14.97	15.06	15.06	15.06	14.97	0	15.06	0
2	15.05	15.3	15.78	16.27	17.62	11.69	25	16.025	123.9
3	15.07	15.3	16.37	17.01	18.82	10.27	27.3	16.69	124.73
4	15.09	15.21	16.88	17.46	19.32	9.68	29.1	17.17	125.63
5	15.08	15.1	17.65	17.88	19.88	8.98	31.6	17.765	127.44
6	15.06	14.6	17.4	18.07	20.17	8.6	32.7	17.735	132.32
7	15.07	15.3	18.1	18.89	21	8.34	34.55	18.495	128.55

Appendix XL Material property relations of Al-4wt.%B_4C preforms with initial relative density of 80%

Temp (K)	έ (s^{-1})	σ (MPa)	ln σ (MPa)	ln (έ) (s^{-1})	1/T*1000 (K)	lnsinh(ασ) (MPa)
573	0.1	158.02	5.063	-2.303	1.745	0.506
573	0.2	161.21	5.083	-1.609	1.745	0.536
573	0.3	164.10	5.100	-1.204	1.745	0.563
673	0.1	145.54	4.980	-2.303	1.486	0.386
673	0.2	147.87	4.996	-1.609	1.486	0.409
673	0.3	151.05	5.018	-1.204	1.486	0.440
773	0.1	106.78	4.671	-2.303	1.293	-0.023
773	0.2	108.65	4.688	-1.609	1.293	-0.002
773	0.3	111.71	4.716	-1.204	1.293	0.033

Model Calculations of Appendix XL – XLV

Calculation of β values:-

Graph between **σ vs ln(έ).** The value of β can be obtain from the slope of the lines **ln(έ) - σ** plot

$$\beta = \left[\frac{\partial ln\, \acute{\varepsilon}}{\partial \sigma}\right]_{T=const}$$

Table: The values of σ and ln(έ) from Appendix XL

Temp.	300 °C		400 °C		500 °C	
Strain rate (s^{-1})	σ (MPa)	ln(έ) (s^{-1})	σ (MPa)	ln(έ) (s^{-1})	σ (MPa)	ln(έ) (s^{-1})
0.1	158.02	-2.302	145.54	-2.302	106.78	-2.302
0.2	161.21	-1.609	147.87	-1.609	108.65	-1.609
0.3	164.1	-1.203	151.05	-1.203	111.71	-1.203

Table: The value of β from lines **ln(ἐ) - σ (Fig σ vs ln(ἐ)).**

Temp.	β
300 °C	0.181
400 °C	0.195
500 °C	0.214
Avg.	**0.196**

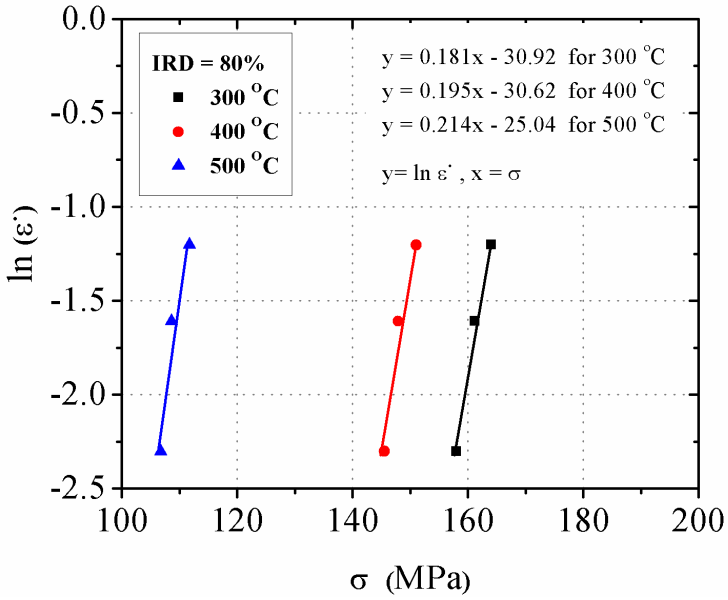

Fig. Relationship between lnἐ– lnσ of Al–4wt.%B_4C composite with IRD: 80%.

<u>Calculation of *n* values:-</u>

Graph between **lnσ vs ln(ἐ)** The value of n can be obtain from the slope of the lines ln(ἐ) - lnσ plot

$$n = \left[\frac{\partial ln\, \dot{\varepsilon}}{\partial ln\sigma}\right]_{T=const}$$

Table: The values of lnσ and ln(ε̇) from Appendix XL

Temp.	300 °C		400 °C		500 °C	
Strain rate (s^{-1})	lnσ (MPa)	ln(ε̇) (s^{-1})	lnσ (MPa)	ln(ε̇) (s^{-1})	lnσ (MPa)	ln(ε̇) (s^{-1})
0.1	5.062	-2.302	4.98	-2.302	4.67	-2.302
0.2	5.078	-1.609	4.99	-1.609	4.68	-1.609
0.3	5.10	-1.203	5.02	-1.203	4.71	-1.203

Table: The value of β from lines ln(ε̇) -ln σ (Fig lnσ vs ln(ε̇)).

Temp.	*n*
300 °C	24.45
400 °C	24.25
500 °C	23.95
Avg.	**24.23**

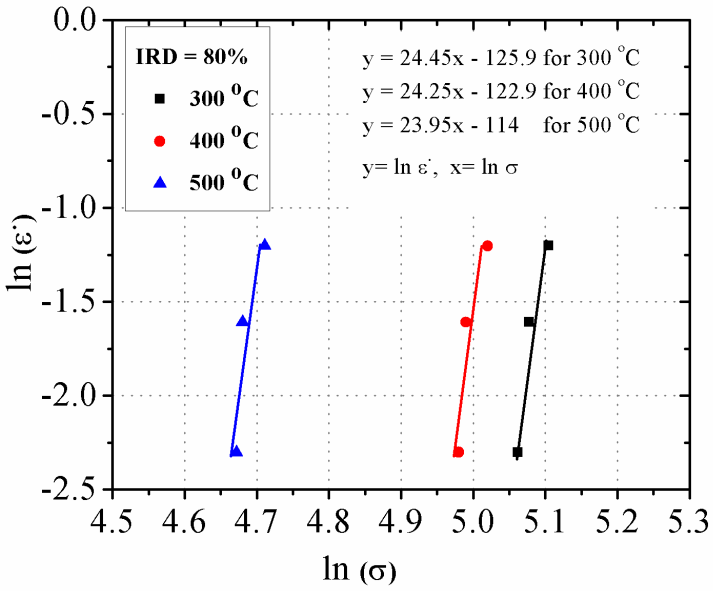

Fig. Relationship between lnε̇–σ of Al–4wt.%B_4C composite with IRD: 80%.

Calculation of α value:-

Temp.	β	n	α=β/n
300	0.181	24.45	0.007403
400	0.195	24.25	0.008041
500	0.214	23.95	0.008917
Avg.	**0.1967**	**24.233**	**0.00812**

Calculation of Activation energy (Q):-

$$Q = R\left[\frac{\partial ln\acute{\varepsilon}}{\partial ln[sinh(\alpha\sigma)]}\right]_{T=const}\left[\frac{\partial ln[sinh(\alpha\sigma)]}{\partial\left(\frac{1}{T}\right)}\right]_{\acute{\varepsilon}=const}$$

Q=Rṅm

$$\dot{n} = \left[\frac{\partial ln\acute{\varepsilon}}{\partial ln[sinh(\alpha\sigma)]}\right]_{T=const}$$

$$m = \left[\frac{\partial ln[sinh(\alpha\sigma)]}{\partial\left(\frac{1}{T}\right)}\right]_{\acute{\varepsilon}=const}$$

Calculation of *ṅ* values:-

The value of ***ṅ*** can be obtain from the slope of the lines lnsinh (ασ) - ln(έ) plot

Table: The values of lnsinh (ασ) and ln(έ) from Appendix XL

Temp.	300 °C		400 °C		500 °C	
Strain rate (s^{-1})	lnsinh (ασ)	ln(έ) (s^{-1})	lnsinh (ασ)	ln(έ) (s^{-1})	lnsinh (ασ)	ln(έ) (s^{-1})
0.1	0.506	-2.302	0.38	-2.302	-0.02	-2.302
0.2	0.536	-1.609	0.4153	-1.609	-0	-1.609
0.3	0.567	-1.203	0.4418	-1.203	0.039	-1.203

Table: The value of $\dot{n}$ from lines lnέ–ln[sinh(ασ)] (Fig lnέ vs ln[sinh(ασ)]).

Tem.	$\dot{n}$
300 °C	17.98
400 °C	17.88
500 °C	16.2
Avg.	**17.35**

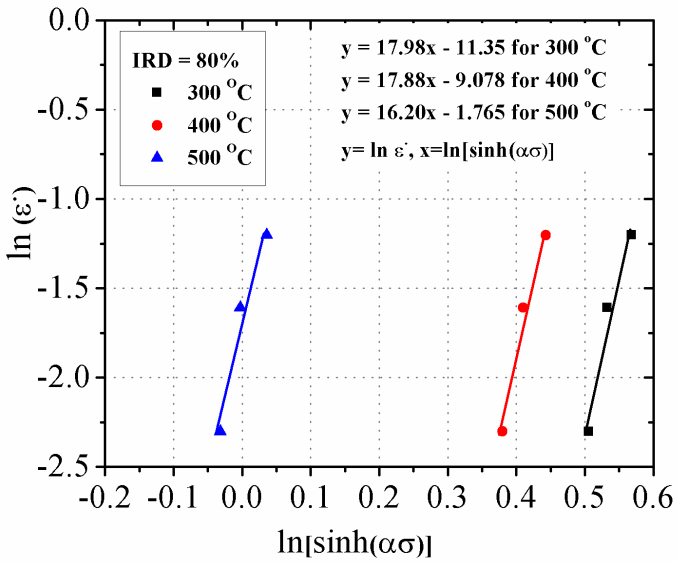

Fig. Relationship between lnέ–ln[sinh(ασ)] of Al–4wt.%B_4C composite with IRD: 80%.

Calculation of *m* values:-

The value of **m** can be obtain from the slope of the lines 1/T*1000 -lnsinh (ασ) plot

Table: The values of 1/T and lnsinh (ασ) from Appendix XL

Strain rate (s^{-1})	300 °C		400 °C		500 °C	
Temp.	1/T*1000	lnsinh (ασ)	1/T*1000	lnsinh (ασ)	1/T*1000	lnsinh (ασ)
300 °C	1.744	0.5	1.744	0.52	1.744	0.56
400 °C	1.485	0.39	1.485	0.42	1.485	0.44
500 °C	1.293	-0.025	1.293	-0.0029	1.293	0.041

Table: The value of *m* from lines **ln[sinh (ασ)]–1/T (Fig ln[sinh (ασ)] vs 1/T).**

Strain rate (s^{-1})	**m**
0.1	1.122
0.2	1.115
0.3	1.112
AVG	1.116

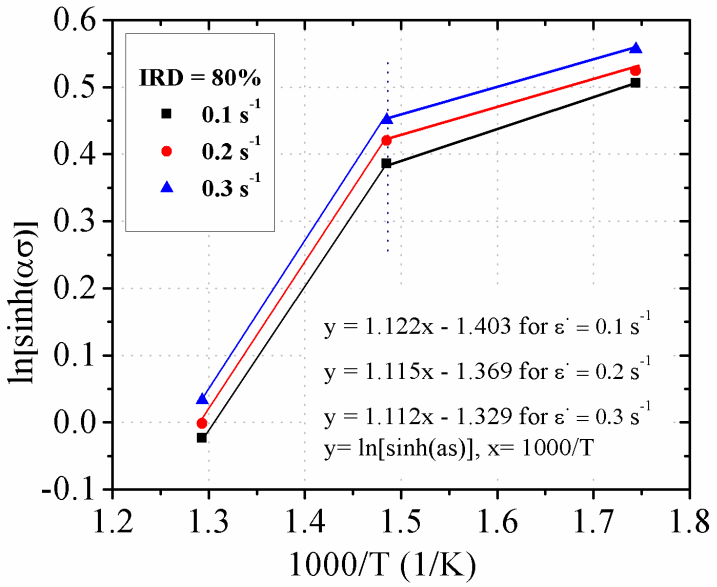

Fig. Relationship between ln[sinh (ασ)]–1/T of Al–4wt%B_4C composite with IRD: 80%.

Calculation of Activation Energy and Zener Hollomon parameter:-

Activation Energy (Q)

At T=300 ^oC, strain rate (ε̇) = 0.1 s^{-1}

Q = Rṅm

Universal gas constant (R) = 8.31 J/mk, ṅ = 24.45, m = 1.122

Q=8.314 X 24.45 X 1.122

Q= 167.723 **KJ/m**

Zener Hollomon parameter:-

$$Z = \dot{\varepsilon}\, exp\left(\frac{Q}{RT}\right)$$

Z= 0.1 X exp (167.723 X 1000/8.314 X 573.15)

Z= 1.93E+14 s^{-1}

Calculation of lnA values:-

The value of **lnA** can be obtain from the slope of the lines **-lnsinh (ασ) – lnZ** plot

Table: The values of **ln(Z) – ln[sinh(ασ)]** from Appendix XLI**.**

lnsinh(ασ)	ln(Z)
0.506	32.9
0.536	33.37
0.563	33.68
0.386	27.5
0.409	28.01
0.439	28.33
-0.023	21.21
-0.001	21.75
0.032	22.1

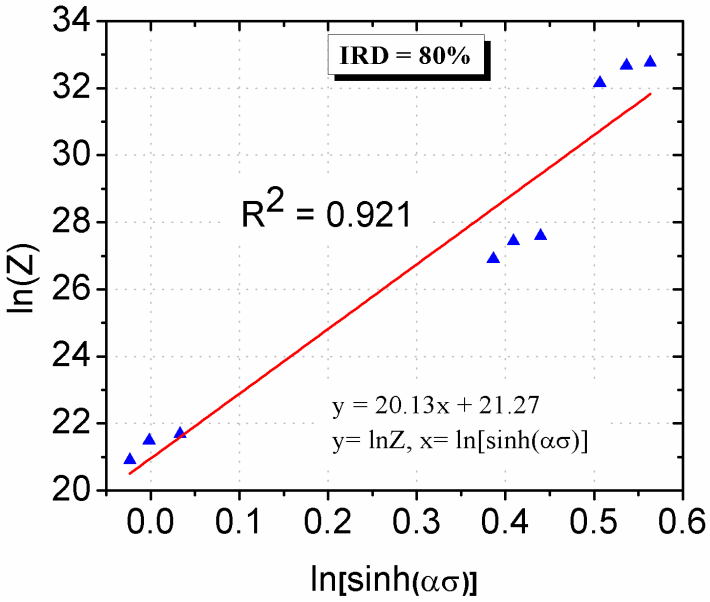

Fig. Relationship between lnZ–ln[sinh(ασ)] of Al–4wt.%B_4C composite with IRD:80%.

Similarly, activation energy, Zener Hollomon parameter and lnA were calculated for various deformation temperatures, strain rates and relative densities as shown in Appendix XLI-XLV.

Appendix XLI Material constants obtained for various processing conditions for P/M Al-4wt.%B_4C preforms with initial relative density of 80%.

IRD (%)	Temp (K)	έ (s^{-1})	σ (MPa)	β	n	α	n'	m	Q (kJ/mol)	Z (s^{-1})	ln(Z)	lnsinh(ασ) (MPa)	lnA
80	573	0.1	158.02	0.181	24.45	0.0074	17.98	1.122	167.723	1.93E+14	32.9	0.506	21.27
	573	0.2	161.21					1.115	166.677	3.1E+14	33.37	0.536	
	573	0.3	164.10					1.112	166.228	4.24E+14	33.68	0.563	
	673	0.1	145.54	0.195	24.25	0.008	17.88	1.122	166.790	8.77E+11	27.50	0.386	
	673	0.2	147.87					1.115	165.750	1.46E+12	28.01	0.409	
	673	0.3	151.05					1.112	165.304	2.02E+12	28.33	0.440	
	773	0.1	106.78	0.214	23.95	0.0089	16.2	1.122	151.119	1.62E+09	21.21	-0.023	
	773	0.2	108.65					1.115	150.176	2.8E+09	21.75	-0.002	
	773	0.3	111.71					1.112	149.772	3.95E+09	22.10	0.033	
Average				0.197	24.21	0.0081	17.35	1.116	161.06				

Appendix XLII Material property relations of Al-4wt.%B_4C preforms with initial relative density of 85%

Temp (K)	έ (s^{-1})	σ (MPa)	ln σ (MPa)	ln (έ) (s^{-1})	1/T*1000 (K)	lnsinh(ασ) (MPa)
573	0.1	167.97	5.124	-2.303	1.745	0.463
573	0.2	171.78	5.147	-1.609	1.745	0.498
573	0.3	173.49	5.157	-1.204	1.745	0.513
673	0.1	146.81	4.989	-2.303	1.486	0.272
673	0.2	149.93	5.01	-1.609	1.486	0.301
673	0.3	152.18	5.027	-1.204	1.486	0.325
773	0.1	115.3	4.748	-2.303	1.293	-0.04
773	0.2	117.81	4.769	-1.609	1.293	-0.014
773	0.3	119.97	4.787	-1.204	1.293	0.009

Appendix XLIII Material constants obtained for various processing conditions for P/M Al-4wt.%B_4C preforms with initial relative density of 85%.

IRD (%)	Temp (K)	έ (s^{-1})	σ (MPa)	β	n	α	n'	m	Q (kJ/mol)	Z (s^{-1})	ln(Z)	lnsinh(ασ) (MPa)	lnA
85	573	0.1	167.97	0.196	28.91	0.0068	19.64	1.091	178.146	1.72E+15	35.08	0.463	24.16
	573	0.2	171.78					1.089	177.819	3.22E+15	35.71	0.498	
	573	0.3	173.49					1.085	177.166	4.21E+15	35.98	0.513	
	673	0.1	146.81	0.205	28.31	0.0072	18.88	1.091	171.252	1.95E+12	28.3	0.272	
	673	0.2	149.93					1.089	170.939	3.68E+12	28.93	0.301	
	673	0.3	152.18					1.085	170.311	4.93E+12	29.23	0.325	
	773	0.1	115.30	0.236	28.12	0.0083	18.60	1.091	168.713	2.5E+10	23.94	-0.04	
	773	0.2	117.81					1.089	168.403	4.77E+10	24.59	-0.014	
	773	0.3	119.97					1.085	167.785	6.5E+10	24.9	0.009	
Average				0.212	28.44	0.0074	19.04	1.088	172.282				

Appendix XLIV Material property relations of Al-4wt.%B_4C preforms with initial relative density of 90%.

Temp (K)	$\dot{\varepsilon}$ (s^{-1})	σ (MPa)	ln σ (MPa)	ln ($\dot{\varepsilon}$) (s^{-1})	1/T*1000 (K)	lnsinh(ασ) (MPa)
573	0.1	171.13	5.142	-2.303	1.745	0.409
573	0.2	173.16	5.160	-1.609	1.745	0.439
573	0.3	175.24	5.170	-1.204	1.745	0.454
673	0.1	150.26	5.010	-2.303	1.486	0.224
673	0.2	151.61	5.029	-1.609	1.486	0.256
673	0.3	153.76	5.040	-1.204	1.486	0.269
773	0.1	124.87	4.828	-2.303	1.293	-0.009
773	0.2	127.10	4.847	-1.609	1.293	0.015
773	0.3	127.81	4.859	-1.204	1.293	0.038

Appendix XLV Material constants obtained for various processing conditions for P/M Al-4wt.%B_4C preforms with initial relative density of 90%.

IRD (%)	Temp (K)	έ (s^{-1})	σ (MPa)	β	n	α	n'	m	Q (kJ/mol)	Z (s^{-1})	ln(Z)	lnsinh(ασ) (MPa)	lnA
90	573	0.1	171.13	0.226	35.07	0.0064	24.23	0.913	183.922	5.79E+15	36.29	0.409	25.5
	573	0.2	173.16					0.905	182.311	8.25E+15	36.65	0.439	
	573	0.3	175.24					0.897	180.699	8.83E+15	36.72	0.454	
	673	0.1	150.26	0.237	34.71	0.0068	24.05	0.913	182.556	1.47E+13	30.32	0.224	
	673	0.2	151.61					0.905	180.956	2.2E+13	30.72	0.256	
	673	0.3	153.76					0.897	179.357	2.48E+13	30.84	0.269	
	773	0.1	124.87	0.267	34.50	0.0077	23.91	0.913	181.493	1.83E+11	25.93	-0.009	
	773	0.2	127.10					0.905	179.903	2.86E+11	26.38	0.015	
	773	0.3	127.81					0.897	178.313	3.35E+11	26.54	0.038	
Average				0.243	34.76	0.0069	24.06	0.905	181.057				